



UPMC
SORBONNE UNIVERSITÉS



UNIVERSITÉ PIERRE ET MARIE CURIE - PARIS VI

École Doctorale 388: Chimie Physique et Chimie Analytique de Paris-Centre

Ab-initio study of X-Ray spectroscopy of molecular ions

thesis presented by

Alessandra PUGLISI

Stéphane CARNIATO	University Pierre et Marie Curie	Supervisor
Pascal CHABERT	Université Pierre et Marie Curie	
Sonia CORIANI	Technical University of Denmark	Rapporteur
Carine CLAVAGUERA	Paris Sud University	
Sylvain CRISTOL	University of Lille	Rapporteur
Jean-Paul MOSNIER	Dublin City University	
Nicolas SISOURAT	University Pierre et Marie Curie	Co-supervisor

*To my family
mum, dad, Elena and Aurora*

Contents

Acknowledgements	3
Résumé	5
Introduction	13
Theoretical background	21
1 Core shell spectroscopy	25
1.1 Spectroscopic techniques	25
1.2 The X-ray photoabsorption process	26
1.3 The Resonant Auger effect	28
2 From the Schrödinger equation to the photoabsorption cross section	31
2.1 The Schrödinger Equation	31
2.2 Time-Independent Schrödinger Equation and Born - Oppenheimer approximation	33
2.3 Potential energy surface approximation	34
2.4 Cross section	36
2.4.1 Cross section in the time-independent approach	36
2.4.2 Cross section in linear coupling model approximation	39
2.4.3 Cross section in the time-dependent approach	41
2.4.4 Equivalence between the time dependent and independent approach	44
3 Electronic structure calculations	47

3.1	The wavefunction approximation and Slater determinant	47
3.2	The Hartree-Fock method	48
	The Hartree-Fock equation	48
	Solving the Hartree-Fock equation	49
3.2.1	Application of the Hartree Fock method	53
	3.2.1.1 The Restricted Hartree-Fock method	53
	3.2.1.2 The Unrestricted Hartree Fock method	55
	3.2.1.3 The Restricted Open-shell Hartree Fock method	57
3.3	The post Hartree-Fock methods	58
	3.3.1 Configuration Interaction method	58
	Configuration Interaction for the excited state calculations	60
	3.3.2 Multi Configurational self-consistent field method	61
3.4	Density Functional Theory	62
4	Computational protocols	65
4.1	K-shell protocol	65
	4.1.1 Development of the protocol	66
	Geometry optimization and ionization potential	66
	Optimization of the guess and active space choice	68
	Potential energy surfaces and dipole moment transitions	69
	Nuclear dynamics	69
	Comparison with the experimental data	69
4.2	L-shell molecular ions	70
	4.2.1 Photoabsorption spectra	70
	Geometry optimization and ionization potential	71
	Potential energy surfaces, spin orbit coupling and dipole moment transitions	71
	Nuclear dynamics	73
	Comparison with the experimental data	74
	4.2.2 L-edge ionization potential	74
4.3	Computational details	76

Results and discussion	81
5 X-ray absorption spectra of CH_n^+ and OH_n^+ molecular ions	83
5.1 CH^+ as case study to the calibration of the method	84
5.1.1 Geometry optimization and ionization potential	84
5.1.2 Optimization of the spin-orbitals and the active space choice	84
5.1.3 Nuclear dynamics results	87
5.1.4 Comparison with experimental data	92
5.2 Calculations of the photoabsorption spectra of CH_n^+	94
5.3 Calculation of the photoabsorption spectra of OH_n^+	97
6 X-ray absorption spectra of SiH_n^+ molecular ions	103
6.1 SiH^+	103
6.1.1 Spin Orbit Coupling operator	104
6.1.2 Electronic transitions analysis	107
6.1.3 Nuclear dynamic simulation	108
6.1.4 Comparison with experimental data	111
6.2 SiH_2^+	115
6.3 SiH_3^+	121
6.4 Infrared spectroscopy for the study of silicon molecular ions	126
7 Spin-orbit coupling correction to the 2p ionization potential of Silicon molecular ions	129
7.1 SiH^+	129
7.2 SiH_3^+	134
8 Conclusions and perspectives	137
Appendix	139
Appendix A	141
Appendix B	145

List of Figures

I.1	Fragmentation pathways of silane, SiH ₄ , molecule in microwave plasma	15
I.2	Scheme of Multi-Analysis Ion Apparatus (MAIA) set-up	16
1.1	The electromagnetic spectrum.	26
1.2	Representation of the X-ray photoionization (A) and photoexcitation (B) processes.	27
1.3	Fluorescence and Auger yield for atoms with $Z < 120$ (from ref. [45]).	29
1.4	Schema of the photoabsorption process followed by the possible de-excitation ways.	30
2.1	General example of PESs with and without a minimum	35
2.2	Vibrational levels ν of potential energy surfaces of ground and excited states in the harmonic oscillator approximation and correspondent FC factors	38
2.3	Evolution of the nuclear wavepacket	43
3.1	Scheme of the Self Consistent Field (SCF) procedure used to solve the Hartree-Fock equation.	56
4.1	Scheme of the calibration of the K-shell protocol	67
4.2	Scheme of the calibration of the L-shell protocol	72
4.3	General scheme of the degeneracy removing in the 2p orbitals	74
4.4	Scheme of the calculation of photoelectron spectra	77
5.1	Simulated photoabsorption spectra of CH ⁺ at CIS level with the three different set of spin-orbitals.	86
5.2	Simulated photoabsorption spectra on logarithmic scale of CH ⁺ at CIS level with the three different references.	86
5.3	CH ⁺ molecular orbitals involved in the electronic transition.	87

5.4	Pontential enegy curve of CH^+	89
5.5	Computed Lorentzian spectra within the methods ND-I.A, ND-I.B and ND-II.	90
5.6	Comparison of simulated X-ray photoabsorption spectra of CH^+ with and without nuclear dynamic.	91
5.7	Comparison between theoretical and experimental results of CH^+ molecular ion.	93
5.8	CH_2^+ and OH_2^+ experimental spectra.	94
5.9	CH_2^+ molecular orbitals involved in the electronic transition.	95
5.10	CH_2^+ computed X-ray photoabsorption spectrum.	96
5.11	CH_3^+ computed X-ray photoabsorption spectrum.	97
5.12	OH^+ computed spectrum, comparison between the vertical and nuclear wavepacket results.	98
5.13	Comparison between the theoretical and experimental spectrum of OH^+	99
5.14	OH_2^+ molecular orbitals involved in the electronic transition.	100
5.15	OH_2^+ computed X-ray photoabsorption spectrum.	101
5.16	OH_3^+ molecular orbitals involved in the electronic transition.	101
5.17	OH_3^+ X-ray photoabsorption spectrum.	102
6.2	SiH^+ simultaед spectra with different spin-orbit coupling methods.	106
6.3	CPU-time for the spin-orbit coupling calculations	107
6.4	Molecular orbitals involved in the electronic transitions of SiH^+	108
6.5	Spectra computed with vertical approximation, linear coupling model and nuclear wavepacket propagation approaches for ground state SiH^+ molecular ion.	110
6.6	Spectra computed with vertical approximation, linear coupling mode and nuclear wavepacket propagation approaches for metastable state SiH^+ molecular ion.	111
6.7	Experimetal and theoretical spectra photoabsorption cross section for SiH^+ molecular ion	113
6.8	Photoabsorption cross section spectra computed with the nuclear wavepacket propagation and linear coupling method for SiH^+	114
6.9	Ground state - metastable state energy gap for SiH_n^+ ($n= 1, 2, 3$) molecular ions.	115
6.10	Geometry of $^2\text{SiH}_2^+$ and $^4\text{SiH}_2^+$	116
6.11	Molecular orbitals involved in the electronic transitions of SiH_2^+ ground state	117
6.12	Molecular orbitals involved in the electronic transitions of SiH_2^+ metastable state	117

6.13	Comparison between the spectra computed within the vertical and linear coupling model for ${}^2\text{SiH}_2^+$	119
6.14	Comparison between the spectra computed within the vertical and linear coupling model for ${}^4\text{SiH}_2^+$	119
6.15	Experimental and theoretical spectra photoabsorption cross section for SiH_2^+ molecular ion	120
6.16	Geometry of ${}^1\text{SiH}_3^+$ and ${}^3\text{SiH}_3^+$	121
6.17	Molecular orbitals involved in the electronic transitions of SiH_3^+ ground state . .	122
6.18	Molecular orbitals involved in the electronic transitions of SiH_3^+ metastable state	122
6.19	Comparison between the spectra computed within the vertical and linear coupling model for ${}^1\text{SiH}_3^+$	124
6.20	Comparison between the spectra computed within the vertical and linear coupling model for ${}^3\text{SiH}_3^+$	124
6.21	Experimental and theoretical photoabsorption cross section for SiH_3^+ molecular ion	125
6.22	Simulated Infrared spectra of SiH^+ in the ground (red line) and metastable (blue line) state.	127
6.23	Simulated Infrared spectra of SiH_3^+ in the ground (red line) and metastable (blue line) state.	128
6.24	Simulated Infrared spectra of SiH_3^+ in the ground and metastable state.	128
7.1	SiH^+ binding energy spectra computed with the CIS-3/0/0 (left) and CISD-3/2/150 (right) methods	131
7.2	HCl photoelectron spectra computed with the CIS-3/0/0 (left) and CISD-3/2/150 (right) methods	133
7.3	SiH_3^+ photoelectron spectra computed with the CIS-3/0/0 (left) and CISD-3/2/150 (right) methods	136
B.1	Vertical X-ray photoabsorption spectra of ${}^1\text{SiH}^+$ (top) and ${}^3\text{SiH}^+$ (bottom) . . .	147
B.2	${}^2\text{SiH}_2^+$ normal modes.	149
B.3	${}^4\text{SiH}_2^+$ normal modes.	149
B.4	Vertical X-ray photoabsorption spectra of ${}^2\text{SiH}_2^+$ (top) and ${}^4\text{SiH}_2^+$ (bottom) . . .	150
B.5	${}^1\text{SiH}_3^+$ normal modes.	152
B.6	${}^3\text{SiH}_3^+$ normal modes	152
B.7	Vertical X-ray photoabsorption spectra of ${}^1\text{SiH}_3^+$ (top) and ${}^3\text{SiH}_3^+$ (bottom) . . .	153

List of abbreviations

BOA Born-Oppenheimer approximation

CI Configuration Interaction

CIS Configuration Interaction Singles

CISD Configuration Interaction Singles Doubles

CISDT Configuration Interaction Singles Doubles Triples

CSF Configuration State Functions

DFT Density Functional Theory

ECRIS Electron Cyclotron Resonance Ion Source

FC Franck-Condon

FWHM Full Width at Half Maximum

GVB Generalized Valence Bond

HA Harmonic Approximation

HF Hartree - Fock

IP Ionization Potential

IR Infrared spectroscopy

ISM Interstellar Medium

LCAO Linear Combination of Atomic Orbitals

MAIA Multi-Analysis Ion Apparatus

-
- MCSCF** Multi Configurational Self Consistent Field
- MO** Molecular Orbital
- ORMAS** Occupation Restricted Multiple Active Space
- PECVD** Plasma Enhanced Chemical Vapour Deposition
- ROHF** Restricted Open shell Hartree-Fock
- SCF** Self Consistent Field
- SOC** Spin Orbit Coupling
- TDSE** Time-Dependent Schrödinger Equation
- TISE** Time-Independent Schrödinger Equation
- UHF** Unrestricted Hartree-Fock
- XAS** X-Ray Absorption Spectroscopy

List of symbols

m_e	Mass of the electron
\mathbf{p}	Momentum operator
$\dot{\mathbf{r}}$	Velocity operator
\mathbf{r}	Position operator
Γ	Decay width
τ	Core-hole lifetime
Ψ	Wavefunction
H	Hamiltonian operator
T	Kinetic energy operator
V	Potential energy operator
ψ	Wavefunction coordinates dependent
ϑ	Wavefunction time dependent
φ	Full adiabatic wavefunction
ϕ	Nuclear wavefunction
x	Cartesian coordinates
Q	Normal coordinates
μ	Reduced mass
ω	Vibrational frequency
μ_{ab}	Transition dipole moment between the state a and b
ω_{ab}	Angular frequency of the photon
ν	Vibrational level of the electronic ground state
ν'	Vibrational level of the electronic excited state

χ	Spin-orbitals
α, β	Spin functions
γ	Full width half maximum Lorentzian profile
ξ	Full width half maximum Gaussian profile
Ω	Spin-orbit coupling constant

*“Above all, don’t fear difficult moments.
The best comes from them.”*
— Rita Levi Montalcini

Acknowledgements

First, I want to thank Prof. S. Coriani and Prof. S. Cristol for accepting to be referees of my Ph.D. work and Prof. P. Chabert, Dr. C. Clavaguera and Pr. J.-P. Mosnier for accepting to be examiners on my Ph.D. defence.

I want to thank my advisor Prof. Stéphane Carniato for having welcomed me in his group three years ago, for having introduced me to the wonderful world of the core-hole spectroscopies and for always being available to reply to my questions or discuss my results. I am also grateful to Dr. Nicolas Sisourat, for being a kind person with a great patience. Thank you for all the time spent teaching, discussing and helping me to solve my problems and for being always available each time I entered your office saying “Nico, I have a problem...”. I wish to thank you both for your kindness and for being great scientists and persons. I am really proud to have been a part of your research group.

I am much obliged to Patricia, Natalie and Vita.

A big thank you, full of hearts and all the sweetest things I can think of, goes to my amazing colleagues Selma, Solene “*SoSo*” and Tsveta “*SuSu*” also known as the “*trois petits cochons*” (three little pigs). Thank you for being friends not only colleagues and also for the numerous lunches, coffee breaks, dinners, happy hours at “La Montagne”, for all discussions about science, food and fool things. If I loved the time spent in the office, it is also because of you.

I express my gratitude to the (old) LCPMR third floor Alfred, Angela, David M., Jèrèmie and Richard, who have kindly welcomed me. Especially, I want to thank Richard, “*le prof bizarre du troisième étage*” (the weird professor of the third floor) for spending every day one minute to say “Hey! Buongiorno, come va?” (“Hey! Good morning, how are you?”, in Italian) and for all the discussions about science, life and cooking.

Thank you Aicha, Basile, Bastien, François, Junwen, Sèvan and the aforementioned Selma,

Solene and Tsveta for sharing the office with me in during my Ph.D. and Antoine, Anthony, Quentin, Marie with whom I shared very nice moments.

I would like to thank the whole LCMPR group!

I thank to all my friend I met here in Paris especially Enzo (now in Como - Italy), Daria (now in Valencia - Spain) and Domenico (now in Bari - Italy), Salvatore "Sasi" (still in Paris!), Marco (now in Padua), Andrea and Tiziano. I thank Debora (now in Barcellona - Spain) for all the talks in front of a good ultraviolet, for the time spent together in Paris, and for being still present despite the distance. A special thought goes to Cecilia just because our friendship is too difficult to summarize in a sentence, but you know what I mean! I am grateful to Alessio, who has been a sort of a second family since I moed in Paris, I could not imagine that nothing would have changed in these 10 years (just the countries).

Thank you Davide, to be by my side, for your love, presence and support through these years. I love you.

And finally I would to thank *my family*: mum and dad, Elena and Aurora, just for being my family. If I am the person who I am, it is only thanks to you, without your support I would have never arrived here. You believed in me more than I believed in my self. You gave me the strength to go through all the blue moments I had, every time you told me "you are strong, you can do it! We believe in you". You and your love make me strong! Thank you!

Résumé

L'objectif de la thèse est la simulation des spectres de photo-absorption au seuil L (2p) des ions moléculaires de silicium SiH_n^+ ($n= 1, 2, 3$) et au seuil K (1s) des ions moléculaire de l'oxygène OH_n^+ ($n= 1, 2$) et du carbone CH_n^+ ($n=1, 2$). Ce travail s'inscrit dans le cadre du labex plas@par de Sorbonne Universités. L'intérêt porté sur ces petites molécules ioniques est double, à la fois dans le domaine de l'astrophysique et de la microélectronique.

En effet, généralement le domaine de longueur d'onde des radiations interstellaire se trouve au-dessous de 13.6 eV ce qui, conjointement à la large abondance d'atomes d'hydrogène, implique qu'une grande quantité d'éléments se trouvent sous forme d'ions moléculaires, en particulier d'ions chargés protonés. Leur présence dans le milieu interstellaire (ISM) joue ainsi un rôle très important dans la description de l'évolution des nuages interstellaires. La présence des ions moléculaires de carbone dans l'ISM est connu depuis longtemps, la première identification datant de 1937 . En revanche, l'observation des espèces à base d'oxygène et de silicium est plus récente. L'intérêt des deux premières classes d'ions est lié à leur capacité à former des hydrates de carbone, c'est à dire de petits acides organiques ainsi que des molécules d'eau, respectivement.

En outre, les ions moléculaires de silicium jouent un rôle crucial aussi dans la composition des plasma de laboratoire et conditionne leur application dans la "plasma-enhanced chemical vapour depositions" (PECVD) utilisées pour le dépôt de couches minces de silicium à partir de silane (SiH_4). Le dépôt de couches minces de silicium utilisant les réacteurs de type PECVD à partir de silane est en effet une clé technologique dans la fabrication des semi-conducteurs, utiles pour la micro-électronique, et la conception de films minces pour l'industrie des cellules photovoltaïques, à base de silicium. Une connaissance précise et détaillée de la croissance de ces films minces et en particulier le rôle joué par les espèces SiH_x ($x =1-3$) et (SiH^+ , SiH_2^+ , SiH_3^+) est reconnu comme un préalable à l'optimisation de la croissance de films minces

Une des voies de caractérisation est l'utilisation de techniques spectroscopiques dans le domaine des rayons X. En effet, parmi l'ensemble des spectroscopies existantes, les dispositifs expérimentaux utilisant le rayonnement électromagnétique dans le domaine des transitions X (de quelques centaines à plusieurs milliers d'électron-Volts) présentent un certain nombre d'avantages. Tout d'abord, la longueur d'onde des radiations X est comparable aux distances interatomiques, ce qui la rend particulièrement bien adaptée pour caractériser la structure d'un matériau, via les méthodes de diffraction des rayons X. Un autre avantage, et non des moindres, est la sélectivité des spectroscopies X vis à vis des éléments chimiques. L'examen d'un échantillon par son spectre X d'absorption ou d'émission nous renseigne sur sa composition chimique puisqu'il met en évidence les éléments chimiques qui le composent. Citons quelques techniques de caractérisation aux différents acronymes (XPS, NEXAFS, EXAFS, RIXS, etc.). L'XPS ou ESCA (Electron Spectroscopy for Chemical Analysis) permet notamment l'analyse de la structure électronique d'un matériau à partir de la mesure de l'énergie d'ionisation des couches internes. La caractérisation de l'énergie de liaison des électrons de coeur est fondamentale puisque sa valeur dépend, entre autres effets, de l'environnement chimique de l'atome émetteur, signature de ce que l'on appelle communément le déplacement chimique. Elles sont également sollicitées pour l'étude de la dynamique de systèmes moléculaires ou la caractérisation de matériaux solides complexes (supra-conducteurs, composants du manteau terrestre, adsorption moléculaire sur semi-conducteurs, etc.). La spectroscopie X a réalisé dans ce domaine d'énormes progrès grâce aux avancées technologiques apportées par les nouvelles générations de sources de radiation X. Il est aujourd'hui facile de disposer de lumière hautement monochromatique, polarisée, de très haute intensité, avec une résolution spectrale pouvant aller jusqu'à moins de quelques milli-électron volt (meV). Le rayonnement synchrotron produit par les anneaux de stockage permet d'accéder à cette excellence. Grâce à ce bond technologique, il est possible de mettre en évidence la structure vibrationnelle associée. C'est donc un domaine de compétences qui accompagne les progrès technologiques réalisés dans le développement de sources de lumière à haute résolution et qui trouve un écho dans la communauté scientifique autour des nouveaux centres synchrotron.

Mon travail théorique a été réalisé en collaboration étroite avec un groupe expérimental installé au synchrotron SOLEIL (J-M Bizau, D. Cubaynes) et une équipe de l'Université de Dublin (E. Kennedy, J. P. Mosnier, P. Van Kampen) travaillant sur la production de ces espèces au sein d'un plasma chaud de molécules de silane, de méthane ou d'eau dans une source ECR (electron cyclotron resonance). L'apport majeur des expériences réalisées par les équipes de SOLEIL et Dublin est de pouvoir combiner ici la production d'ions hydrures chargés et pouvoir

sonder dans le même temps la structure électronique de ces espèces au seuil K, L avec une haute résolution grâce à l'utilisation du rayonnement synchrotron de 3eme génération (ligne Pléiade de SOLEIL). Toutefois, l'interprétation des spectres des niveaux de coeur de ces espèces est délicate pour plusieurs raisons. En effet, (i) les spectres obtenus présentent un grand nombre de structures correspondant à des transitions électroniques vers des états de valence (localisés) ou de Rydberg (états diffus) enrichis des effets de couplage spin-orbite (seuil L), (ii) la température (élevée) au sein du plasma autorise la population d'états excités de valence dont la multiplicité de spin peut être différente de l'état électronique fondamental, (iii) enfin, suite à l'excitation par le rayonnement X, ces différents systèmes évoluent suivant plusieurs voies de recombinaison électronique (ex: fluorescence, X, effet Auger). De plus, de large déformations géométriques (jusqu'à la dissociation moléculaire) sont mis en jeu. L'interprétation des mesures nécessite donc l'appui de simulations numériques réalisées à un niveau DFT et post Hartree Fock.

Les modèles théoriques mis en place ont permis de calculer avec une relative bonne précision les surfaces d'énergie potentielle des états électroniques engagés dans une gamme d'énergie couvrant plusieurs dizaines d'eV. En outre, la dynamique des noyaux et des électrons ont des constantes de temps caractéristiques différentes en raison de leurs masses très différentes. Le mouvement des électrons est à l'échelle de quelques centaines d'attosecondes, tandis que le temps de vibration des noyaux est supérieur à la femtoseconde. Pour cette raison, on est amené à considérer que les électrons répondent presque instantanément aux déplacements des noyaux, ce qui permet de séparer les degrés de liberté électroniques et nucléaires. C'est l'approximation de Born-Oppenheimer. La probabilité de transition est alors déterminée dans l'approximation de Franck-Condon par le recouvrement des fonctions d'onde vibrationnelles entre l'état fondamental et l'état excité. La fenêtre de probabilité (dite "zone de Franck-Condon") est essentiellement conditionnée par la largeur de la fonction de probabilité vibrationnelle des noyaux dans l'état fondamental. C'est l'essence même du principe de Franck-Condon qui stipule que les positions des noyaux (lents) restent inchangées lors de la transition électronique (rapide). Autrement dit, les noyaux étant considérés comme immobiles lors de l'excitation électronique, la molécule se retrouve dans un ou plusieurs états vibrationnels de l'état électronique après l'excitation. Le nombre de ces états vibrationnels dépend de la largeur de la fenêtre de Franck-Condon, et du profil de la surface de potentiel de l'état excité. L'excitation électronique se répartie donc sur plusieurs nombres quantiques : c'est la progression vibrationnelle.

Le but principal de cette thèse a été de développer des protocoles numériques permettant de calculer avec une précision raisonnable les spectres d'absorption au seuil K et L en combinant des méthodes de structures électroniques et de propagation de paquet d'ondes.

La thèse présente deux parties principales: une description des techniques et modèles théoriques utilisés est tout d'abord détaillée. Ensuite une partie dédiée à la discussion des résultats est présentée. Dans la première partie sont exposés les principaux concepts des spectroscopies utilisant le rayonnement X ainsi qu'une présentation de la notion de section efficace, discutée dans une approche dépendante et indépendante du temps. Dans cette première partie, les différentes approches de calcul utilisées pour la description des systèmes excités en couche interne sont décrites. En particulier, une présentation des méthodes de chimie quantique utilisées au cours de ce travail est donnée. Un des problèmes majeurs rencontré au cours de ce travail a été de traiter des états excités de nature très différentes.

Dans le cas de l'oxygène ou du carbone, l'excitation de coeur a lieu en couche 1s ce qui nécessite la prise en compte essentiellement de la relaxation électronique. Pour le silicium, élément plus lourd, l'excitation étudiée a lieu en couche 2p. Dans ce cas, l'interaction spin-orbite joue un rôle déterminant en contribuant notamment à une complexité accrue (multiplication des bandes) du spectre d'excitation. Pour mener à bien ce travail, les calculs ont été réalisés en utilisant des codes disposant de méthodes ab-initio à un niveau post Hartree-Fock ou/et DFT. L'utilisation de ce type d'approches est justifiée par le grand nombre de raies d'absorption sur une large gamme spectrale (20-30 eV). Nous avons fait le choix en particulier d'utiliser la méthode d'Interaction de Configurations réduite aux simples excitations (CIS) pour le calcul des surfaces d'énergie potentielle et des moments de transition permettant d'accéder aux intensités absolues des raies observées avec une relative bonne précision. Nous avons établi que la prise en compte des effets de relaxation suite à la création d'un trou localisé en couche interne est essentiel. Le calcul de surface d'énergie potentielle a été réalisé en utilisant les spin-orbitales optimisées pour un système excité en couche interne, afin d'inclure la relaxation électronique dans nos simulations. Différentes façon de prendre en compte la relaxation électronique ont été étudiées et sont présentées en détail.

Les surfaces d'énergies potentielles ainsi que les moments de transitions dipolaires ont été utilisés pour calculer les sections efficaces absolues d'absorption, à l'aide d'une méthode de propagation de paquet d'ondes nucléaires. Compte tenu de la production probable d'ions moléculaires dans une configuration excitée de valence au sein des sources plasma, ces calculs ont été réalisés à la fois pour l'état fondamental et le premiers état excité métastable de valence de chaque espèce. Afin de déterminer semi-quantitativement la proportion des ions moléculaires métastables dans la source de plasma utilisée par nos collègues expérimentateurs, nous avons cherché à optimiser les populations relatives de l'état fondamental et de l'état métastable par une méthode de moindres carrés afin de reproduire les résultats expérimentaux.

La seconde partie de cette thèse présente une analyse détaillée des résultats théoriques obtenus, ainsi qu'une comparaison de ces résultats avec les expériences menées sur synchrotron. Le protocole de calcul des sections efficaces a été testé sur les systèmes mono-protonnés, CH^+ et OH^+ . Ces tests sont présentés en détail. Les spectres ainsi obtenus sont comparés avec les mesures expérimentales. Les résultats des simulations montrent un très bon accord avec les mesures, comme le montre la Figure 1. De plus, à partir de nos simulations nous avons estimé que pour CH^+ le rapport entre la population dans l'état fondamental et excité de valence est de 9 pour 1 alors que pour OH^+ seul l'état fondamentale est peuplé dans la source ECR utilisée.

Une fois le protocole de calculs bien établi, nous l'avons appliqué pour le calcul des spectres de CH_2^+ et OH_2^+ . Cependant, les données expérimentales sont pas disponibles actuellement.

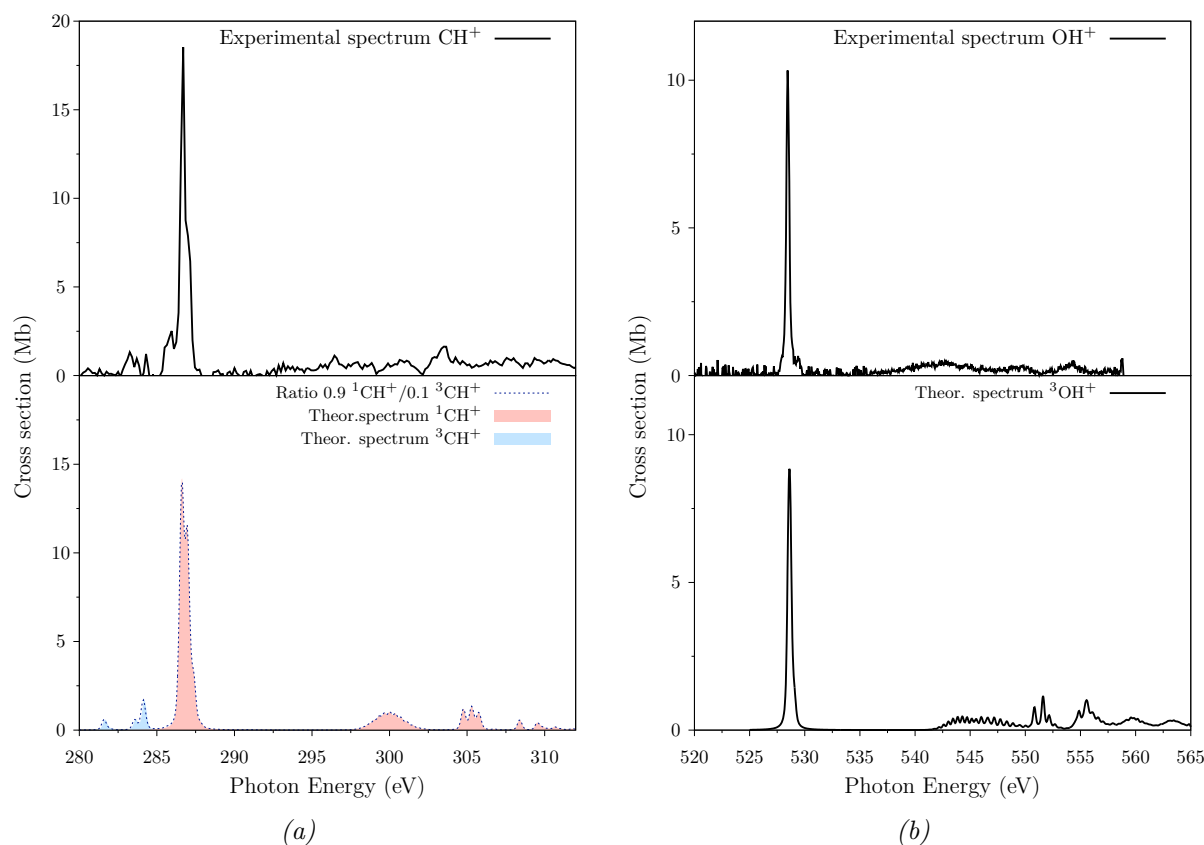


Figure 1: Comparaison entre les résultats des simulations et les données expérimentales. En bas: spectres théoriques des ions moléculaires CH^+ (a) et OH^+ (b). En haut: spectres expérimentaux des ions moléculaires CH^+ , OH^+ .

Dans la suite du manuscrit, l'étude des systèmes à base de silicium excités en couche

L est présentée. Pour cette étude, nous avons pris en compte explicitement l'interaction spin-orbite en utilisant l'opérateur de Breit-Pauli, ce qui alourdit notablement les calculs. Afin de pouvoir traiter les systèmes multiprotonés (SiH_2^+ et SiH_3^+), nous avons étudié l'effet des différents termes de l'opérateur de Breit-Pauli sur le spectre de SiH^+ . Nous avons montré que les termes monoélectroniques de cet opérateur sont les plus importants. En effet, les sections efficaces d'absorption de SiH^+ changent peu lorsque l'on néglige les termes bi-électroniques, ce qui rend les calculs beaucoup plus rapide, et faisable pour SiH_2^+ et SiH_3^+ . Comme pour les molécules de carbone et d'oxygène, nous avons calculé les spectres pour les états excités métastables.

Les temps de calculs étant élevés pour les systèmes à base de silicium, la simulation des spectres d'absorption avec la méthode de propagation du paquet d'onde n'était pas possible. Afin toutefois de prendre en compte la dynamique nucléaire, nous avons utilisé la méthode du couplage linéaire (Linear Coupling Model) qui est beaucoup moins coûteuse.

Dans la dernière partie des résultats, les spectres sont comparés aux données expérimentales. Nous avons aussi évalués les populations de l'état fondamental et de l'état métastable de chaque espèce dans la source ECR, en utilisant la méthode de moindres carrés. Les résultats pour les ions de silicium sont présentés sur la Figure 2. La procédure de "fit" suggère que pour SiH^+ , SiH_2^+ et SiH_3^+ les populations relatives de l'état fondamental sont 50%, 85% et 20%, respectivement.

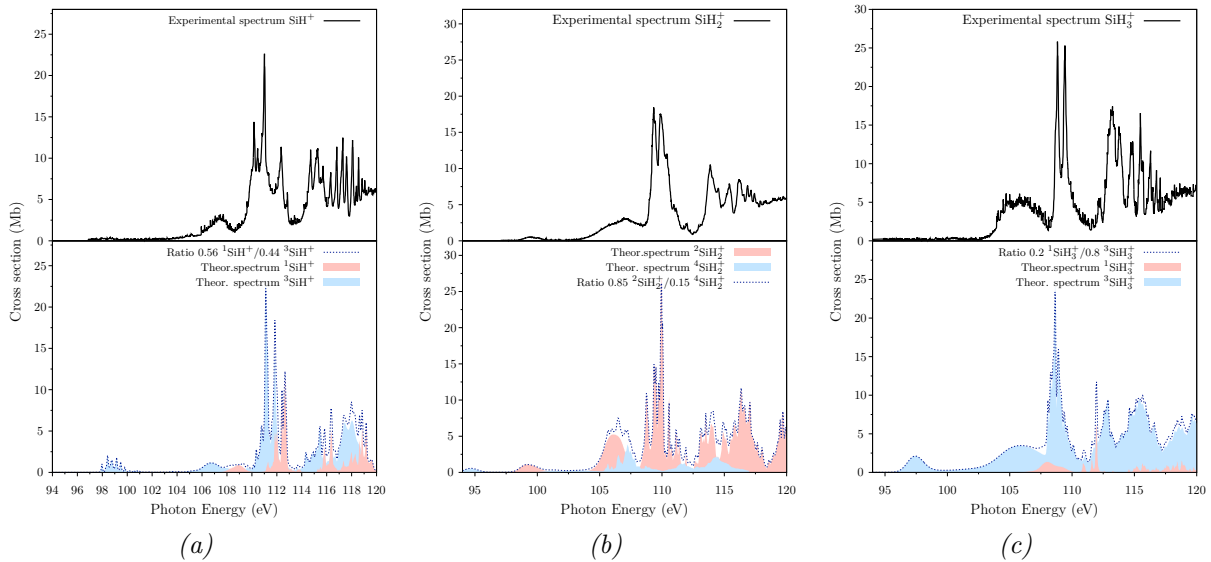


Figure 2: Comparaison entre les résultats des simulations et les données expérimentales. En bas: spectres théoriques des ions moléculaires SiH^+ (a), SiH_2^+ (b) et SiH_3^+ (c). En haut: spectres expérimentaux des ions moléculaires SiH^+ , SiH_2^+ et SiH_3^+ .

En conclusion, au cours de cette thèse nous avons développé un protocole basé sur des méthodes de structure électronique combinées avec des approches de propagation de paquet d'onde afin de simuler, interpréter et prédire les spectres d'absorption du rayonnement X d'ions moléculaires. Nous avons proposé deux protocoles différents pour l'absorption au seuil K d'ions contenant des éléments de la deuxième ligne du tableau périodique et au seuil L pour des éléments de la troisième ligne. L'étude de ces systèmes pour lesquelles les données expérimentales sont disponibles montre un très bon accord expérience/théorie.

Introduction

The Interstellar Medium (ISM) is constituted of gas in various stages of ionization and it contains both atomic and molecular species, as well as dust particles [1]. The regions of the ISM are classified according to the temperature and the density of the matter. The phases are classified as

- *cold phase* characterized by low temperature ($< 100K$) and high density ($10^2 - 10^6 \text{ cm}^{-3}$). In this region the species present are molecules or neutral gas.
- *warm phase* which has temperature of $10^{3-4}K$ and density lower than the first one ($1 - 10^4 \text{ cm}^{-3}$). Both neutral and ionized gas are found in this phase.
- *hot phase* having temperature higher than 10^6K and very low density (10^{-3} cm^{-3}). It is characterized by ionized gas.

The study of the atomic and molecular systems in the ISM provides information on the physics and chemistry of astrophysical objects (stars, molecular clouds, galaxies, etc...). Chemically speaking, the size of the species in the ISM is between 2 and 13 atoms. An half of the detected molecules includes water, ammonia, formaldehyde and small alcohols (methanol, ethanol) while the remaining are positive molecular ions (e.g. H_3^+ , HCO^+ , H_3O^+), radicals (C_nH), isomers (e.g. HNC , HCCNC , HOC^+) and unusual triatomic rings (e.g. C_3H , C_3H_2). Molecule and molecular ions containing elements of the second row as silicon and chlorine are also observed [2].

The hydrogen, H, represents the most abundant element since it constitutes 70% of the whole chemical composition. The remaining percentage is constituted by Helium (28%) and other “heavier” elements (2%) [3]. The first two are formed in a process called *primordial nucleosynthesis* while the heavier elements originates from the evolution of the stars [1]. Due to the H abundance, the protonated species coming from reactions of H with heavier elements

(C, N, O, S, ...) are the first products formed in the ISM. They can be in the form of the neutral molecules (i.e. CH, NH, OH, OH₂) and molecular ions (i.e. CH⁺, OH⁺, H₂O⁺, ...). The investigation of molecular ions has therefore an important role in the study of the stellar evolution [4, 2].

The identification of CH⁺ in the interstellar medium is dated to 1937 and was one of the first molecular ion detected [5, 6, 7]. Molecular ions containing oxygen have been detected in the last decade [8] both in the monoprotonated [8, 9] and multiprotonated forms [10], OH⁺ and OH_n⁺ (n=2-3), respectively. Also monoprotonated molecular ions containing heavier elements such as sulphur (SH⁺) [11, 12] and chlorine (HCl⁺) [13] were detected in the same periods. The silicon monohydride molecular ion, SiH⁺ was first detected in the solar photospheric spectrum in the '70s [14]. Its presence in the ISM was predicted by Almeida *et al.* soon after [15] but, until now, it has not been detected.

The spectroscopic techniques used to probe the chemical composition of the ISM are various: they include rotational, rotovibrational, infrared and X-ray spectroscopies. The latter is used to investigate the hot phase region since, during the cooling process, X-ray emission occurs. This phase is characterized by the so-called *astrophysical plasma*.

The molecular ions are also present in the *laboratory plasma*. The methylidene molecular ion, CH⁺, is important in magnetic fusion plasma [16] and in the production of carbon nanocone array [17] and carbon nanotubes [18] when plasma technique such as Plasma Enhanced Chemical Vapour Deposition (PECVD) are used. Plasma techniques are also used in silicon nanocrystal formation [19] and in the functionalization [20] and deposition of silicon on surfaces [21, 22, 23]. The production of silicon molecular ion in the silane plasma is well known. As reported in Fig. I.1, in microwave plasma the silane can dissociates to its radicals (SiH₃, SiH₂, SiH, Si) and its molecular ions (SiH₃⁺, SiH₂⁺, SiH⁺, Si⁺) [24]. The silane molecular ion, SiH₄⁺ is an unstable species and undergoes to predissociation forming the SiH₂⁺ ion [25].

As illustrated above, the study of molecular ions is important both on the astrophysical and laboratory plasma.

Different techniques are suitable for the study of the molecular ions and among them we can find the X-ray spectroscopies. These techniques can be used both to the characterization of the solid state structure (X-Ray diffraction) and to probe the chemical composition due to its element specificity. The X-ray radiation covers a wide energy range, between 100 and 5×10^5 eV, and it permits to study sample containing different elements and their chemical environment. It can be used in the absorption or emission regime according to which we can define different

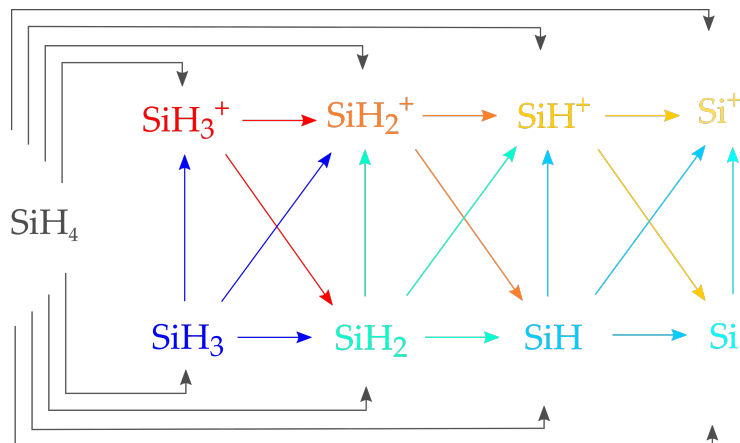


Figure I.1: Fragmentation pathways of silane molecule, SiH_4 , in microwave plasma (from ref. [24])

techniques such as X-ray Absorption Near Edge Structure (XANES), X-ray Photoelectron Spectroscopy (XPS) or X-ray Fluorescence spectroscopy (XFS).

There are different X-ray sources (tube, laser, synchrotron) which may be classified according to their *brightness*. The synchrotron radiation provides an excellent X-ray source since it has high brightness, monochromatization and spectral resolution (in the order of meV).

The scope of this thesis work is to study theoretically the X-ray photoabsorption spectrum features of Carbon, Oxygen and silicon protonated molecular ions generally labelled as XH_n^+ ($X = \text{C}, \text{O}, \text{Si}; n = 1, 2, 3$). The ground and valence excited states properties have been studied [26, 27, 28, 29] but up to now neither theoretical nor experimental works have been reported on the core-excited states.

This thesis work was carried out in collaboration with two experimental groups in University of Paris-Sud (J.-M. Bizau, D. Cubaynes, S. Guilbaud) and Dublin City University (E. Kennedy, J.-P. Mosnier, P. Van Kampen). These teams study on the production of atomic and molecular ions through the use of an Electron Cyclotron Resonance Ion Source (ECRIS). Characterization of these species is done with X-ray absorption spectroscopy. The experimental data were recorded using the Multi-Analysis Ion Apparatus (MAIA) set-up (Fig. I.2) [30] which is permanently installed on the Pléiades beam line at the synchrotron facility of SOLEIL in St. Aubin (Paris, France) [31].

A detailed description of the experimental set-up goes beyond the scope of this thesis but can be found in ref. [32]. In general, the molecular ions were produced in the ECRIS source

(ECRIS in Fig. I.2). Neutral molecular gas CH_4 , H_2O and SiH_4 were used to form in the source the C, O and Si molecular ions, respectively. The molecular ions are produced via ionization dissociation pathways such as the one reported in Fig. I.1 for SiH_4 . After the ECRIS source, one particular molecular ion can be selected by the magnets present in the MAIA analyser (Magnet 1 in Fig. I.2). The selected molecular ion is then driven in the Interaction Region (IR in Fig. I.2) where the interaction with the synchrotron radiation takes place. After core-excitation in this region, the excited system undergoes to Auger decay (de-excitation process) which generally leads to the fragmentation of the molecular ion. The experimental set-up was calibrated in order to detect the double charged atomic ion (X^{2+}). Assuming that this is the only product of the fragmentation, absolute cross sections can be deduced. The experimental cross section is therefore determined by the quantification of photoions X^{2+} detected (Detector in Fig I.2) with respect to the parent ions.

Fragmentation of the neutral molecules in the ECRIS source leads to the formation of radicals (non-detectable in MAIA apparatus) and cations. The latter can be in their ground state or in the lowest valence excited state having a different spin multiplicity than the ground state, also referred as *metastable states*. Generally these metastable states present lifetimes in the order of ms (10^{-3} s) [33, 34]. They are therefore detectable in MAIA since the time-of-flight between the ECRIS source and the interaction region is in the order of μs (10^{-6} s).

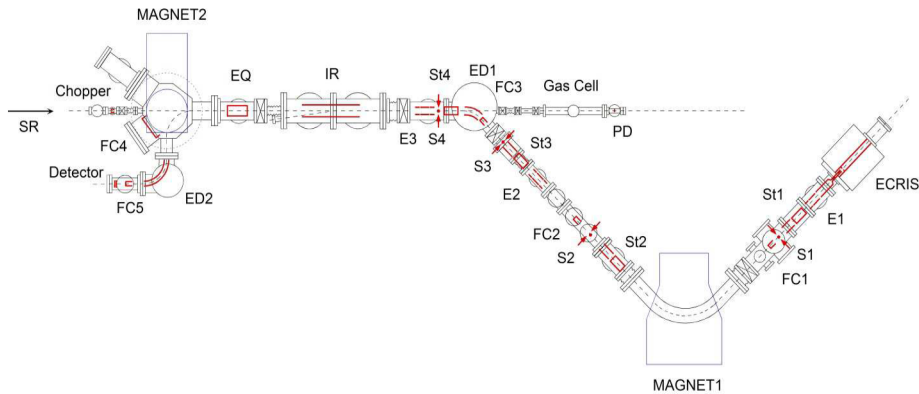


Figure I.2: Scheme of Multi-Analysis Ion Apparatus (MAIA) set-up from ref. [30]. ECRIS: Electron Cyclotron Resonance Ion Source, E: einzel lens, St: set of vertical and horizontal steerers, FC: Faraday cups, S: collimating slits, ED: electrostatic deflector, IR: interaction region, EQ: electrostatic quadrupole, SR: synchrotron radiation, PD:calibrated photodiode

The main goal of this thesis is to develop theoretical protocols which provide X-ray photoabsorption spectra at different edge (1s and 2p shell) by combination of electronic structure and nuclear wavepacket propagation techniques. Given the possibility to produce metastable states in the ECRIS source, it was necessary to find a procedure to include them in the theoretical approach.

The thesis is divided into two parts: *theoretical background* and *results and discussion*. In Chapter 1 a description of the core shell phenomena is provided (core-excitation and resonant Auger decay) and the concept of photoabsorption cross section is introduced.

In Chapter 2, the formula to compute cross sections in the time independent and time dependent approaches is presented. Starting from the Time-Dependent (TD) Schrödinger equation, the Time-Independent (TI) Schrödinger equation is derived. The Born-Oppenheimer approximation (BOA) and the Potential Energy Surface (PES) are then introduced. The Chapter proceeds with the discussion of the equivalence between the photoabsorption cross section computed in the TI and TD approximation.

In Chapter 3, the electronic structure methods used as tools throughout the works are presented. The chapter starts with the description of the Hartree-Fock theory for closed and open shell systems. The reader is then driven up to the more correlated methods such as Configuration Interaction (CI) and Multi-Configurational Self Consistent Field (MCSCF).

In Chapter 4, the application of the electronic structure and wavepacket propagation methods to the calculations of core-excited spectra is presented. The X-ray photoabsorption spectra of the 1s and 2p shell, also labelled K and L respectively, present different problems and then have to be treated separately. First, a detailed description of the protocols used in the simulation of the photoabsorption spectra on the K-shell is reported where the simple system CH^+ was used as case study. The choice of the best set of spin-orbitals and the dynamics of the excited states were investigated using different approaches. In the following, the L-shell protocol was optimized working on the case study SiH^+ . For this edge, it is crucial to take into account the spin-orbit coupling interaction but the computational resources to include it are not negligible. To this purpose we investigate the best balance between the spin-orbit coupling operator and the number of active electrons to be explicitly considered. The development of an effective Hamiltonian for the calculation of the 2p ionization threshold is also presented, even if this work is still on going.

The results and discussion of the calculations of the K- and L-edge X-ray photoabsorption spectra are discussed in Chapter 5 and 6 respectively. The calculations of the L-shell ionization

threshold for the silicon molecular ions are reported in Chapter 7.

Finally, conclusions are drawn and perspectives for future works are envisaged.

Theoretical background

“Explain it! The most important thing is, that you are able to explain it! [...] So learn to explain it! You can train this by explaining to another student, a colleague. If they are not available, explain it to your mother - or to your cat!”

— Rudolf Ludwing Mössbauer - 1984

1 Core shell spectroscopy

In this Chapter are presented the fundamental principles of the X-ray absorption spectroscopy. Section 1.1 gives a general introduction on the spectroscopic techniques. The X-ray photoabsorption process is described in detail in section 1.2, the concept of cross section is presented and it will be extensively discussed later in the next chapter. Finally in section 1.3 the processes following the excitation are illustrated focusing in particular on the resonant Auger effect since it is explicitly taken into account in our calculations.

1.1 Spectroscopic techniques

Spectroscopy is the branch of science that studies the interaction between radiation and matter. Depending on the energy of the incoming radiation, which are shown in Fig. 1.1, we distinguish different type of spectroscopic tools. The incoming radiation is characterized by its wavelength λ or frequency ω which are related to the energy E as follow

$$E = \frac{hc}{\lambda} = \hbar\omega \quad (1.1.1)$$

The Infra-Red (IR) spectroscopy uses low energy photon (Fig. 1.1), thus it is able to excite the molecules *vibrationally*. The IR spectroscopy is generally used for the identification of molecules because it permits to study the vibrational motion of the systems. In order to produce *electronic excitations*, one needs higher energy. For example, the Ultra Violet - Visible (UV-vis) region corresponds to valence excitation while X-ray photons allows the promotion of the core electron to empty levels. The former type of spectroscopy gives information about the bond structure of the molecules (e.g. presence of double bonds) while the latter provides information about the chemical environment of a selected types of atoms in molecules. This

permits to obtain information about a specific atomic site and, for example, it allows the study of a wide range of systems from free molecules with different size containing different sites [35, 36, 37] to solid state systems [38, 39].

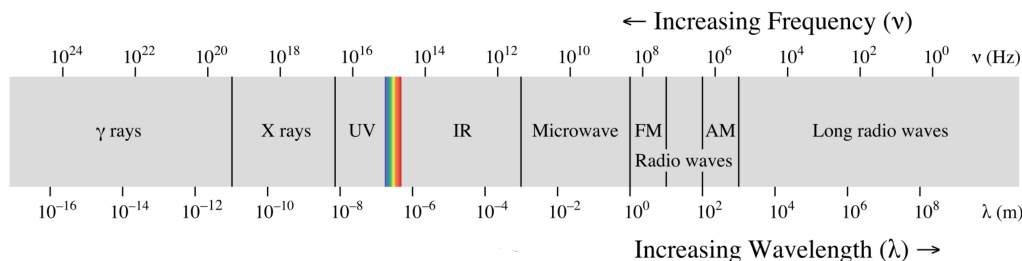


Figure 1.1: The electromagnetic spectrum.

In what follow, we will focus on X-ray spectroscopy which, as seen in the previous chapter, is a powerful tool for the investigation of laboratory and astrophysical plasma. It is in this last case that this thesis takes place.

The range of the X-ray radiation covers energies between 100 and 5×10^5 eV which can be divided into *soft* and *hard* X-ray region below and above the 1000 eV, respectively. Depending on the energy of the incoming X-ray photon, different processes can occur. Two scenarios are possible : (I) the energy of the incoming photon is higher than the Ionization Potential (IP) of the core electron, which allow to eject the latter in the continuum or (II) the incoming photon has a energy such that the electron is resonantly excited to an unoccupied orbital. The two processes are called *photoionization* and *photoexcitation*, respectively, and are schematically shown in Fig. 1.2.A and 1.2.B, respectively. The electron involved in the photoionization or photoabsorption process is labelled according to its principal quantum number. Thus we distinguish K or L-shell excitation. The energy required to excite or ionize the electron depends on the atomic number Z of the studied atom and this make the technique atom specific. For example, the K-edge of the lighter elements (Be - Ne, $Z \leq 10$) as well as the L-edge for the third/fourth row elements (Na - Cu, $Z < 29$) occur below 1000 eV. [40]

1.2 The X-ray photoabsorption process

In the photoabsorption process an electron is promoted from a core to an unoccupied Molecular Orbital (MO) by the energy of the X-ray photon. The transition probability per unit of time

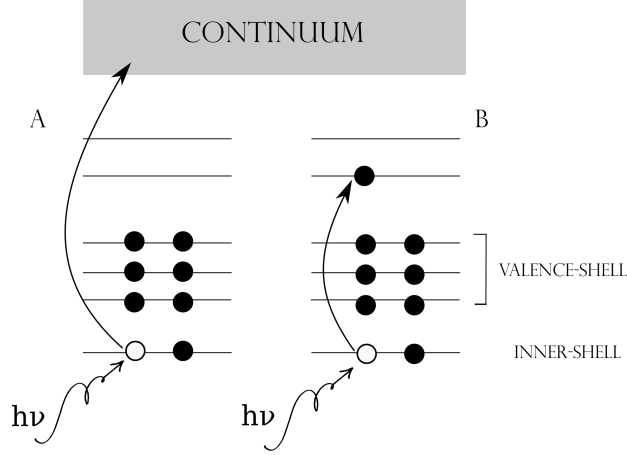


Figure 1.2: Representation of the X-ray photoionization (A) and photoexcitation (B) processes.

($P_{i \rightarrow f}$) between the initial state i and the final state f is given by the *Fermi's Golden rule* [41] :

$$P_{i \rightarrow f} = \frac{2\pi}{\hbar} |\langle f | \hat{\mathbf{M}} | i \rangle|^2 \delta(\hbar\omega + E_i - E_f) \quad (1.2.1)$$

where $|i\rangle$ and $|f\rangle$ are the wavefunction of the initial and final state, respectively, $\hat{\mathbf{M}}$ is the operator that describes the interaction between the radiation and the system, $\hbar\omega$ is the energy of the incoming photon, E_i and E_f are the energies of the initial and final states, respectively and their difference $E_i - E_f$ is defined as ω_{if} .

In the *dipole approximation* [42] the matrix element M_{fi} can be written in terms of linear momentum operator of the electrons $\mathbf{p} = m_e \dot{\mathbf{r}}$

$$M_{fi} = \frac{i}{\hbar} \langle f | \hat{\boldsymbol{\varepsilon}} \cdot \mathbf{p} | i \rangle = \frac{im_e}{\hbar} \hat{\boldsymbol{\varepsilon}} \langle f | \dot{\mathbf{r}} | i \rangle \quad (1.2.2)$$

where m_e is the mass of the electron. In Eq. 1.2.2, $\hat{\boldsymbol{\varepsilon}}$ is the polarization vector of the electromagnetic wave. Applying the Heisenberg equation of motion to the operator $\dot{\mathbf{r}}$

$$\dot{\mathbf{r}} = \frac{1}{i\hbar} [\mathbf{r}, H_0] \quad (1.2.3)$$

where \mathbf{r} is the position vector and H_0 is the unperturbed Hamiltonian of the system, we obtain

$$\langle f | \dot{\mathbf{r}} | i \rangle = \frac{1}{i\hbar} (E_i - E_f) \langle f | \mathbf{r} | i \rangle = i\omega_{if} \mathbf{r} \quad (1.2.4)$$

which is true if $|i\rangle$ and $|f\rangle$ are eigenstates of H_0 . Thus the matrix element M_{fi} can be rewritten as

$$M_{fi} = -\frac{m_e \omega_{fi}}{\hbar} \langle f | \hat{\boldsymbol{\varepsilon}} \mathbf{r} | i \rangle = \frac{m_e \omega_{fi}}{\hbar e} \langle f | \hat{\boldsymbol{\varepsilon}} \boldsymbol{\mu} | i \rangle = \frac{m_e \omega_{fi}}{\hbar e} \hat{\boldsymbol{\varepsilon}} \langle f | \boldsymbol{\mu} | i \rangle \quad (1.2.5)$$

where the operator $\boldsymbol{\mu}$ is the *electric dipole moment operator* in the length gauge.

The *absorption cross section* $\sigma(\omega)$ for the system (atoms or molecules) is equal to the number of excited electrons per unit time divided by the number of incident photons per unit time per unit area [43, 42]:

$$\sigma(\omega) = \frac{4\pi^2 \hbar^2 \alpha}{m_e^2 \omega_{fi}} |M_{fi}|^2 \delta(\hbar\omega + \omega_{if}) \quad (1.2.6)$$

where $\alpha = e^2/\hbar c$ is the fine structure constant ($\simeq 1/137$), the δ function ensures energy conservation (i.e. $E_f = E_i + \hbar\omega$). The cross section is usually given in units of cm^2 or in *barn* ($1 cm^2 = 10^{24} barn$).

1.3 The Resonant Auger effect

The X-ray photoabsorption is generally followed by two de-excitation processes: *resonant Auger decay* (non radiative) and *fluorescence* (radiative) with rates ω_A and ω_F , respectively [43, 44]. The yield of the above presented phenomena depends strongly on the atomic number Z and the general trend for the de-excitation processes with respect to Z [40] is reported in Fig. 1.3. The Auger decay channel is dominant in the case of K-shell excitation of the lighter atoms ($Z < 10$) and L-shell excitation of atoms with $Z < 90$ [45].

Generally, both the resonant Auger effect and the fluorescence contribute to the line broadening of the photoabsorption cross section. Lines in the absorption cross-section appear as a Lorentzian distribution $L(\omega; \Gamma)$ with a Full Width at Half Maximum (FWHM) Γ .

$$\sigma(\omega) = \frac{4\pi^2 \hbar^2 \alpha}{m_e^2 \omega_{fi}} |M_{fi}|^2 L(\omega; \Gamma) \quad (1.3.1a)$$

$$= \frac{4\pi^2 \hbar^2 \alpha}{m_e^2 \omega_{fi}} |M_{fi}|^2 \frac{1}{\pi} \frac{\frac{1}{2}\Gamma}{(\omega - \omega_{fi})^2 + (\frac{1}{2}\Gamma)^2} \quad (1.3.1b)$$

Γ is inversely proportional to the core-hole life time

$$\Gamma = \frac{1}{\tau} = \frac{1}{\tau_A} + \frac{1}{\tau_F} \quad (1.3.2)$$

where τ_A and τ_F are the contribution to the core-hole life time from the resonant Auger effect and fluorescence, respectively.

For the lighter atoms, the core-hole life time is mainly due to the Auger decay and its magnitude is on the femtosecond time scale ($\sim 10^{-15}s$) [45] which produce a broadening of the spectral line shape of the order of 100 meV.

In the Auger process, the promoted electron can de-excite resonantly or participate or not to other decay pathways. In the last two cases it is called *participator Auger electron* and *spectator Auger electron*, respectively. In other channels, the excited electron can be ejected in the continuum or further excited to a level with higher or lower energy [46]. These three process are labelled *shake-off*, *shake-up* and *shake-down*, respectively. All the possible processes are illustrated in Fig.1.4.

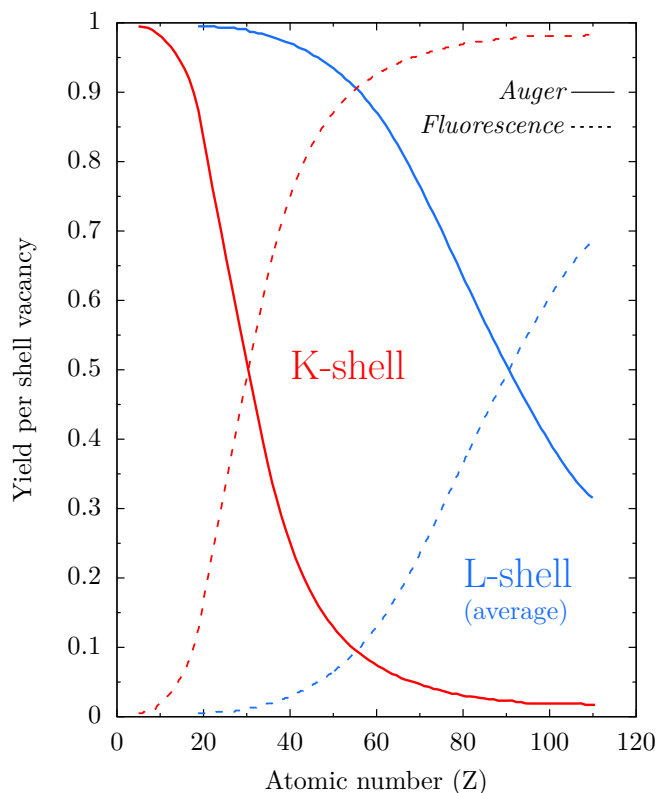


Figure 1.3: Fluorescence and Auger yield for atoms with $Z < 120$ (from ref. [45]).

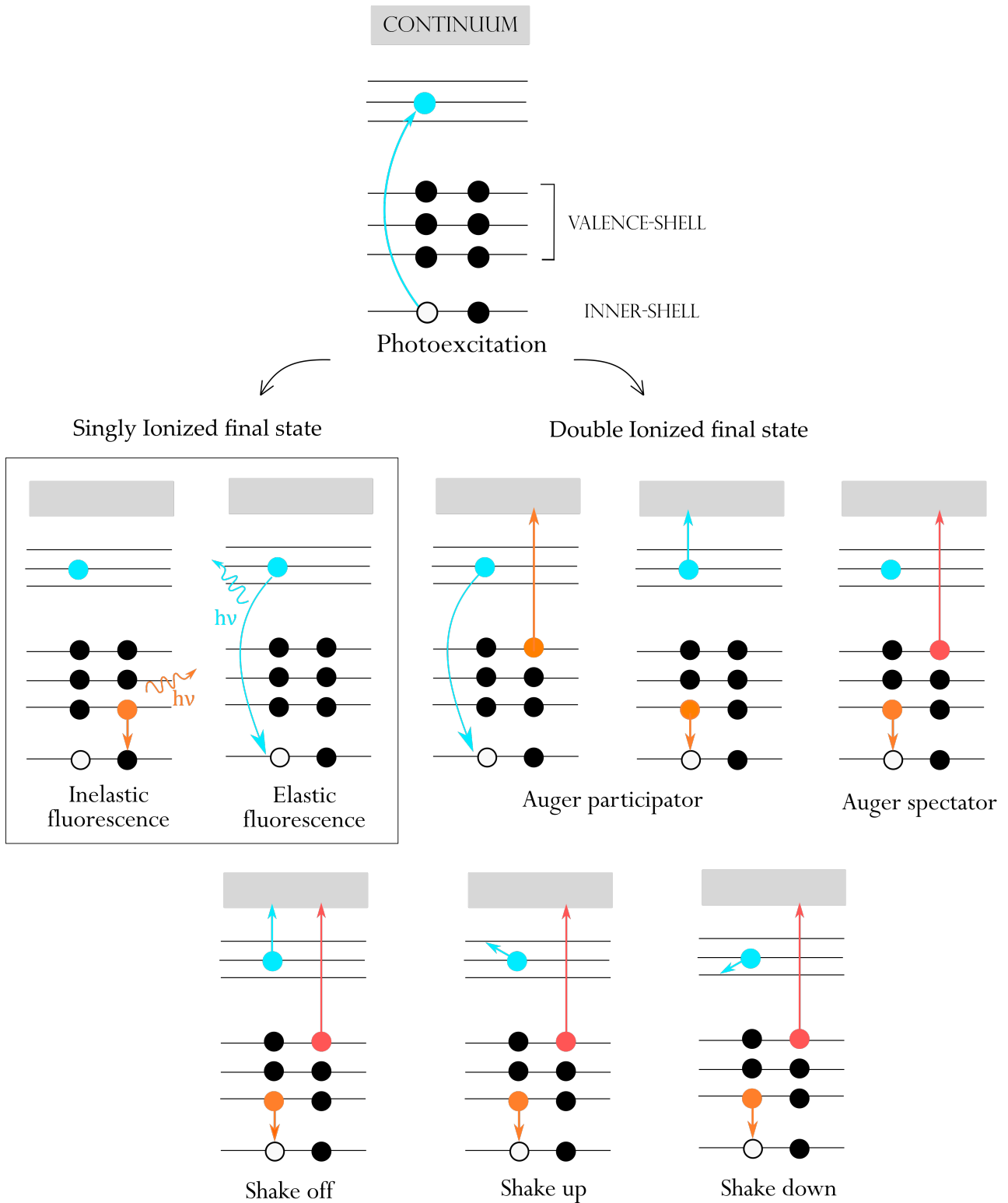


Figure 1.4: Schema of the photoabsorption process followed by the possible de-excitation ways.

2 From the Schrödinger equation to the photoabsorption cross section

In this Chapter is presented the relation between the photoabsorption cross section and Schrödinger equation both in the time dependent (TD) and the time independent (TI) pictures. A general picture of the Schrödinger equation is presented in Section 2.1 where it is introduced in the time dependent and time independent forms. In Section 2.2, the time independent picture is treated in details. The concept of potential energy surface which appears in the Born-Oppenheimer approximation (BOA) is presented in Section 2.2.1 with a focus on its expression in the Harmonic Approximation (HA). In Section 2.3.1 and 2.3.2 are illustrated the way to take into account the nuclear dynamics in the TI and TD regime, respectively. Finally, the calculation of the photoabsorption cross section is elucidated in Section 2.4.

2.1 The Schrödinger Equation

The properties of a system can be studied through the resolution of the differential equation called Time-Dependent Schrödinger Equation (TDSE)

$$i\hbar \frac{\partial}{\partial t} |\Psi\rangle = i\hbar |\dot{\Psi}\rangle = \hat{H} |\Psi\rangle \quad (2.1.1)$$

where \hat{H} is the Hamiltonian operator

$$\hat{H} = \hat{T} + \hat{V} \quad (2.1.2)$$

where \hat{T} is the kinetic energy operator and \hat{V} is the potential energy operator which does not depend on time in the approximation reported here.

Generally the wavefunction depends on the system coordinate \mathbf{r} and the time t . For a one-dimensional system \mathbf{r} can be replaced by one spatial coordinate \mathbf{x} . This simplification permits to better explain the resolution of the TDSE by variable separation. This technique leads to a particular solution of the equation that can be used to predict the time dependent observables.

The wavefunction $\Psi(\mathbf{x}, t)$ can be expressed as the product of two functions depending separately on coordinates and time, $\psi(\mathbf{x})$ and $\vartheta(t)$ respectively.

$$|\Psi\rangle = |\vartheta\rangle|\psi\rangle \quad (2.1.3)$$

Introducing this wavefunction expression in Eq. 2.1.1 we obtain

$$i\hbar \frac{|\dot{\vartheta}\rangle}{|\vartheta\rangle} = \hat{H} \frac{|\psi\rangle}{|\psi\rangle} \quad (2.1.4)$$

The two sides of Eq. 2.1.4 must be equal to the same constant, the energy E .

$$i\hbar \dot{\vartheta}(t) = E\vartheta(t) \quad (2.1.5)$$

$$\hat{H}|\psi\rangle = E|\psi\rangle \quad (2.1.6)$$

Eq. 2.1.6 is the Time-Independent Schrödinger Equation (TISE). It is an eigenvalue equation where $\psi(\mathbf{x})$ is the eigenfunction related to the eigenvalue E .

The Eq. 2.1.5 has an analytical solution

$$|\vartheta\rangle = |\vartheta_0\rangle e^{-\frac{i}{\hbar}Et} \quad (2.1.7)$$

The solution of the TDSE, called *particular solution*, can be written as follow

$$|\Psi\rangle = |\psi\rangle|\vartheta_0\rangle e^{-\frac{i}{\hbar}Et} \quad (2.1.8)$$

where ϑ_0 is a constant and it can be included in $\psi(\mathbf{x})$. Its magnitude is determined in the TISE and it is chosen in order to fulfil the normalization condition

$$\langle\Psi|\Psi\rangle = 1 \quad (2.1.9)$$

2.2 Time-Independent Schrödinger Equation and Born - Oppenheimer approximation

The energy of a system of N nuclei and n electrons can be reached solving the TISE using the Hamiltonian operator described by the position vectors of the electrons \mathbf{r} and nuclei \mathbf{R} . The Hamiltonian operator has the form

$$\hat{H} = \sum_{i=1}^n -\frac{\hbar^2 \nabla_{e,i}^2}{2m_e} + \sum_i \sum_{j>i} \frac{e^2}{|\mathbf{r}_i - \mathbf{r}_j|} - \sum_{I=1}^N \frac{\hbar^2 \nabla_{N,I}^2}{2M_I} + \sum_I \sum_{J>I} \frac{Z_I Z_J e^2}{|\mathbf{R}_I - \mathbf{R}_J|} - \sum_i \sum_I \frac{Z_I e^2}{|\mathbf{r}_i - \mathbf{R}_I|} \quad (2.2.1)$$

where m_e and M are the electron and nuclei masses, Z is the atomic number of the nuclei and $\nabla_{e,i}$ and $\nabla_{N,i}$ are the Laplacian operators associated to the electronic and nuclear coordinates, respectively. The first two terms are the kinetic energy operator for the electrons (\hat{T}_e) and the electron-electron repulsion potential operator (\hat{V}_e), respectively. The third and fourth terms describe the kinetic energy operator for the nuclei (\hat{T}_N) and the nucleus-nucleus repulsion potential (\hat{V}_N) operators, respectively. The last term of the Eq. 2.2.1 represents the electron-nuclei attraction (\hat{V}_{eN}).

The Hamiltonian can be rewritten in terms of electronic and nuclear Hamiltonian

$$\hat{H} = \hat{H}_{elect} + \hat{H}_{nucl} \quad (2.2.2)$$

where

$$\hat{H}_{elect} = \hat{T}_e + \hat{V}_e + \hat{V}_{eN} \quad (2.2.3a)$$

$$\hat{H}_{nucl} = \hat{T}_N + \hat{V}_N \quad (2.2.3b)$$

In the Born-Oppeneimer approximation (BOA) the wavefunction can be expressed in terms of full adiabatic wavefunction $\varphi(\mathbf{r}; \mathbf{R})\phi(\mathbf{R})$ where $\varphi(\mathbf{r}; \mathbf{R})$ and $\phi(\mathbf{R})$ are the electronic and nuclear wavefunctions, respectively.

Inserting this ansatz in the TISE and projecting on $\phi(\mathbf{R})$ we obtain an eigenvalue equation which gives the electronic energy of the system

$$\hat{H}_{elect}\varphi(\mathbf{r}; \mathbf{R}) = E_{elect}(\mathbf{R})\varphi(\mathbf{r}; \mathbf{R}) \quad (2.2.4)$$

Similarly, integrating over the electronic degrees of freedom (dof) we obtain

$$\hat{H}^{BOA}(\mathbf{R})\phi(\mathbf{R}) = (E_{elect}(\mathbf{R}) + \hat{V}_N + \hat{T}_N)\phi(\mathbf{R}) \quad (2.2.5)$$

The Hamiltonian operator in Eq. 2.2.5 is called *adiabatic Hamiltonian* where the total energy is expressed as sum of the electronic energy and a constant potential of the nuclei. The aforementioned approximation is called *Born-Oppenheimer approximation* (BOA) or *adiabatic approximation*. In such approximation, we assume that under normal conditions the electronic motion is much faster than the nuclear ones because the mass of the nuclei are much heavier than electrons. In this condition, the electronic rearrangement arises almost instantaneously compared to the nuclear motion.

The resolution of the TISE (Eq. 2.1.6) is one of the big challenge in quantum chemistry and, to this purpose, different methods have been developed. The electronic problem will be treated more deeply in the next chapter.

2.3 Potential energy surface approximation

The calculation of the total energy as function of the nuclear positions leads to the *potential energy surface* (PES). For a general system A - B, we can have different types of PES. Those who have a minimum are labelled *bound* otherwise they are called *dissociative*. In the first case (Fig. 2.1 - bottom), the minimum of the PES is at the equilibrium distance and the molecule is stable in this electronic configuration. In the second case, the molecule is unstable and it undergoes dissociation (Fig. 2.1 - top).

For a system of N atoms, the PES depends on the 3N Cartesian coordinates labelled \mathbf{x} . In case of the ground state PES, the potential can be approximated by a Taylor expansion

$$V(\mathbf{x}) = V(x_0) + \sum_k (x_k - x_0) \frac{\partial V}{\partial x_k} + \frac{1}{2} \sum_{k,l} (x_k - x_0)(x_l - x_0) \frac{\partial^2 V}{\partial x_l \partial x_k} + \dots \quad (2.3.1)$$

where $V(x_0)$ is the potential energy at the equilibrium geometry, the second term is the gradient of the energy along the x_k coordinate and the third term is the second derivative with respect to the coordinates x_k and x_l . The first-order term is zero as the expansion is performed around the minimum of the potential. The terms above the second-order are small enough to be neglected as long as we are interested to the region around the equilibrium geometry and we can work

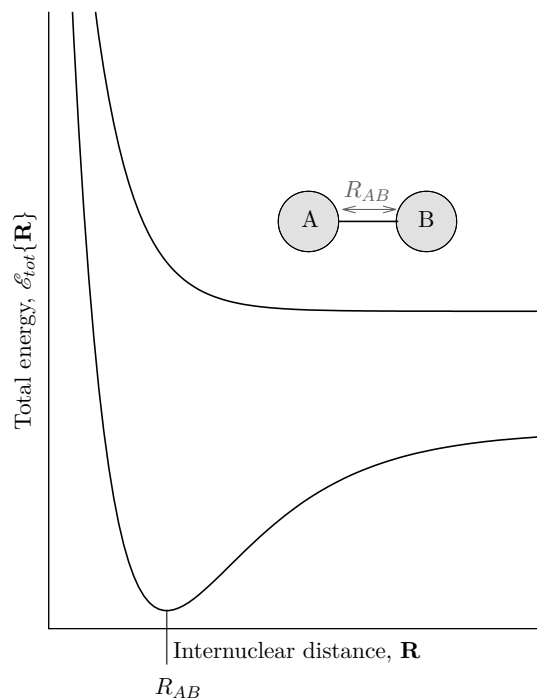


Figure 2.1: General example of PESs with and without a minimum, bottom and top respectively.

in the so-called *harmonic approximation* (HA). In Eq. 2.3.1 the second derivative is usually written as a matrix called *Hessian* which has a dimensions $3N \times 3N$.

$$\mathbf{Hess} = \begin{bmatrix} \frac{\partial^2 V}{\partial x_1^2} & \frac{\partial^2 V}{\partial x_k \partial x_l} & \cdots & \frac{\partial^2 V}{\partial x_k \partial x_N} \\ \frac{\partial^2 V}{\partial x_l \partial x_k} & \frac{\partial^2 V}{\partial x_l^2} & \cdots & \frac{\partial^2 V}{\partial x_l \partial x_N} \\ \vdots & \vdots & \ddots & \vdots \\ \frac{\partial^2 V}{\partial x_N \partial x_k} & \cdots & \cdots & \frac{\partial^2 V}{\partial x_N^2} \end{bmatrix} \quad (2.3.2)$$

The Eq. 2.3.1 can be rewritten as follow:

$$V = V_0 + \frac{1}{2} \mathbf{x}^T \mathbf{Hess} \mathbf{x} \quad (2.3.3)$$

where the vector \mathbf{x} is the displacement of the coordinates x .

The diagonalization of the **Hess** matrix gives the eigenvalues λ_N and eigenvectors \mathbf{P} .

Using the eigenvectors of **Hess** it is possible to define a new set of coordinates corre-

sponding to the projection of the atomic positions on a new set of axes. These new coordinates are called *normal coordinates* \mathbf{Q} . The eigenvalues λ_k are the force constant associated to the normal mode \mathbf{Q}_k and are related to the *normal mode frequency* ω_k

$$\omega_k = \sqrt{\frac{\lambda_k}{\mu_k}} \quad (2.3.4)$$

where μ_k is the reduced mass associated to the normal mode.

The normal modes are independent of each other and each mode acts as a simple harmonic oscillator, which simplify considerably the problem.

Molecules have $3N$ normal modes. For linear molecules three of them are the coordinates for the motion of the center of mass and two are the rotational angle, the last one are three for non linear molecules. The *vibrational normal modes* for linear and non linear molecules are thus $3N - 5$ and $3N - 6$, respectively.

In this thesis work, we defined the PES of excited states in this normal coordinates. For bound excited states we keep the three terms in Eq. 2.3.1 while only the first two terms are used for dissociative states.

2.4 Cross section

2.4.1 Cross section in the time-independent approach

As previously shown in the time independent approach, the transition dipole moment integral can be written as

$$M_{fi} = \frac{m_e \omega_{fi}}{\hbar e} \hat{\epsilon} \langle f | \boldsymbol{\mu} | i \rangle \quad (2.4.1)$$

Within the BOA, each wavefunctions can be factorized as product of electronic and nuclear wavefunction $\varphi(\mathbf{r}; \mathbf{R})$ and $\phi(\mathbf{R})$, respectively. Moreover, the dipole moment operator can expressed as the sum of the electronic and nuclear components

$$\boldsymbol{\mu} = \boldsymbol{\mu}_e + \boldsymbol{\mu}_N \quad (2.4.2a)$$

$$= -e \sum_i \mathbf{r}_i + e \sum_I Z_I \mathbf{R}_I \quad (2.4.2b)$$

Applying these approximations, the Eq. 2.4.1 becomes

$$M_{fi} = \int \int d\mathbf{R} d\mathbf{r} \phi_f^*(\mathbf{R}) \varphi_f^*(\mathbf{r}; \mathbf{R}) \boldsymbol{\mu}_e \varphi_i(\mathbf{r}; \mathbf{R}) \phi_i(\mathbf{R}) \quad (2.4.3a)$$

$$+ \int \int d\mathbf{R} d\mathbf{r} \varphi_f^*(\mathbf{r}; \mathbf{R}) \phi_f^*(\mathbf{R}) \boldsymbol{\mu}_N \phi_i(\mathbf{R}) \varphi_i(\mathbf{r}; \mathbf{R}) \quad (2.4.3b)$$

where the two integrals are on the nuclear and electronic degree of freedom. As $\boldsymbol{\mu}_N$ acts only on the nuclear coordinates, the Eq. 2.4.3b goes to zero because of the orthonormality of the initial and final electronic wavefunctions. The Eq. 2.4.3a can be rewritten as follow

$$M_{fi} = \int d\mathbf{r} \varphi_f^*(\mathbf{r}; \mathbf{R}) \boldsymbol{\mu}_e \varphi_i(\mathbf{r}; \mathbf{R}) \int d\mathbf{R} \phi_f^*(\mathbf{R}) \phi_i(\mathbf{R}) \quad (2.4.4)$$

From the first integral, we obtain the electronic dipole moment transitions

$$\boldsymbol{\mu}_e^{fi}(\mathbf{R}) = \int d\mathbf{r} \varphi_f^*(\mathbf{r}; \mathbf{R}) \boldsymbol{\mu}_e \varphi_i(\mathbf{r}; \mathbf{R}) \quad (2.4.5)$$

Applying the *Condon approximation* [47, 48, 49], we can neglect the dependence of the electronic dipole moment on the nuclear coordinates. Thus, Eq. 2.4.5 can be approximate to the value of the electronic dipole moment transition at the equilibrium distance $\boldsymbol{\mu}_e(\mathbf{R}_{eq})$. Within these approximation, Eq. 2.4.4 can be rewritten as

$$M_{fi} = \boldsymbol{\mu}_e^{fi}(\mathbf{R}_{eq}) \int d\mathbf{R} \phi_f^*(\mathbf{R}) \phi_i(\mathbf{R}) = \boldsymbol{\mu}_e^{fi}(\mathbf{R}_{eq}) \langle \phi_f | \phi_i \rangle \quad (2.4.6)$$

In Eq. 2.4.6, the square of the overlap integral $\langle \phi_f | \phi_i \rangle$ is named Franck-Condon (FC) factor.

In Fig. 2.2a, it is presented a pictorial representation of the vibrational levels for an harmonic oscillator where the vibrational wavefunctions for electronic initial and final states are labelled ν_i and ν'_i , respectively. The initial nuclear wavepacket is centered around the equilibrium internuclear distance R_{eq} and the PES region involved in the vertical transition is called *Franck-Condon region*. The PESs of initial and final states may not be parallel and it follows that the transition with the higher intensity is the one which has the largest overlap with ϕ_{ν_i} . The resulting FC factor distribution is reported in Fig. 2.2b.

Let us consider here a general case of the A-B system with only one normal mode ($3N-5 = 1$). Using the FC approximation, the spectrum for the transitions from the ground ν_0 to the excite ν' vibrational state is proportional to the absolute square value of the FC factors (Eq. 2.4.6). It can be simulated using a Voigt's profile which takes into account of the natural and experimental broadening in the Lorentzian and Gaussian part, respectively.

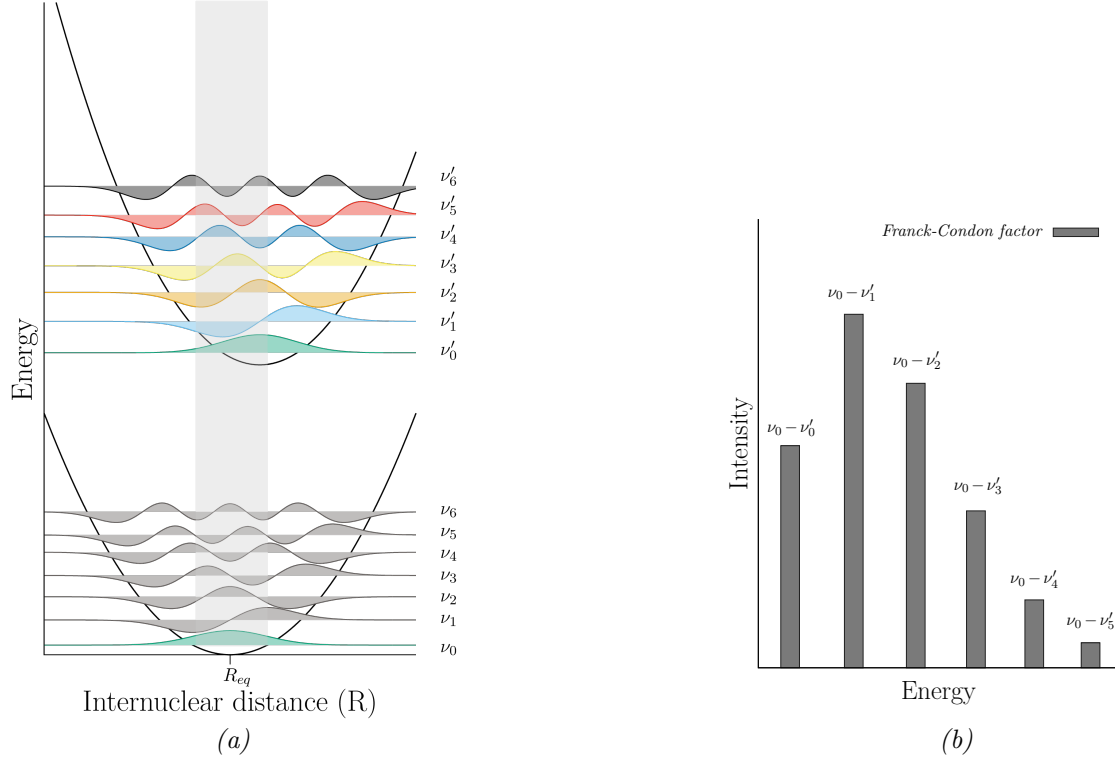


Figure 2.2: *a.* Vibrational levels ν of potential energy surfaces of ground and excited states in the harmonic oscillator approximation. The prime labels the vibrational levels of the excited state and the grey zone is the Franck-Condon region. *b.* Franck-Condon factor for the transitions between ν_0 and ν'_n ($n \geq 0$) in Fig. 2.2a

$$\sigma(\omega) = \frac{4\pi^2 \hbar^2 \alpha}{m_e^2 \omega_{fi}} \frac{1}{3} \mu_{fi}^2 \sum_{\nu'} |\langle \phi_{\nu'} | \phi_{\nu_0} \rangle|^2 \int \frac{e^{-4 \ln 2 (E - \omega + (\omega_{fi} + \Delta_\nu))^2 / \xi^2}}{2\xi} \frac{1}{\pi} \frac{\frac{1}{2}\Gamma}{[E - \omega + (\omega_{fi} + \Delta_\nu)]^2 + (\frac{1}{2}\Gamma)^2} dE \quad (2.4.7)$$

where ω is the photon energy, ξ and Γ are the FWHM of the Gaussian and Lorentzian profiles, respectively. $\omega_{fi} = E_f - E_i$ is the energy difference between the final and initial electronic states (*vertical energy*) and $\Delta_\nu = E_{\nu'} - E_{\nu_0}$ is the energy difference between the excited and ground vibrational levels. The factor 1/3 takes into account the rotational averaging of the system.

In case of the nuclear dynamics is negligible ($|\langle \nu'_0 | \nu_0 \rangle|^2 \approx 1$), the photoabsorption cross section can be rewritten as

$$\sigma(\omega) = \frac{4\pi^2\hbar^2\alpha}{m_e^2\omega_{fi}} \frac{1}{3}\mu_{fi}^2 \int \frac{e^{-4\ln 2(E-\omega+\omega_{fi})^2/\xi^2}}{2\xi} \frac{1}{\pi} \frac{\frac{1}{2}\Gamma}{[E-\omega+\omega_{fi}]^2 + (\frac{1}{2}\Gamma)^2} dE \quad (2.4.8)$$

2.4.2 Cross section in linear coupling model approximation

The linear coupling model (LCM) provides a very simple but approximate technique to study the nuclear dynamics of excited states in the TI approach.

The Franck-Condon factor are evaluated in function of *coupling constant* which is related to the gradient associated to the normal mode of the interested PES [50, 51]. The gradient along the normal mode k is

$$\frac{\partial E}{\partial Q_k} = \sum_l \frac{\partial E}{\partial x_l} \frac{A_{lk}}{\sqrt{m_l}} \quad (2.4.9)$$

where A_{lk} is the component associated to the unitary transformation between normal and Cartesian coordinates and l is the sum over the Cartesian coordinates.

In case of PESs which have, for a given normal mode k , same frequencies in the ground and excited states $\omega_k = \omega'_k$, the displacement δq along the normal mode k can be evaluated as follow

$$\delta q_k = \frac{1}{\omega_k^2} \frac{\partial E}{\partial Q_k} \quad (2.4.10a)$$

$$= \frac{1}{\omega_k^2} \sum_l \frac{\partial E}{\partial x_l} \frac{A_{lk}}{\sqrt{m_l}} \quad (2.4.10b)$$

From Eq. 2.4.10a, it is possible define the expression of the coupling constant S_k

$$S_k = \frac{\omega_k \delta q_k^2}{2\hbar} \quad (2.4.11a)$$

$$= \frac{1}{2\hbar\omega_k^3} \left[\sum_l \frac{\partial E}{\partial x_l} \frac{A_{lk}}{\sqrt{m_l}} \right]^2 \quad (2.4.11b)$$

For a system which presents only one normal mode ($k = 1$), the FC factors in the LCM are expressed as

$$|\langle \phi_{\nu'} | \phi_{\nu_0} \rangle|^2 = \frac{S^{\nu'}}{\nu'!} e^{-S} \quad (2.4.12)$$

For a multidimensional system ($k > 1$), the excited state vibrational wavefunction can be rewritten as

$$|\phi_{\nu'}\rangle = \prod_k |\phi_{\nu'_k}\rangle \quad (2.4.13)$$

and Eq. 2.4.12 can be rewritten as

$$|\langle \phi_{\nu'} | \phi_{\nu_0} \rangle|^2 = \prod_k \frac{S_k^{\nu'_k}}{\nu'_k!} e^{-S_k} \quad (2.4.14)$$

When the FC distribution of the transitions toward the excited state is large the vibrational progression can be simulated using a Gaussian profile with FWHM related to the *normal slope* of the involved normal mode

$$\xi_k = 2\sqrt{\ln 2} a_k \left[\sqrt{\mu_k} \frac{\partial E}{\partial Q_k} \right] \quad (2.4.15)$$

where μ_k is the reduced mass associated to the k^{th} normal mode and a_k ($= \sqrt{\hbar/\mu_k\omega_k}$) is the width of the ground state nuclear wavefunction. In general, this case occurs when the excited state is dissociative.

For a system with m excited electronic states, the cross section expression can be generally written as follow

$$\sigma(\omega) = \sum_{m,\nu'}^{bound} \frac{4\pi^2\hbar\alpha}{m_e^2\omega_{mi}} \frac{1}{3} \mu_{mi}^2 |\langle \phi_{\nu'_m} | \phi_{\nu_0} \rangle|^2 \int \frac{e^{-4\ln 2(E-\omega+(\omega_{mi}+\Delta_\nu)^2/\xi^2)}}{2\xi} \frac{1}{\pi} \frac{\frac{1}{2}\Gamma}{[E-\omega+(\omega_{mi}+\Delta_\nu)]^2 + (\frac{1}{2}\Gamma)^2} dE + \quad (2.4.16a)$$

$$\sum_m^{diss} \frac{4\pi^2\hbar\alpha}{m_e^2\omega_{mi}} \frac{1}{3} \mu_{mi}^2 \int \frac{e^{-4\ln 2(E-\omega+\omega_{mi})^2/\xi'^2}}{2\xi'} \frac{1}{\pi} \frac{\frac{1}{2}\Gamma}{[E-\omega+\omega_{mi}]^2 + (\frac{1}{2}\Gamma)^2} dE \quad (2.4.16b)$$

where the two sum are over the excited state with bound and dissociative character, respectively. ξ' takes into account whether the broadening related to the experimental band pass and the one from the normal slope (Eq.2.4.15) and $\omega_{mi} = E_m - E_i$ is the energy difference between the m^{th} and initial electronic states.

2.4.3 Cross section in the time-dependent approach

In the time dependent and weak field regime, the transition between two states can be described using the first-order perturbation theory [52]. The Hamiltonian in the BOA is then expressed

$$\hat{H} = \hat{H}^{BOA} + \hat{H}_1(t) \quad (2.4.17)$$

where \hat{H}^{BOA} is the Hamiltonian in the BOA approximation and \hat{H}_1 is the perturbing term. In the same way, the nuclear wavepacket is defined as

$$\psi(t) = \psi^{(0)}(t) + \psi^{(1)}(t) \quad (2.4.18)$$

where $\psi^{(0)}$ and $\psi^{(1)}$ are the zeroth and first perturbed order nuclear wavepacket.

In the description of the radiation-matter interaction, the perturbing term \hat{H}_1 has the form $\mu\varepsilon(t)$ where μ is the transition dipole moment and ε is the field dependent in time (Eq. 1.2.5). In this process the vector character of the transition dipole moment is neglected.

Within the BOA, for a two state system the unperturbed Hamiltonian can be written as

$$\hat{H}^{BOA} = \begin{pmatrix} \hat{H}_i & 0 \\ 0 & \hat{H}_f \end{pmatrix} \quad (2.4.19)$$

where \hat{H}_i and \hat{H}_f stand for the Hamiltonian of the initial and final state, respectively. The perturbing term can be written as

$$\hat{H}_1 = \begin{pmatrix} 0 & -\mu_{if}\varepsilon^*(t) \\ -\mu_{fi}\varepsilon(t) & 0 \end{pmatrix} \quad (2.4.20)$$

In the TD approach, the nuclear wavepacket ψ is function of the nuclear coordinates \mathbf{R} and time t . Before the excitation, there will be no amplitude in the final electronic state and all the amplitude will be in the initial electronic state

$$\psi(t=0) = \psi^{(0)}(t=0) = \begin{pmatrix} \phi_{v_0} \\ 0 \end{pmatrix} \quad (2.4.21)$$

Combining Eq. 2.4.19, 2.4.20 and 2.4.21, the wavepacket at the first order perturbation

theory is given by

$$\psi^{(1)}(t) = \frac{1}{i\hbar} \int_0^t e^{-\frac{i}{\hbar} \hat{H}^{BOA}(t-t')} \hat{H}_1(t') e^{-\frac{i}{\hbar} \hat{H}^{BOA}(t')} \psi(t=0) dt' \quad (2.4.22a)$$

$$\begin{aligned} &= \frac{1}{i\hbar} \int_0^t \begin{pmatrix} e^{-\frac{i}{\hbar} \hat{H}_i(t-t')} & 0 \\ 0 & e^{-\frac{i}{\hbar} \hat{H}_f(t-t')} \end{pmatrix} \begin{pmatrix} 0 & -\mu_{if} \varepsilon^*(t') \\ -\mu_{fi} \varepsilon(t') & 0 \end{pmatrix} \\ &\quad \times \begin{pmatrix} e^{-\frac{i}{\hbar} \hat{H}_i(t')} & 0 \\ 0 & e^{-\frac{i}{\hbar} \hat{H}_f(t')} \end{pmatrix} \begin{pmatrix} \phi_{\nu_0} \\ 0 \end{pmatrix} dt' \end{aligned} \quad (2.4.22b)$$

$$= \begin{pmatrix} 0 \\ \frac{1}{i\hbar} \int_0^t e^{-\frac{i}{\hbar} \hat{H}_f(t-t')} \{-\mu_{fi} \varepsilon(t')\} e^{-\frac{i}{\hbar} \hat{H}_i(t')} \phi_{\nu_0} dt' \end{pmatrix} \quad (2.4.22c)$$

The vector notation in Eq.s 2.4.22b-2.4.22c can be rewritten as

$$\psi^{(1)}(t) = \frac{1}{i\hbar} \int_0^t e^{-\frac{i}{\hbar} \hat{H}_f(t-t')} \{-\mu_{fi} \varepsilon(t')\} e^{-\frac{i}{\hbar} \hat{H}_i(t')} \phi_{\nu_0} dt' \quad (2.4.23)$$

The meaning of Eq. 2.4.23 is reported in the following. At time $t = 0$ (Fig. 2.3a), before the perturbation, the amplitude ψ is on the initial potential defined by \hat{H}_i and it evolves on it up to the time t' . At $t = t'$, the electric field $\varepsilon(t')$ interacts with the system. The transition dipole moment leads the amplitude to the final potential defined by \hat{H}_f (Fig. 2.3b). Thus the wavepacket will evolve on \hat{H}_f in the time $t' < t$ as a coherent wavepacket (Fig. 2.3c).

The wavepacket in the initial state is an eigenvector of \hat{H}_i and it can be expressed in terms of ν^{th} vibrational level. In that condition, we have $\hat{H}_i \phi_{\nu_0} = E_{\nu_0} \phi_{\nu_0}$ and ϕ_{ν_0} in Eq. 2.4.23 can be replaced by $e^{-\frac{i}{\hbar} E_{\nu_0} t'} \phi_{\nu_0}$

$$\psi^{(1)}(t) = \frac{1}{i\hbar} \int_0^t \{\varepsilon(t') e^{-\frac{i}{\hbar} E_{\nu_0} t'}\} e^{-\frac{i}{\hbar} \hat{H}_f(t-t')} \{-\mu_{fi} \phi_{\nu_0}\} dt' \quad (2.4.24)$$

The term $\{\mu_{fi} \phi_{\nu_0}\} = \zeta_{\nu_0}$ represents the initial wavepacket which evolves on the excited state potential \hat{H}_f and Eq. 2.4.24 can be rewritten in terms of ζ_{ν_0}

$$\psi^{(1)}(t) = -\frac{1}{i\hbar} \int_0^t \{\varepsilon(t') e^{-\frac{i}{\hbar} E_{\nu_0} t'}\} e^{-\frac{i}{\hbar} \hat{H}_f(t-t')} \zeta_{\nu_0} dt' \quad (2.4.25)$$

We further assume that the initial vibrational state ϕ_{ν_0} is vertically excited by a delta function

$$\varepsilon(t') = \delta(t' - t_1) \quad (2.4.26)$$

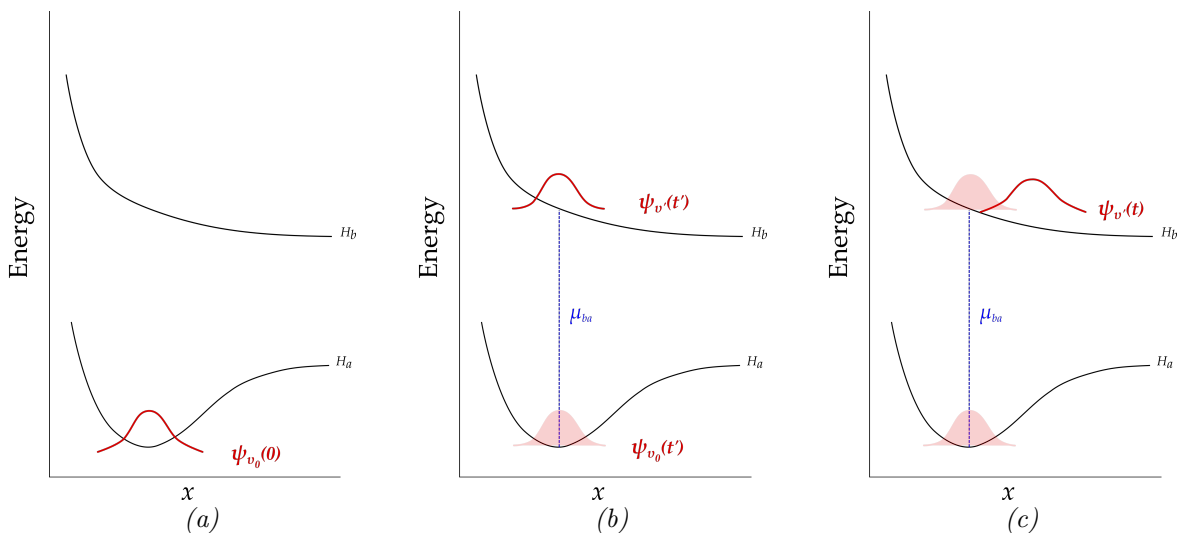


Figure 2.3: Evolution of the nuclear wavepacket ψ . At $t = 0$ the nuclear wavepacket is in the on the initial potential H_i (a). The nuclear wavepacket is excited on the H_f potential by the interaction with the electromagnetic field (b) and it evolve on H_f (c).

and the initial state on the excited potential will be its replica. Substituting Eq. 2.4.26 in Eq. 2.4.25 we obtain

$$\psi^{(1)}(t) = -\frac{1}{i\hbar} e^{-\frac{i}{\hbar} \hat{H}_f(t-t_1)} e^{-\frac{i}{\hbar} E_{\nu_0} t_1} \zeta_{\nu_0} \quad (2.4.27)$$

For $t' = t_1$, in the excitation time, the wavefunction ϕ_{ν_0} is transferred on the excited state \hat{H}_f and propagates on it. While the ground vibrational state is an eigenvector of \hat{H}_i , it is not anymore of \hat{H}_f . Hence following the excitation, it evolves as coherent wavepacket (Eq. 2.4.23).

In a simple picture, two different scenarios are possible depending whether the potential is bounded or dissociative. In the first case, the wavepacket will first leave the FC region and then return after reaching the classical turning point for a complete (or partial) recurrence. In case of unbounded PES, the wavepacket will evolve towards the asymptotic region leaving the FC region.

The overlap between the wavepacket ψ and the wavefunction of the vibrational ground state ϕ_{ν_0} gives the correlation function

$$C(t) = \langle \phi_{\nu_0} | \psi^{(1)}(t) \rangle \quad (2.4.28)$$

The spectrum can be reached via the Fourier transform (FT) of the correlation function $C(t)$

$$\sigma(\omega) = \frac{4\pi^2\hbar^2\alpha}{m^2\omega_{fi}} \frac{1}{2\pi} \int_{-\infty}^{\infty} C(t)e^{i\omega t}e^{-\Gamma t}dt \quad (2.4.29)$$

where the term $e^{-\Gamma t}$ takes into account the de-excitation (Auger) phenomena. The correlation function $C(t)$ and the spectrum $\sigma(\omega)$ are Fourier transform pair.

2.4.4 Equivalence between the time dependent and independent approach

The expression of the spectra in the TI and TD regime are presented in Eq. 2.4.7 and Eq. 2.4.29, respectively and they are equivalent.

The wavepacket in the initial state is a wavefunction of this state (ϕ_{ν_0}) and it can be rewritten in terms of superposition of vibrational excited states

$$|\psi^{(1)}(t)\rangle = \mu_{fi} \sum_{\nu'} c_{\nu'} e^{-\frac{i}{\hbar}E_{\nu'}t} |\phi_{\nu'}\rangle \quad (2.4.30)$$

where the coefficients are defined as

$$c_{\nu'} = \langle \phi_{\nu'} | \phi_{\nu_0} \rangle \quad (2.4.31)$$

Eq. 2.4.31 means that we can express the initial wavefunction as projection on the excited state ν' .

Substituting Eq. 2.4.30 in the expression of the correlation function we got

$$C(t) = \langle \phi_{\nu_0} | \psi^{(1)}(t) \rangle = \mu_{fi} \sum_{\nu'} \langle \phi_{\nu'} | \phi_{\nu_0} \rangle e^{-\frac{i}{\hbar}E_{\nu'}t} \langle \phi_{\nu_0} | \phi_{\nu'} \rangle \quad (2.4.32)$$

Applying the FT of Eq. 2.4.32, the spectrum computed in the Condon approximation for

a system with m excited states is

$$\sigma(\omega) = \sum_m \frac{4\pi^2 \hbar^2 \alpha}{m_e^2 \omega_{mi}} \frac{1}{3} \mu_{mi}^2 \sum_{\nu'} \langle \phi_{\nu'_m} | \phi_{\nu_0} \rangle \langle \phi_{\nu_0} | \phi_{\nu'_m} \rangle \int e^{i(\omega - \frac{E_{\nu'_m}}{\hbar})t} e^{-i\Gamma t} dt \quad (2.4.33a)$$

$$= \sum_m \frac{4\pi^2 \hbar^2 \alpha}{m_e^2 \omega_{mi}} \frac{1}{3} \mu_{mi}^2 \sum_{\nu'} \langle \phi_{\nu'_m} | \phi_{\nu_0} \rangle \langle \phi_{\nu_0} | \phi_{\nu'_m} \rangle L(\omega - E_{\nu'_m}; \Gamma) \quad (2.4.33b)$$

$$= \sum_m \frac{4\pi^2 \hbar^2 \alpha}{m_e^2 \omega_{mi}} \frac{1}{3} \mu_{mi}^2 \sum_{\nu'} |\langle \phi_{\nu} | \phi_{\nu'_m} \rangle|^2 L(\omega - E_{\nu'_m}; \Gamma) \quad (2.4.33c)$$

where $L(\omega - E_{\nu'_m}; \Gamma)$ stands for the Lorentzian profile. In Eq. 2.4.30c, one recognizes the sum over the FC factors which is equivalent to Eq. 2.4.7.

3 | Electronic structure calculations

In this chapter are presented the quantum chemistry methods used to solve the TISE in our work. First, in Section 3.1 are described the properties that the electronic wavefunction must satisfy. After, in Section 3.2, the Hartree-Fock method is presented paying attention on the treatment to the resolution of the equations for both closed and open-shell systems, respectively in Section 3.2.1 and 3.2.2-3.2.3. In Section 3.3, following an introduction about the concept of the correlation energy, post Hartree-Fock methods (Configuration Interaction and Multi Configurational Self Consistent Field) are presented. The Chapter ends with an overview on the Density Functional Theory.

3.1 The wavefunction approximation and Slater determinant

The TISE can be solved analytically only for few one-electron systems, such as Hydrogen, Hydrogen-like atoms and diatomic H_2^+ molecular system. To solve it for multi-electron systems, it is necessary to introduce an approximate expression of the wavefunction. However, this expression must preserve some properties that are illustrated in the following [53].

For a fermionic system, having N particles, the simplest approximate wavefunction can be expressed as a *Slater determinant*

$$|\psi\rangle = |\chi_1\chi_2\cdots\chi_N| = \frac{1}{\sqrt{N!}} \begin{vmatrix} \chi_1(\mathbf{x}_1) & \chi_2(\mathbf{x}_1) & \cdots & \chi_N(\mathbf{x}_1) \\ \chi_1(\mathbf{x}_2) & \chi_2(\mathbf{x}_2) & \cdots & \chi_N(\mathbf{x}_2) \\ \vdots & \vdots & \ddots & \vdots \\ \chi_1(\mathbf{x}_N) & \chi_2(\mathbf{x}_N) & \cdots & \chi_N(\mathbf{x}_N) \end{vmatrix} \quad (3.1.1)$$

where $\frac{1}{\sqrt{N!}}$ is the normalization condition and $\chi_N(\mathbf{x})$ are *spin - orbitals*. The Slater determinant

ensures the condition of *antisymmetry* of the wavefunction and thus satisfies the *Pauli's principle* [53, 54].

A spin-orbital χ (Eq. 3.1.2) is given by the product of two function depending on spatial coordinates $\tilde{\varphi}(\mathbf{r})$ and spin $\sigma(\varpi)$, the last one describes the spin of the electron and α and β stand for spin *up* and *down*, respectively.

$$\chi(\mathbf{r}) = \begin{cases} \tilde{\varphi}(\mathbf{r}) \alpha \\ \tilde{\varphi}(\mathbf{r}) \beta \end{cases} \quad (3.1.2)$$

As well as the exact wavefunction, $\{\psi\}$ has to be antisymmetric respect to the permutation operation, *square integrable* and hence *normalized* (Eq. 3.1.3) and eigenfunction of the total and projected spin operators (Eq. 3.1.4a).

$$\langle \psi | \psi \rangle = 1 \quad (3.1.3)$$

$$S^2 \psi = S(S+1) \psi \quad (3.1.4a)$$

$$S_z \psi = M_S \psi \quad (3.1.4b)$$

3.2 The Hartree-Fock method

The Hartree - Fock (HF) equation transforms the *many-electron* problem into N *one-electron* problems. Its resolution depends on the spin orbitals of the others electrons thus the Fock operator depends on from its solutions and it must be solved iteratively using the Self Consistent Field (SCF) method ¹ [54]. The solution of the HF equations leads to a set of spin-orbitals $\{\chi_k\}$ with energies $\{\epsilon_k\}$.

The Hartree-Fock equation

As previously introduced, the HF theory is a one-determinant theory. In order to solve the HF equations we have to find the set of spin-orbitals $\{\chi_a\}$ which represent the best approximation

¹In the SCF method, a set of orbitals is used as initial guess to solve the HF equation and compute the average field for each electron. The new set of spin orbitals is then used to solve again the equation. The operation is repeated until the self-consistency is obtained.

of the ground state N-electrons system. Within the variational principle, the best spin-orbitals are the ones which minimize the electronic energy

$$E^{HF} = \langle \Psi | \hat{H} | \Psi \rangle \quad (3.2.1a)$$

$$= \sum_a \langle a | h | a \rangle + \frac{1}{2} \sum_{ab} \langle ab || ab \rangle \quad (3.2.1b)$$

where a and b are the spin-orbitals. In Eq. 3.2.1b, the first term is the one-electron integral and the second term is the compact form of the two-electrons integrals. This last is defined as follow

$$\langle ab || ab \rangle = \langle ab | ab \rangle - \langle ab | ba \rangle \quad (3.2.2a)$$

$$= \int d\mathbf{r}_i \int d\mathbf{r}_j \chi_a^*(i) \chi_b^*(j) \frac{1}{r_{ij}} \chi_b(j) \chi_a(i) - \int d\mathbf{r}_i \int d\mathbf{r}_j \chi_a^*(i) \chi_b^*(j) \frac{1}{r_{ij}} \chi_a(j) \chi_b(i) \quad (3.2.2b)$$

where the two integrals are called *Coulomb* and *Exchange integral*, respectively.

The HF equation can be rewritten in terms of the following eigenvalue equation

$$h(i)\chi_a(i) + \sum_{b \neq a} \left[\int d\mathbf{r}_j \chi_b^*(j) \frac{1}{r_{ij}} \chi_b(j) \right] \chi_a(i) - \sum_{b \neq a} \left[\int d\mathbf{r}_j \chi_b^*(j) \frac{1}{r_{ij}} \chi_a(j) \right] \chi_b(i) = \epsilon_a \chi_a(i) \quad (3.2.3)$$

where the three operators are called *Hartree* $h(i)$, *Coulomb* $\mathcal{J}_b(i)$ and *exchange operator* $\mathcal{K}_b(i)$, respectively.

The Coulomb operator is a *local operator* representing the instantaneous interaction between the electron i and j through the *two-electrons* potential r_{ij}^{-1} . It describes the average local potential on χ_a at the position $d\mathbf{r}_i$ arising from the electron that occupies the spin orbital χ_b . The exchange operator is a *non-local operator* arising from the antisymmetric nature of the wavefunction and it involves the exchange between the electrons i and j . It is defined non-local because it is not possible to define a unique potential $\mathcal{K}_b(\mathbf{r}_i)$ at a local point in the space \mathbf{r}_i . The result of $\mathcal{K}_b(i)\chi_a(i)$ depends on the $\chi_a(i)$ values throughout the entire space.

Solving the Hartree-Fock equation

The HF method is variational and its solution leads to a set of orthonormal orbitals such that minimize the energy, this process is carried out using the *Lagrange's method*.

The total energy of a system E_0 is a functional of the spin orbitals $\{\chi_a\}$ and it is necessary to minimize it with respect to the spin orbitals. Furthermore, we want to keep the orbitals orthogonal to each other

$$\int d\mathbf{r}_i \chi_a^*(i) \chi_b(i) = \delta_{ab} \Rightarrow \int d\mathbf{r}_i \chi_a^*(i) \chi_b(i) - \delta_{ab} = 0 \quad (3.2.4)$$

where the overlap integral can be rewritten in a more compact form as S_{ab}

The Lagrange's function can be written as

$$\mathcal{L}[\{\chi_a\}] = E_0[\{\chi_a\}] - \sum_{a=1}^N \sum_{b=1}^N \epsilon_{ba} (S_{ab} - \delta_{ab}) \quad (3.2.5)$$

where E_0 is the expectation value for the single determinant wavefunction and ϵ_{ba} are the Lagrange multipliers.

Applying an infinitesimal variation such that $\chi_a \rightarrow \chi_a + \delta\chi_a$, the first variation of the Lagrange's function is

$$\delta\mathcal{L} = \delta E_0 - \sum_{a=1}^N \sum_{b=1}^N \epsilon_{ba} \delta S_{ab} \quad (3.2.6)$$

where

$$\delta S_{ab} = \int d\mathbf{x}_i \delta\chi_a^*(i) \chi_b(i) + \int d\mathbf{x}_i \chi_a^*(i) \delta\chi_b(i) \quad (3.2.7)$$

and the first variation in E_0 is

$$\delta E_0 = \sum_{a=1}^N \delta h_{aa} + \frac{1}{2} \sum_{a=1}^N \sum_{b=1}^N \left(\delta \mathcal{J}_{ab} - \delta \mathcal{K}_{ab} \right) \quad (3.2.8)$$

which is the sum of the first variation of the Hartree, Coulomb and exchange operators having

the following form

$$\delta h = \int d\mathbf{x}_i \delta \chi_a^*(i) h(i) \chi_a(i) + \int d\mathbf{x}_i \chi_a^*(i) h(i) \delta \chi_a(i) \quad (3.2.9a)$$

$$\begin{aligned} \delta \mathcal{J}_{ab} = & \int \int d\mathbf{x}_i \mathbf{x}_j \delta \chi_a^*(i) \chi_a(i) \frac{1}{r_{ij}} \chi_b^*(j) \chi_b(j) + \int \int d\mathbf{x}_i \mathbf{x}_j \chi_a^*(i) \delta \chi_a(i) \frac{1}{r_{ij}} \chi_b^*(j) \chi_b(j) \\ & + \int \int d\mathbf{x}_i \mathbf{x}_j \chi_a^*(i) \chi_a(i) \frac{1}{r_{ij}} \delta \chi_b^*(j) \chi_b(j) + \int \int d\mathbf{x}_i \mathbf{x}_j \chi_a^*(i) \chi_a(i) \frac{1}{r_{ij}} \chi_b^*(j) \delta \chi_b(j) \end{aligned} \quad (3.2.9b)$$

$$\begin{aligned} \delta \mathcal{K}_{ab} = & \int \int d\mathbf{x}_i \mathbf{x}_j \delta \chi_a^*(i) \chi_b(i) \frac{1}{r_{ij}} \chi_b^*(j) \chi_a(j) + \int \int d\mathbf{x}_i \mathbf{x}_j \chi_a^*(i) \delta \chi_b(i) \frac{1}{r_{ij}} \chi_b^*(j) \chi_a(j) \\ & + \int \int d\mathbf{x}_i \mathbf{x}_j \chi_a^*(i) \chi_b(i) \frac{1}{r_{ij}} \delta \chi_b^*(j) \chi_a(j) + \int \int d\mathbf{x}_i \mathbf{x}_j \chi_a^*(i) \chi_b(i) \frac{1}{r_{ij}} \chi_b^*(j) \delta \chi_a(j) \end{aligned} \quad (3.2.9c)$$

Substituting the Eq. 3.2.9a - 3.2.9c in Eq. 3.2.8 and then in Eq. 3.2.6 we obtain

$$\delta \mathcal{L} = \sum_{a=1}^N \int d\mathbf{x}_i \delta \chi_a^*(i) \left[h(i) \chi_a(i) + \sum_{b=1}^N (\mathcal{J}_b(i) - \mathcal{K}_b(i)) \chi_a(i) - \sum_{b=1}^N \epsilon_{ba} \chi_b(i) \right] + \text{complex conjugate} = 0 \quad (3.2.10)$$

In order that Eq. 3.2.10 is satisfied, the quantity in square bracket must be zero then we obtain

$$\left[h(i) + \sum_{b=1}^N (\mathcal{J}_b(i) - \mathcal{K}_b(i)) \right] \chi_a(i) = \sum_{b=1}^N \epsilon_{ba} \chi_b(i) \quad (3.2.11)$$

Eq. 3.2.11 is the Fock equation and it can be rewritten in a more compact form as

$$f |\chi_a\rangle = \sum_{b=1}^N \epsilon_{ba} \chi_b(i) \quad (3.2.12)$$

where f is the *Fock operator*.

The Eq. 3.2.12 does not have the canonical form of the eigenvalue equation and its form arises from the single determinant nature of the wavefunction then the expectation value of the energy does not change when the spin-orbitals are mixed. To obtain an eigenvalue equation as that seen previously, it is necessary to operate an unitary transformation to the spin orbitals such that

$$\chi'_a = \sum_b \chi_b U_{ba} \quad (3.2.13)$$

hence it must exist a spin orbitals set $\{\chi'_a\}$ such that the Lagrange multipliers matrix is diagonal

$$f(i)|\chi'_a\rangle = \epsilon'_a|\chi'_a\rangle \quad (3.2.14)$$

The set of spin orbital $\{\chi'_a\}$ reached from the eigenvalue equation are called *canonical spin orbitals* and the prime can be dropped. Eq. 3.2.14 says that ϵ_a is the energy associated to the spin orbital $|\chi_a\rangle$. For a general N-electronic system, the $N/2$ spin orbitals with the lower energy are called *occupied* while the rest are called *unoccupied* or *virtual*. The first ones are labelled as a, b, c, \dots and the other as r, s, t, \dots

The Fock equation can be rewritten using the *bra-ket* notation

$$\langle \chi_b | f | \chi_a \rangle = \epsilon_a \langle \chi_b | \chi_a \rangle = \epsilon_a \delta_{ab} \quad (3.2.15)$$

then

$$\epsilon_a = \langle \chi_a | f | \chi_a \rangle \quad (3.2.16a)$$

$$= \langle \chi_a | f + \sum_b (\mathcal{J}_b - \mathcal{K}_b) | \chi_a \rangle \quad (3.2.16b)$$

$$= \langle a | h | a \rangle + \sum_{b \neq a} \langle ab | ab \rangle - \langle ab | ba \rangle \quad (3.2.16c)$$

where the Coulomb and exchange integrals are written in the more compact form previously presented. The exchange integral is non zero only for spin orbital with parallel spin.

In a similar way, it is possible to define the energy for the virtual orbitals as

$$\epsilon_r = \langle r | h | r \rangle + \sum_b \langle rb | rb \rangle - \langle rb | br \rangle \quad (3.2.17)$$

The resolution of the HF equation depends on whether the system is closed or open-shell as illustrated in the following section.

3.2.1 Application of the Hartree Fock method

3.2.1.1 The Restricted Hartree-Fock method

For a molecular closed-shell system, the Fock equation can be solved with a standard matrix technique, this method was first introduced by Roothaan [55]. For this purpose the spin orbitals are replaced by a *Linear Combination of Atomic Orbitals (LCAO)*

$$\chi_a = \sum_{g=1} C_{ga} \phi_g \quad \begin{array}{l} a = 1, 2, 3, \dots, K \\ g = \mu, \nu, \sigma, \dots \end{array} \quad (3.2.18)$$

where g is a general indice for the basis function. Notice that here ϕ is used to indicate the atomic orbitals. Inserting Eq. 3.2.18 in the general Hartree-Fock equation we obtain

$$f(i) \sum_{\nu} C_{\nu a} \phi_{\nu}(i) = \epsilon_a \sum_{\nu} C_{\nu a} \phi_{\nu}(i) \quad (3.2.19)$$

multiplying this equation by the conjugate complex $\phi_{\mu}^*(i)$ and integrating over the coordinates of the i^{th} electron it follows that

$$\sum_{\nu} C_{\nu a} \int d\mathbf{r}_i \phi_{\mu}^*(i) f(i) \phi_{\nu}(i) = \epsilon_a \sum_{\nu} C_{\nu a} \int d\mathbf{r}_i \phi_{\mu}^*(i) \phi_{\nu}(i) \quad (3.2.20)$$

Eq. 3.2.20 permits to define the *overlap* and *Fock matrices* respectively in Eq. 3.2.21 and 3.2.22

$$S_{\mu\nu} = \int d\mathbf{r}_i \phi_{\mu}^*(i) \phi_{\nu}(i) \quad (3.2.21)$$

$$F_{\mu\nu} = \int d\mathbf{r}_i \phi_{\mu}^*(i) f(i) \phi_{\nu}(i) \quad (3.2.22a)$$

$$= \int d\mathbf{r}_i \phi_{\mu}^* h(i) \phi_{\nu}(i) + \sum_{a=1}^{N/2} \int d\mathbf{r}_i \phi_{\mu}^* \left[2\mathcal{J}_a(i) - \mathcal{K}_a(i) \right] \phi_{\nu}(i) \quad (3.2.22b)$$

that lead to the *Roothaan's equation* in the matrix form

$$\mathbf{FC} = \mathbf{SC}\epsilon \quad (3.2.23)$$

where \mathbf{C} is the coefficient matrix and ϵ is the diagonal matrix containing the energy ϵ_a associated to the molecular orbitals ψ_a . Once obtained the molecular orbitals, it is possible to compute the *probability density* distribution for a closed-shell system

$$\rho(\mathbf{r}) = 2 \sum_a^{N/2} |\chi_a(\mathbf{r})|^2 \quad (3.2.24)$$

where $N/2$ is the number of occupied MOs and the factor 2 is the number of electrons by MOs. Eq. 3.2.24 describes that probability to find one electron in the volume element $d\mathbf{r}$. It can be rewritten in term of *density matrix* $P_{\mu\nu}$ using the molecular orbital expression seen in Eq. 3.2.18

$$\rho(\mathbf{r}) = 2 \sum_a^{N/2} \sum_\nu C_{\nu a}^* \phi_\nu^*(\mathbf{r}) \sum_\mu C_{\mu a} \phi_\mu(\mathbf{r}) \quad (3.2.25a)$$

$$= \sum_{\mu\nu} P_{\mu\nu} \phi_\mu(\mathbf{r}) \phi_\nu^*(\mathbf{r}) \quad (3.2.25b)$$

where $P_{\mu\nu}$ is

$$P_{\mu\nu} = 2 \sum_a^{N/2} C_{\mu a} C_{\nu a}^* \quad (3.2.26)$$

We can express Eq. 3.2.22 in function of the density matrix on the atomic orbital representation and rewrite it as

$$F_{\mu\nu} = H_{\mu\nu} + P_{\mu\nu} \sum_{\lambda\sigma} \left[(\mu\nu|\sigma\lambda) - \frac{1}{2}(\mu\lambda|\sigma\nu) \right] \quad (3.2.27)$$

where the last two integrals represent the two-electron part of the Fock matrix

In order to solve the Eq. 3.2.23 into a form of usual eigenvalue problem we need to work with orbitals that are orthonormal. It is necessary carry out a orthonormalization procedure on the orbitals reached by solving the Roothaan's equations. The set of orbitals not orthogonal $\{\phi_\mu\}$ gives a overlap matrix \mathbf{S} (Eq. 3.2.21) and it is possible to define a new set of orbitals $\{\phi'_\mu\}$

$$\phi'_\mu = \sum_\nu X_{\nu\mu} \phi_\nu \quad (3.2.28)$$

that gives

$$\int d\mathbf{r} \phi_{\mu}^*(\mathbf{r}) \phi_{\nu}'(\mathbf{r}) = \delta_{\mu\nu} \quad (3.2.29)$$

To carry out normalization, we can define a transformation matrix

$$\mathbf{X} = \mathbf{U} \mathbf{S}^{1/2} \quad (3.2.30)$$

such that it permits to eliminate the overlap matrix in the Roothaan's equation and gives new normalized coefficients matrix \mathbf{C}

$$\mathbf{X}^{\dagger} \mathbf{S} \mathbf{X} = \mathbf{1}; \quad \mathbf{C} = \mathbf{X} \mathbf{C}' \quad (3.2.31)$$

Substituting Eq. 3.2.30 and 3.2.31 in the Roothaan's equation (Eq. 3.2.23), we obtain

$$\mathbf{F}' \mathbf{C}' = \mathbf{C}' \epsilon \quad (3.2.32)$$

which is called *transformed Roothaan's equations*. Solving Eq. 3.2.32, from the diagonalization of \mathbf{F}' we obtain the coefficient \mathbf{C}' . Through this last one, we can solve the Roothaan's equation.

The Roothaan's equations are solved iteratively using the SCF procedure depicted in Fig. 3.1. The procedure is ended when the energy and density convergence is reached.

3.2.1.2 The Unrestricted Hartree Fock method

For open shell systems, the simple way is to introduce in the spin orbitals the dependence of the spatial part on the spin. It follows that we can define two sets of LCAO χ_a^{α} and χ_a^{β} with general form

$$\chi_a^{\varrho} = \sum_{\mu=1}^K C_{\mu a} \phi_{\mu}(\mathbf{r}) \varrho \quad \varrho = \alpha, \beta \quad (3.2.33)$$

and the Fock equations become

$$f(i) \chi_a^{\varrho}(\mathbf{r}_i) \varrho = \epsilon_a^{\varrho} \chi_a^{\varrho}(\mathbf{r}_i) \varrho \quad (3.2.34)$$

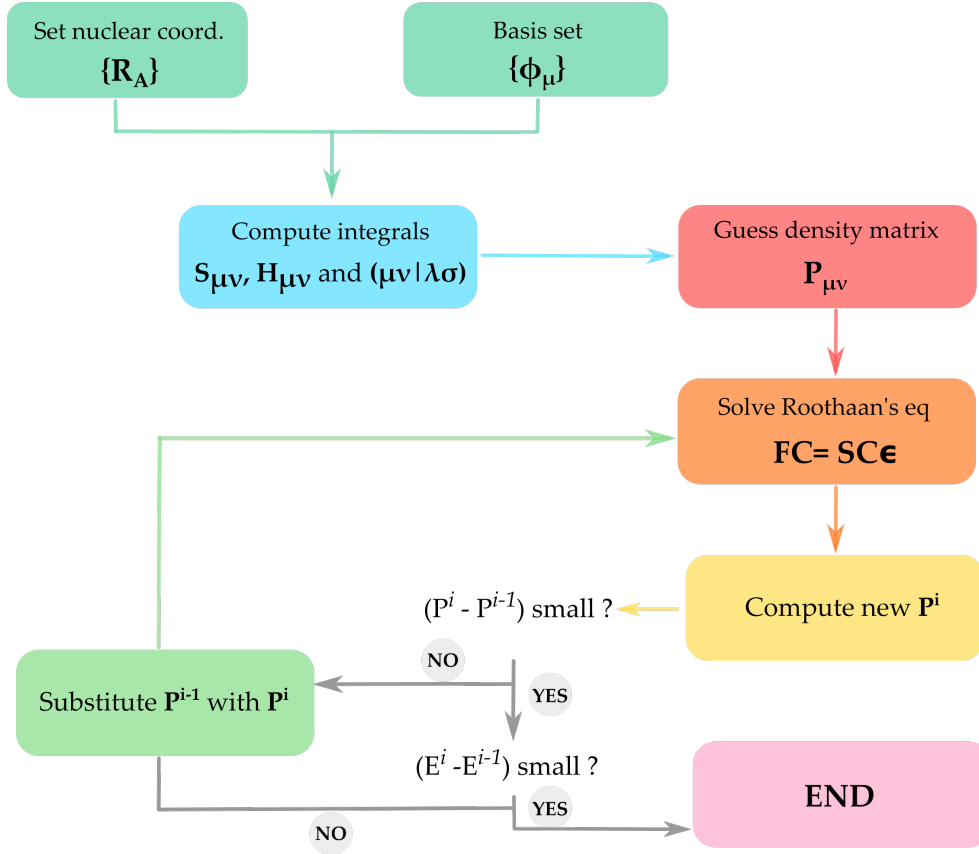


Figure 3.1: Scheme of the Self Consistent Field (SCF) procedure used to solve the Hartree-Fock equation.

where ϵ_a^ρ is the energy of the spin orbital $\psi_a^\rho(\mathbf{r}_i)\rho$ with $\rho = \alpha, \beta$. Multiplying for $\rho^*(\varpi_i)$ and integrating over the spin, we obtain two different Fock operators for the spin α and β

$$f^\alpha(i)\chi_a^\alpha(i) = \epsilon_a^\alpha \chi_a^\alpha(i) \quad (3.2.35a)$$

$$f^\beta(i)\chi_a^\beta(i) = \epsilon_a^\beta \chi_a^\beta(i) \quad (3.2.35b)$$

corresponding to the following matrix form

$$\mathbf{F}^\alpha \mathbf{C}^\alpha = \mathbf{S} \mathbf{C}^\alpha \epsilon^\alpha \quad (3.2.36a)$$

$$\mathbf{F}^\beta \mathbf{C}^\beta = \mathbf{S} \mathbf{C}^\beta \epsilon^\beta \quad (3.2.36b)$$

called *Pople-Nesbet equations* [56]. As well as for the RHF, it is necessary to compute the density matrix associated to the basis, in this case the *total density matrix* $P_{\mu\nu}^T$ depends on the two density matrices $P^\alpha(\mathbf{r})$ and $P^\beta(\mathbf{r})$

$$P_{\mu\nu}^\alpha = \sum_a^{N_\alpha} C_{\mu a}^\alpha (C_{\nu a}^\alpha)^* \quad (3.2.37a)$$

$$P_{\mu\nu}^\beta = \sum_a^{N_\beta} C_{\mu a}^\beta (C_{\nu a}^\beta)^* \quad (3.2.37b)$$

$$P_{\mu\nu}^T = P_{\mu\nu}^\alpha + P_{\mu\nu}^\beta \quad (3.2.37c)$$

and it follows that the expression of the $P_{\mu\nu}^T$ appears in both expression of the Fock operator

$$F_{\mu\nu}^\alpha = H_{\mu\nu}^\alpha + \sum_\lambda \sum_\sigma P_{\lambda\sigma}^T (\mu\nu|\sigma\lambda) - P_{\lambda\sigma}^\alpha (\mu\lambda|\sigma\nu) \quad (3.2.38a)$$

$$F_{\mu\nu}^\beta = H_{\mu\nu}^\beta + \sum_\lambda \sum_\sigma P_{\lambda\sigma}^T (\mu\nu|\sigma\lambda) - P_{\lambda\sigma}^\beta (\mu\lambda|\sigma\nu) \quad (3.2.38b)$$

and the two equations must be solved simultaneously.

The problem with the Unrestricted Hartree-Fock (UHF) method is that the wavefunction is not an eigenfunction of S^2 (so-called *spin contamination*). For this reason the UHF wavefunction does not represent a good guess for the calculation of correlated systems or excited states and the Restricted Open shell Hartree-Fock (ROHF) is preferable.

3.2.1.3 The Restricted Open-shell Hartree Fock method

The problem of spin contamination, seen previously, may be solved by defining an unique Fock matrix [57, 58]

$$F_{\mu\nu} = \sum_\nu a_\nu H_{\mu\nu} + \sum_{\mu\nu} a_\nu a_\mu (2b_\mu^\nu \langle \mu\nu | \mu\nu \rangle - c_\mu^\nu \langle \mu\nu | \nu\mu \rangle) \quad (3.2.39)$$

where b_μ^ν and c_μ^ν are the coupling coefficients and a_ν and a_μ are the orbitals occupancy. These can have different values of 1, 1/2 and 0 whether the orbital is doubly occupied (*c*), singly occupied (*o*) and virtual orbitals (*v*) respectively. The Roothaan's effective Fock operator is then defined in the MOs basis and it has the following form

$$\mathbf{F} = \begin{pmatrix} \mathbf{P}_{cc} & \mathbf{F}_{co}^{\beta} & \mathbf{F}_{cv}^{cs} \\ \mathbf{F}_{oc}^{\beta} & \mathbf{P}_{oo} & \mathbf{F}_{ov}^{\alpha} \\ \mathbf{F}_{vc}^{cs} & \mathbf{F}_{vo}^{\alpha} & \mathbf{P}_{vv} \end{pmatrix} \quad (3.2.40)$$

where \mathbf{F}^{α} and \mathbf{F}^{β} are the UHF Fock matrices and $\mathbf{F}^{cs} = (\mathbf{F}^{\alpha} + \mathbf{F}^{\beta})/2$. The diagonal terms \mathbf{P} are the density matrix chosen arbitrarily for a set of A and B parameters

$$\mathbf{P}_{cc} = A_{cc}\mathbf{F}_{cc}^{\alpha} + B_{cc}\mathbf{F}_{cc}^{\beta} \quad (3.2.41a)$$

$$\mathbf{P}_{oo} = A_{oo}\mathbf{F}_{oo}^{\alpha} + B_{oo}\mathbf{F}_{oo}^{\beta} \quad (3.2.41b)$$

$$\mathbf{P}_{vv} = A_{vv}\mathbf{F}_{vv}^{\alpha} + B_{vv}\mathbf{F}_{vv}^{\beta} \quad (3.2.41c)$$

different values of A and B have been proposed in different works [57]. After a basis transformation, the matrix in Eq. 3.2.40 is solved within the same procedure presented for the RHF method. The ROHF wavefunction does not suffer of spin contamination.

3.3 The post Hartree-Fock methods

The lack of correlation of the HF method brings to the definition of correlation energy as the difference between the exact non-relativistic energy \mathcal{E} and the energy at the HF limit E^{HF}

$$E_{corr} = \mathcal{E} - E^{HF} \quad (3.3.1)$$

The limits of the HF method are reflected also in the bond description in particular regions of the PES or for systems to whom the one-determinant wavefunction does not provides a good description. To go beyond the HF limit and recover the correlation it is necessary to turn to methods that use a multiconfigurational wavefunction as the Configuration Interaction (CI) or the Multi Configurational Self Consistent Field (MCSCF). To this purpose, these methods are presented below.

3.3.1 Configuration Interaction method

In the CI method, the wave function is expressed as a linear combination of Slater determinants where the determinants are expressed according to the number of "excitations". Considering

ψ_0 , the HF determinant, as a good approximation of the wavefunction, we can write a linear combination of new determinants as follow

$$|\Psi^{CI}\rangle = \sum_i C_i |\psi_i\rangle \quad (3.3.2a)$$

$$= c_0 |\psi_0\rangle + \sum_{ar} c_a^r |\psi_a^r\rangle + \sum_{\substack{a<b \\ r<s}} c_{ab}^{rs} |\psi_{ab}^{rs}\rangle + \sum_{\substack{a<b<c \\ r<s<t}} c_{abc}^{rst} |\psi_{abc}^{rst}\rangle + \dots \quad (3.3.2b)$$

where the determinant $|\psi_a^r\rangle$ is obtained by exciting one electron in $|\psi_0\rangle$ from the occupied orbital a to the virtual r , in the same way the determinant $|\psi_{ab}^{rs}\rangle$ is obtained by exciting two electrons from the occupied orbitals a and b to the virtual orbital r and s and so on. These terms are called “*configuration*” while the Configuration State Functions (CSF) are linear combinations of Slater’s determinants that are also eigenfunctions of the spin angular momentum operator \hat{S}^2 .

The coefficients in Eq. 3.3.2 are determined by variational procedure intended to minimize the expectation value of the energy for the eigenvalue equation

$$\mathbf{H}\mathbf{C} = E_{CI}\mathbf{C} \quad (3.3.3)$$

where \mathbf{C} is the vector containing the coefficient values obtained by diagonalizing the Hamiltonian matrix \mathbf{H} . Using the CI method, the optimization is performed only on the coefficient in Eq. 3.3.2 and not on the orbitals. The solving procedure is called “*full CI*” (FCI) when all possible CSF are used.

The structure of the Hamiltonian matrix has the following form

$$\mathbf{H} = \begin{matrix} \langle\psi_0| \\ \langle\psi_a^r| \\ \langle\psi_{ab}^{rs}| \\ \langle\psi_{abc}^{rst}| \\ \langle\psi_{abcd}^{rstq}| \\ \vdots \end{matrix} \left[\begin{array}{cccccc} \langle\psi_0|H|\psi_0\rangle & & & & & \\ 0 & \langle\psi_a^r|H|\psi_a^r\rangle & & & & \\ \langle\psi_{ab}^{rs}|H|\psi_0\rangle & \langle\psi_{ab}^{rs}|H|\psi_a^r\rangle & \langle\psi_{ab}^{rs}|H|\psi_{ab}^{rs}\rangle & & & \\ 0 & \langle\psi_{abc}^{rst}|H|\psi_a^r\rangle & \langle\psi_{abc}^{rst}|H|\psi_{ab}^{rs}\rangle & \langle\psi_{abc}^{rst}|H|\psi_{abc}^{rst}\rangle & \dots & \\ 0 & 0 & \langle\psi_{abcd}^{rstq}|H|\psi_{ab}^{rs}\rangle & \langle\psi_{abcd}^{rstq}|H|\psi_{abc}^{rst}\rangle & \langle\psi_{abcd}^{rstq}|H|\psi_{abcd}^{rstq}\rangle & \\ \vdots & \vdots & \vdots & \vdots & \vdots & \vdots \end{array} \right] \quad (3.3.4)$$

where the elements $\langle\psi_0|H|\psi_a^r\rangle$ are zero as consequence of the *Brillouin’s theorem* and the other zero-value matrix elements came from the fact that matrix elements between two determinants

differing by more than two excitations are zero. As consequence of the Brillouin's theorem, the reference energy is not affected by the single excited determinant directly and the coupling between reference and single excitation is indirect. On the contrary doubly excitation CSFs couple directly with the reference [54].

Performing a FCI calculation is unworkable for most of the system of interest because the size of the CI matrix depends on the number of CSF. For a system with N electrons and M orbitals the number of possible CSF is

$$N_{CSF} = \binom{M}{N} = \frac{M!}{N!(M-N)!} \quad (3.3.5)$$

It follows that the size of the CI matrix scales factorially with the number of electrons and the orbitals [59]. It is thus necessary to truncate the expansion. The method is named Configuration Interaction Singles (CIS), Configuration Interaction Singles Doubles (CISD) or Configuration Interaction Singles Doubles Triples (CISDT) if the truncation is operated on the first, second or third excited terms of Eq. 3.3.2b, respectively.

In order to make CI calculations more affordable, the *frozen core approximation* was introduced [60, 61, 62]. Within this approximation the lowest lying molecular orbitals are forced to be doubly occupied in all CSF hence it permits to reduce considerably the size of the CI matrix.

The inclusion of more excitation is not workable for large systems making the CIS the only CI method usable. In order to improve the results, it is possible to make the wavefunction more flexible using extended basis set and allowing the mixing of CSF corresponding to different excitations ???. This makes the energies obtained within truncated CI sensitive to the set of used guess orbital.

Configuration Interaction for the excited state calculations

The CI method can be used to compute the energies of the excited states of a system and for extended systems with large basis the most convenient is use CIS method [63]

$$|\Psi^{CIS}\rangle = \sum_{ar} C_a^r |\psi_a^r\rangle \quad (3.3.6)$$

The CI coefficient in Eq. 3.3.6 are computed through the matrix elements [54]

$$\langle \psi_a^r | H | \psi_b^s \rangle = [E_{HF} + \epsilon_r - \epsilon_a] \delta_{rs} \delta_{ab} - (rs|ba) + 2(ra|bs) \quad (3.3.7)$$

where ϵ_a and ϵ_r are the energy for the molecular orbitals a and r and $(ra||sb)$ are the two electrons integral in the MO basis. The eigenvalue E_{CIS} is the total energy of the chosen excited state.

The wavefunction and the energies obtained can be used to compute different properties among which the dipole moment transition

$$\mu_{LM} = e \langle \psi_L^{CIS} | \sum_i \mathbf{r}_i | \psi_M^{CIS} \rangle \quad (3.3.8)$$

where L and M generally indicate two states.

3.3.2 Multi Configurational self-consistent field method

In order to have a good description of the dissociation limit it is necessary to go to *multiconfigurational methods* presented in the next section. The MCSCF method is a flexible method that can be used for the study of systems both in ground and excited states. Unlike what we have seen so far, the wavefunction is written as

$$|\psi^{MCSCF}\rangle = e^{-\hat{\kappa}} \sum_i C_i |\psi_i\rangle \quad (3.3.9)$$

where $e^{-\hat{\kappa}}$ is the operator that carries out an unitary transformation between the MOs and C_i are the coefficients of the expansion. The MCSCF method is variational and throughout the minimization procedure both κ and \mathbf{C} are modified. As a consequence, the MCSCF method optimizes the coefficient and the molecular orbitals of the system. The MCSCF method coincides with the HF method if only one determinant is used.

The configurations of the MCSCF are selected using an occupancy 0 (*not occupied*), 1 (*singly occupied*) or 2 (*doubly occupied*) within the selected space. We can distinguish three different spaces: *inactive*, *active* and *secondary* (or *virtual*) orbitals. The active and inactive orbitals are respectively doubly occupied and unoccupied in all possible configurations. If all possible configurations of the orbitals in the active space are scanned, this method is called *complete active space SCF method*

A special case of the MCSCF method is the Generalized Valence Bond (GVB) approach. In this method, two orbital are used to describe each pair of electrons using a wavefunction

expressed as Slater's determinant. As all the method presented up to now, also the GVB is a variational method.

The GVB wavefunction is written in terms of composite wavefunction in terms of doubly and singly occupied MOs and orbitals in pair [64, 65]. The procedure to solve the GVB is more complicated than the others presented before and an extensive description can be found in the paper of *Langlois et al.* [66].

The GVB is able to treat properly the dissociation of a molecular system in its open-shell fragments.

3.4 Density Functional Theory

In the methods presented up to now the energy of a system is computed as expectation values of the wavefunction. In the Density Functional Theory (DFT) the energy is expressed as a *functional* of the electronic ground state density as defined from the *first theorem of Hohenberg-Kohn* [67]. The energy E^{DFT} of a N -electrons system is a unique functional of the electronic density of the ground state

$$E^{DFT}[\rho] = \int \rho(\mathbf{r})V_{Ne}d\mathbf{r} + F_{HK}[\rho] \quad (3.4.1)$$

where V_{Ne} is the attraction potential between the nuclei and the electrons and $F_{HK}[\rho]$ is the *Hohenberg-Kohn functional* defined as

$$F_{HK}[\rho] = T[\rho] + J[\rho] + E_{n-cl}[\rho] \quad (3.4.2)$$

where $T[\rho]$ is the kinetic energy functional, $J[\rho]$ is the Coulomb functional and $E_{non-cl}[\rho]$ is the energy functional describing the non classical electron-electron interaction. If the density is exact and the form of the Eq. 3.4.2 is known, the DFT provides the exact energy for the ground state. Unfortunately the exact form of $F_{HK}[\rho]$ is unknown then the computed energy strictly depends on the chosen functional.

To compute the DFT energy, it is necessary to use the *Kohn-Sham equations* as follow

$$f^{KS}\phi_a = \epsilon_a\phi_a \quad (3.4.3)$$

where ϕ_i are the *Kohn-Sham spin-orbitals* related to the electronic density of the system and f^{KS} is the *monoelectronic Kohn-Sham operator*, the two are defined as follow

$$\rho(\mathbf{r}) = \sum_a^N |\phi_a(\mathbf{r})|^2 \quad (3.4.4)$$

$$f^{KS} = -\frac{1}{2}\nabla^2 + \int \frac{\rho(r_j)}{r_{ij}} - \sum_J \frac{Z_J}{r_{iJ}} + V_{XC}(r_i) \quad (3.4.5)$$

where V_{XC} is the *exchange-correlation operator*. The KS equations are solved using the Lagrange method presented before.

Different approximations of the exchange-correlation operator have been proposed: *local density LDA*, *local spin density LSDA*, *generalized gradient GGA* approximation and *hybrid functional*. Development of more accurate functionals is still on going.

4 Computational protocols

In this Chapter we report the key aspects of the development of the protocols to the calculations of core excited spectra. The main goal is to provide a set of methods which can be applied both to the K- and L-shell excitation through the methods presented in the previous chapters.

States corresponding to the aforementioned absorption thresholds have significantly different characteristics. In particular, L-shell excited states exhibit strong spin-orbit couplings. For this reason, it is necessary to propose two different protocols.

In the first Section is presented the development of the protocol for the 1s excited systems. The CH^+ molecular ions was used as case study throughout the choice of the basis set, the set of spin orbitals and the method to take into account the dynamics in the excited states (time independent or time dependent).

In the second Section, the techniques used to compute the 2p core excited spectra are presented. We study the importance of the number of active electrons and the spin-orbit coupling operators used in the calculations of the core-excited state. In the second part of the section, the spin orbit coupling interaction was included explicitly in the calculations of the 2p ionization potential through the use of an effective Hamiltonian.

The Chapter ends with the computational details used in our calculations.

4.1 K-shell protocol

The carbon K-shell excitation spectra have been studied for the last three decades both on gas [68, 69, 70] and condensed phases [71]. The simulation of the spectra throughout quantum chemistry techniques invoke the use of different methods such as the DFT [72, 73] as well as

post-HF methods such as Coupled Cluster (CC) [74, 75] and Symmetry Adapted Cluter (SAC) - CI [76].

The CI method was successfully used for the simulation of resonant inelastic X-ray scattering (RIXS) and photoelectron spectra on the K-shell of chlorine [77]. In this work we want to develop a CI based method to the calculations of the photoabsorption spectra at the K-edge of light elements (C, N, O, etc.). The different aspects evaluated are reported in the following.

4.1.1 Development of the protocol

A general scheme of the protocol is presented in Fig. 4.1. In our calculations we want to account for relaxation effects upon the hole creation in order to achieve the best set of spin-orbitals to use in the PESs calculations. The PESs and dipole moments are then used as input for the nuclear dynamics simulations.

In the following subsections the aspects of each step of the calculations are reported separately.

Geometry optimization and ionization potential

The first step of the calculations is to obtain the equilibrium geometry of the systems both on the ground and metastable states. In the field of the molecular ions, the geometry data are not always available. We used the DFT method to find the equilibrium geometry of the systems considered in this work since it provides a good method for the geometry optimization [78, 79]. Nevertheless, when available, the computed data were compared to the experimental ones. Since the molecular ions are produced in a ECRIS source, it is important to compute the energy difference between the ground and valence excited states. We have evaluated it at the equilibrium geometry and at the same level of theory. Furthermore, the K-shell IP must be determined in order to set the upper limit of the X-Ray Absorption Spectroscopy (XAS).

Once computed the equilibrium geometries, we evaluated the energy gap between the ground and metastable states.

$$\Delta E_{MS-GS} = E_{MS} - E_{GS} \quad (4.1.1)$$

where E_{GS} and E_{MS} are the energy at the equilibrium geometry for the ground and metastable state, respectively.

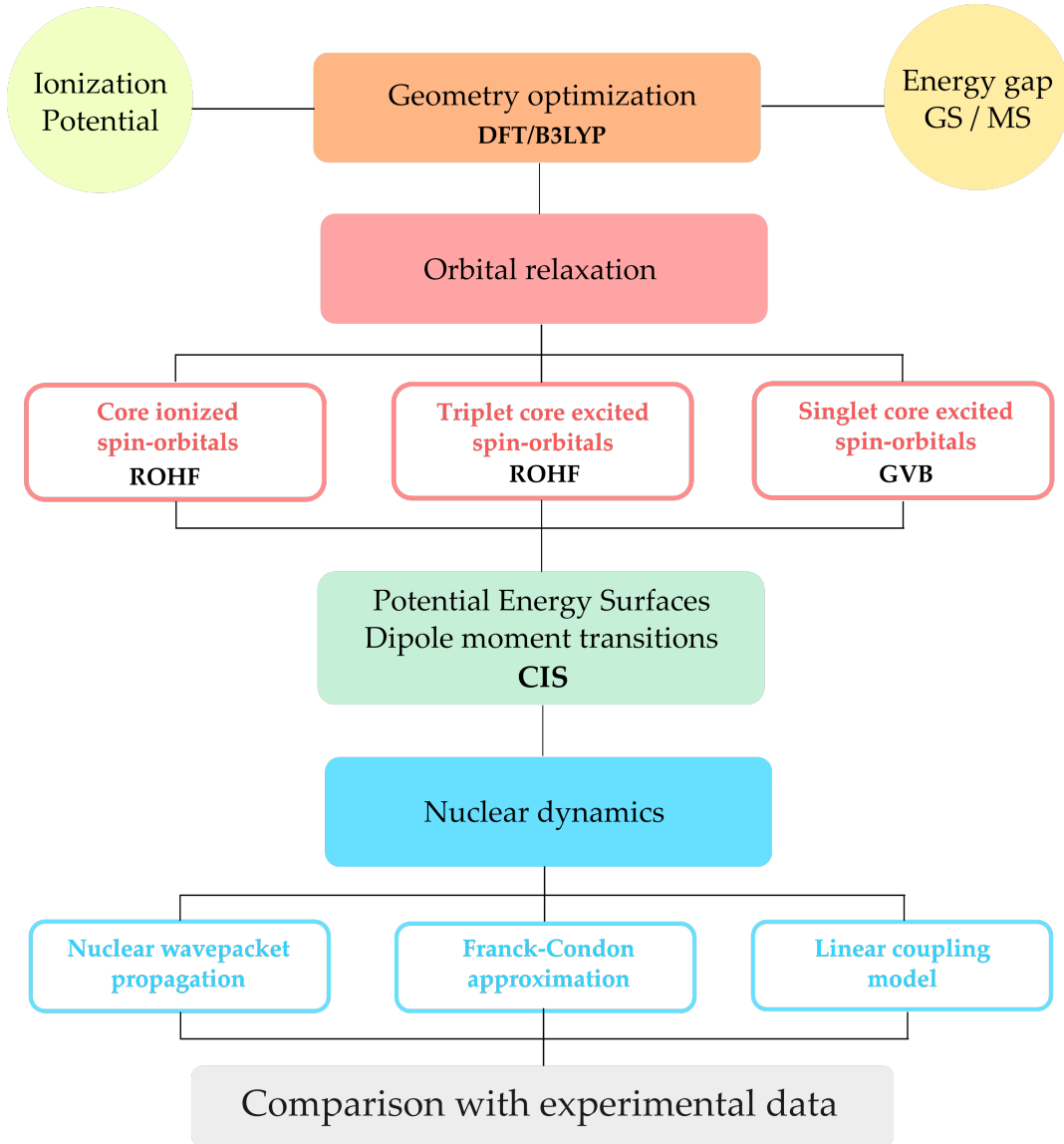


Figure 4.1: Scheme of the calibration of the K-shell protocol

The K-shell ionization potential (IP) was computed through the Δ SCF method

$$IP = [E_{KS}(X^+) - E_{KS}(X)] + \Delta_{SO} \quad (4.1.2)$$

where $E_{KS}(X^+)$ and $E_{KS}(X)$ are the Kohn-Sham total energies of the ionized and ground state system, respectively and Δ_{SO} is a corrective term for the spin-orbit coupling interaction. This

interaction is not important for the K-shell IP of light elements and then was neglected.

Optimization of the guess and active space choice

The creation of a core hole leads the higher orbitals to relax around the hole because of strong changes in the potential felt by the outer electrons.

As described in the previous Chapter, the CIS method provides a simple and relatively cheap technique for the calculations of the excited energies. However, such a simple expansion cannot recover the strong electronic relaxation. It is therefore necessary to use a set of orbitals which take into account the relaxation. For a generic system with 6 electrons, as i.e. CH^+ , the ground state and unrelaxed wavefunction can be written as

$$|\psi_0\rangle = |a^2 b^2 c^2 r^0 s^0 t^0 \dots\rangle \quad (4.1.3)$$

In order to include the relaxation we tested sets of orbitals optimized for three possible configurations which involve a hole in the core orbital

$$|\psi^{CIon}\rangle = |a'^1 b'^2 c'^2 r' s' t' \dots\rangle \quad (4.1.4a)$$

$$|\psi^{TCE}\rangle = |a'^1 b'^2 c'^2 r'^1 s' t' \dots\rangle \quad (4.1.4b)$$

$$|\psi^{SCE}\rangle = |a'^1 b'^2 c'^2 \bar{r}'^1 s' t' \dots\rangle - |\bar{a}'^1 b'^2 c'^2 r'^1 s' t' \dots\rangle \quad (4.1.4c)$$

where $|\psi^{CIon}\rangle$, $|\psi^{TCE}\rangle$ and $|\psi^{SCE}\rangle$ are core ionized, triplet core-excited and singlet core-excited determinant, respectively. The bar over the spin-orbitals indicates electrons with spin β . In the determinants presented in Eq. 4.1.4a - 4.1.4c, the single Slater's determinant of the ground state (Eq. 4.1.3) was used as guess for the spin-orbital optimization through a variational SCF procedure fixing the occupancy of the 1s orbital to one. In the next chapter, we show that the set of spin-orbitals optimized for the lowest triplet core-excited CSFs (Eq. 4.1.4b) is more adapted for the calculation of the XAS spectrum.

Furthermore, the computational cost of the CIS calculation increases with the number of orbitals and excited states required. In order to reduce this cost, we searched for the optimal size of active space (i.e. number of orbitals included in the calculations). We found that it is possible reduce the size of the active space discarding the MOs having energies above the ionization threshold without losing of informations from the photoabsorption spectrum (Chapter 5.1.2) and this makes the calculations three times faster.

Potential energy surfaces and dipole moment transitions

The core-ionized or excited wavefunctions (Slater's determinant) presented above are used as reference for the generation of the CSFs of CIS level of theory calculations. The latter provides the dipole moment transitions (Eq. 1.2.5) and the potential energy surfaces.

In the following chapters, we employ the Taylor expansion to approximate the bounded (harmonic approximation) and dissociative PESs as explained in Chapter 2. In order to verify the validity of this approximation, we computed also the complete PESs.

Nuclear dynamics

The PESs and dipole moment transitions precedentely presented are input data for the nuclear dynamics simulations. The latter provides the cross sections (Eq. 2.4.26).

In order to probe the loss of informations which occurs when the harmonic approximation (HA) is introduced we compared the Frank-Condon (FC) factors computed with different approximation of the PESs. Furthermore, the role played by the electronic correlation in the calculations is investigated. First, we used the CISDT method to compute the complete PESs (ND-I.A). Within the same method, we used the HA to study the effects of the PESs approximation on the FC factors (ND-I.B). In the last, the HA was used to simulate the PESs computed at CIS level (ND-II) in order to investigate the effects of the less correlated method. The three methods are summarized in Table 4.1.

ND-I	A	PES computed at CISDT level
	B	PES computed at CISDT level using HA
ND-II		PES computed at CIS level using HA

Table 4.1: Summary of the techniques used to take into account the nuclear dynamics of the core excited states.

Comparison with the experimental data

The spectra obtained with the aforementioned approaches are then compared with the experimental data. In order to evaluate the presence of metastable species and the ratio between the ground and metastable molecular ions, a comparison with the experimental cross sections was performed using a least-square best fit procedure

$$\sigma(\omega) = p_{GS}\sigma_{GS}(\omega) + p_{MS}\sigma_{MS}(\omega) \quad (4.1.5)$$

where p_{GS} and p_{MS} are the weight coefficients corresponding to the population in the ground and metastable state, respectively.

4.2 L-shell molecular ions

For silicon based molecular ions, we investigated the L-shell excited states. This choice is dictated from the fact that the L-edge provides a complementary method to the K-edge since it permits to explore core-excited states which cannot be explored using the latter due to the dipole moment transition selection's rules. Furthermore, the 2p excitation energies are around 100 eV falling into the soft X-ray region (as well as CH_n^+ and OH_n^+) while the 1s shell needs higher energies in the order of 1800 eV [40].

The principal problem to work at the L-shell threshold is the non-negligible Spin Orbit Coupling (SOC). On this subject, an extended theoretical work was carried out on molecule containing chlorine whether on the photoabsorption [80, 81, 82] or on photoionization spectra [83].

In the first part of this section, we focus our attention on the XAS of the different protonated silicon molecular ions SiH_n^+ ($n = 1 - 3$) using, as done before for the K-shell, the simplest one as case study to establish the protocol. In the second part of the section, we consider the spin-orbit effects in the calculations of the 2p ionization potential.

4.2.1 Photoabsorption spectra

The flowchart presenting the protocol for the L-shell excited systems is reported in Fig. 4.2. After the geometry optimization and the L-shell IP calculations, we compute the transition dipole moments with the CIS method using the orbitals optimized for the lowest triplet core-excited state, as in the K-shell protocol. In this last step, we have performed a study on the effects of the active electrons included in the CIS expansion. The calibration of the XAS protocol at the 2p excitation threshold was carried out for SiH^+ molecular ion as case study.

Geometry optimization and ionization potential

As for the K-shell photoabsorption spectra, the equilibrium geometries for the molecular ions were computed using the DFT method. The energy gap between the molecular ion in the ground and metastable states was computed through Eq. 4.1.1. Furthermore, the ionization potentials were evaluated using Eq. 4.1.2 without taking into account the spin-orbit correction.

Potential energy surfaces, spin orbit coupling and dipole moment transitions

The orbitals relaxed for the first core-excited state were used as starting point to compute the PESs and the dipole moment transitions using CIS method. The harmonic approximation was used since the SOC calculations are highly time demanding. In those calculations, the active space contains orbitals having energy up to 150 eV which is slightly higher than the 2p ionization threshold computed without spin orbit correction.

The spin-orbit coupling effects were taken into consideration through the Breit-Pauli operator which has the following form

$$\hat{H}_{SO} = \frac{\alpha^2}{2} \left\{ \sum_{i=1}^{N_{el}} \sum_{I=1}^{N_{atoms}} \frac{Z_I}{|\mathbf{r}_i - \mathbf{R}_I|^3} [(\mathbf{r}_i - \mathbf{R}_I) \times \mathbf{p}_i] \cdot \mathbf{S}_i - \sum_{i=1}^{N_{el}} \sum_{j \neq i}^{N_{el}} \frac{1}{|\mathbf{r}_i - \mathbf{r}_j|^3} [(\mathbf{r}_i - \mathbf{r}_j) \times \mathbf{p}_i] \cdot [\mathbf{S}_i + 2\mathbf{S}_j] \right\} \quad (4.2.1)$$

where α is the fine structure constant, Z_I are the nuclear charges, r_i and R_I are the electron and nuclear coordinates, respectively, \mathbf{p}_i is the electron momentum operator and \mathbf{S}_i is the electron spin operator. In Eq. 4.2.1, the first double sum is also known as *one-electron (1e)* SOC operator while the second double sum is the *two-electrons (2e)* SOC operator.

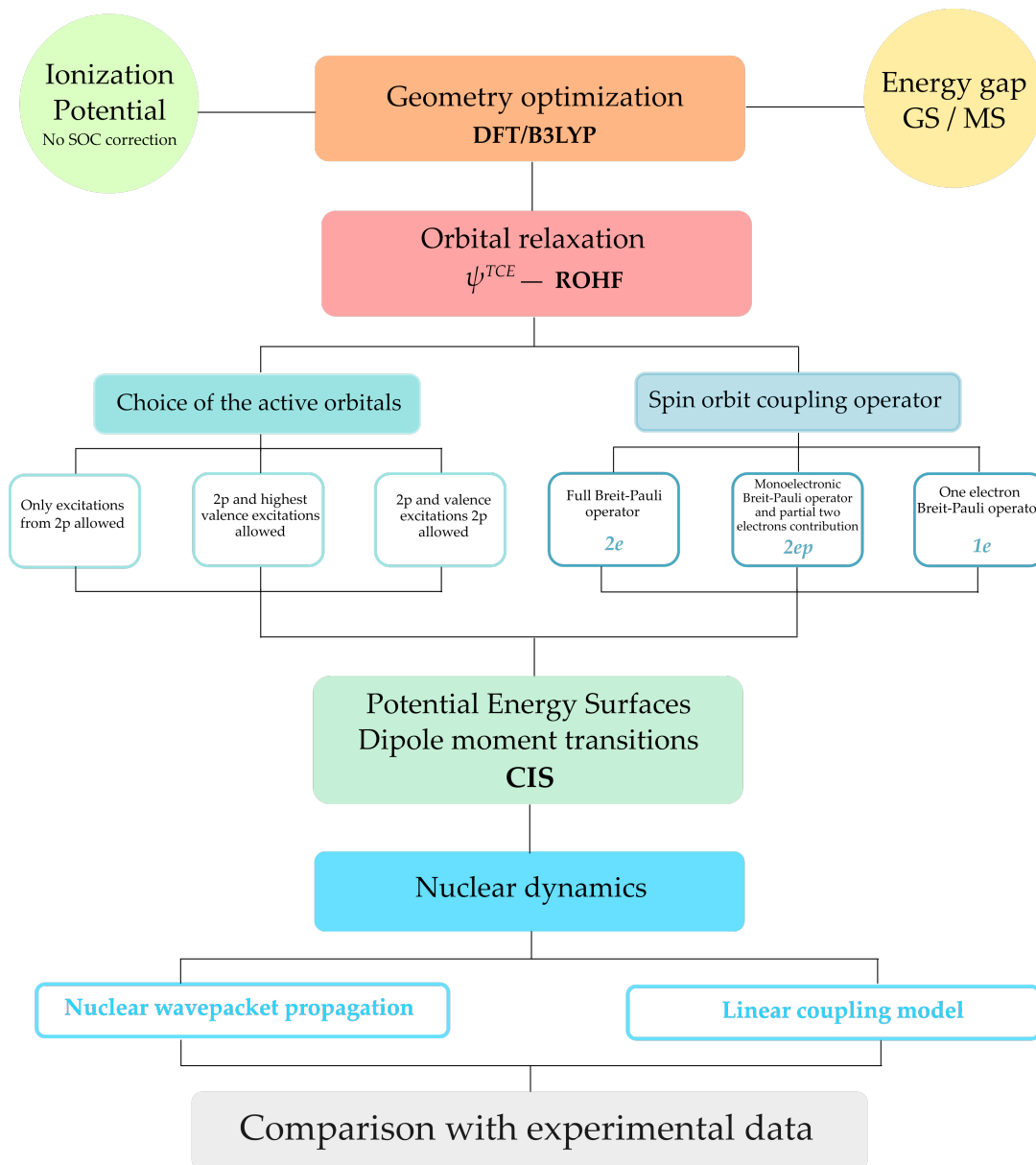


Figure 4.2: Scheme of the calibration of the L-shell protocol

Fedorov *et al.* [84] implemented in the GAMESS-US package [85] the Breit-Pauli operator such that it is possible to include the spin orbit corrections separately for the one and two-electrons operators ($1e$ and $2e$) and through an intermediate partial two electrons contribution ($2ep$). Then the SOC Hamiltonian can be rewritten in term of three different contributions

$$\langle \Psi_{S,M_S} | \hat{H}_{SO} | \Psi_{S,M_S} \rangle = \hat{H}_{act-act}^{1e} + \hat{H}_{core-act}^{2e} + \hat{H}_{core-core}^{2e} \quad (4.2.2)$$

where “core” and “act” is referred to the frozen and active electrons, respectively. The methods *1e*, *2ep* and *2e* presented before are generally defined as follow:

$$1e \quad \langle \Psi_{S,M_S} | \hat{H}_{SO} | \Psi_{S',M'_S} \rangle = \hat{H}_{act-act}^{1e} \quad (4.2.3a)$$

$$2ep \quad \langle \Psi_{S,M_S} | \hat{H}_{SO} | \Psi_{S',M'_S} \rangle = \hat{H}_{act-act}^{1e} + \hat{H}_{core-act}^{2e} \quad (4.2.3b)$$

$$2e \quad \langle \Psi_{S,M_S} | \hat{H}_{SO} | \Psi_{S',M'_S} \rangle = \hat{H}_{act-act}^{1e} + \hat{H}_{core-act}^{2e} + \hat{H}_{core-core}^{2e} \quad (4.2.3c)$$

A deep and exhaustive algebraic treatment of Eqs. 4.2.3a - 4.2.3c can be found in ref. [84] and the details go beyond the scope of this discussion. Nevertheless, it is important to know that in the *1e* method the neglected two-electron term is approximatively replaced by semiempirical effective charge, Z_{Ieff} .

The evaluation of the SOC matrix represents the most time-consuming step because the evaluation of the Breit-Pauli matrix elements of the two-electron integrals. Therefore the implementation of the *1e* and *2ep* methods introduces the possibility to reduce the time and space disk requirements. In this work, we studied the best balance between the number of excited electron included in the CIS calculation using the frozen core-approximation and the different methods for the evaluation of the spin orbit couplings.

Nuclear dynamics

The PESs were computed within the harmonic approximation. For SiH^+ , the core-excited states dynamics was probed with the nuclear wavepacket propagation. This method was not affordable for the SiH_n^+ ($n = 2, 3$) molecular ions for two reasons 1) since the molecular ions in the ground and metastable configuration present very different geometries, it is necessary to compute the PESs beyond the HA approximation but 2) the computational cost of a single point calculation is too high. It takes 26 hours for SiH^+ and more than 90 hours for SiH_2^+ and SiH_3^+ (on Intel Xenon 3 GHz processors). The X-ray photoabsorption cross sections were therefore computed with the LCM presented in Chapter 2.

Comparison with the experimental data

The comparison with the experimental data provided the population of the ground and metastable states throughout Eq. 4.1.5.

4.2.2 L-edge ionization potential

The 2p ionization energies are affected by the chemical environment and the spin orbit coupling. For a given atom, the creation of a new bond lifts the degeneracy of the $2p_{x,y,z}$ atomic orbitals (Fig. 4.3), this effect is called *molecular field* (MF). Moreover, for the 2p orbitals, the spin orbit interaction is non-zero and a further contribution to the splitting has to be taken into consideration.

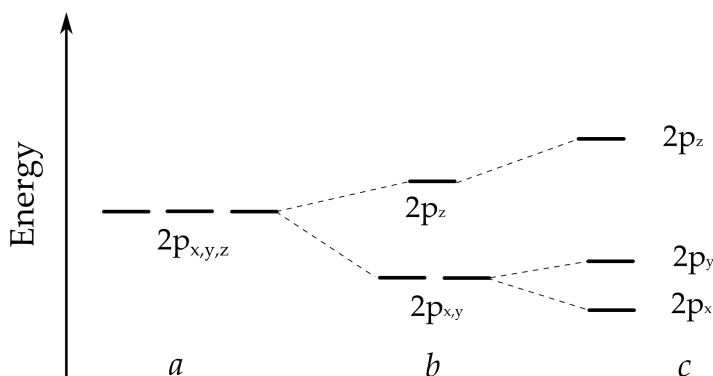


Figure 4.3: General scheme of the lift of degeneracy in the 2p orbitals with the introduction of the molecular field. *a* the 2p orbitals are completely degenerate, *b* and *c* the molecular field lift partially and completely the degeneracy, respectively

The SiH_n^+ molecular ions provide an example of the combination between the MF and spin-orbit coupling interaction. They provides two different pictures: the $2p_{x,y}$ orbitals are degenerate (Fig. 4.3.b) and the degeneracy is completely lifted (Fig. 4.3.c).

As seen in the previous section, the SOC interaction can be included in the calculation through the Breit-Pauli operator but the high time consuming does not permit to include the correlation effects through the inclusion of higher excitations in the CI method (CISD, CISDT, ...). The derivation of an effective Hamiltonian can permit to bypass the Breit-Pauli operator and compute ionization threshold with more correlated methods in order to better compute absolute and relative energies.

The effective Hamiltonian for the spin-orbit couplings can be generally written as

$$\hat{H}_{SO} = \sum_{i=1}^{n_{el}} \hat{P}_{2p}(\Omega \hat{l}_i \hat{s}_i) \hat{P}_{2p} \quad (4.2.4)$$

where \hat{P}_{2p} is the projection operator on the 2p orbitals of silicon, \hat{l}_i and \hat{s}_i are the angular and spin operator and Ω is the spin orbit coupling parameter associated to the silicon 2p shell. Ω is a constant that can be positive or negative and that we consider positive for convention.

In the case of closed shell system where the $2p_{x,y}$ orbitals are degenerate (Fig.4.2b) the ionized final state, generally labelled $2p^{-1}$, has doublet spin multiplicity. This leads to have six wavefunction characterized by values of angular l , magnetic m_l and spin m_s quantum number as reported in Table 4.2.

$2p^{-1}$ state	l	m_l	m_s
$2p_{\pi+}^{\alpha}$		+1	1/2
$2p_{\pi+}^{\beta}$		+1	-1/2
$2p_{\sigma}^{\alpha}$	1	0	1/2
$2p_{\sigma}^{\beta}$		0	-1/2
$2p_{\pi-}^{\alpha}$		-1	1/2
$2p_{\pi-}^{\beta}$		-1	-1/2

Table 4.2: Relativistic states for core ionized state ($2p^{-1}$) with doublet spin multiplicity.

For this system, effective spin-orbit matrix has the following form

$$H_{SO}(2p^{-1}) = \begin{pmatrix} E(^2\pi_+) + \Omega/2 & 0 & 0 & 0 & 0 & 0 \\ 0 & E(^2\pi_-) - \Omega/2 & 0 & 0 & 0 & \Omega/\sqrt{2} \\ 0 & 0 & E(^2\sigma) & \Omega/\sqrt{2} & 0 & 0 \\ 0 & 0 & \Omega/\sqrt{2} & E(^2\pi_+) - \Omega/2 & 0 & 0 \\ 0 & 0 & 0 & 0 & E(^2\pi_-) + \Omega/2 & 0 \\ 0 & \Omega/\sqrt{2} & 0 & 0 & 0 & E(^2\sigma) \end{pmatrix} \quad (4.2.5)$$

The details concerning the derivation of the matrix in Eq. 4.2.5 from Eq. 4.2.4 are provided in Appendix A. The eigenvalue of the $2p^{-1}$ states obtained by diagonalization of the

matrix in Eq. 4.2.5 are reported in the follow

$$\textcircled{1} E_{\pi_{\pm}} + \frac{\Omega}{2} \quad (4.2.6a)$$

$$\textcircled{2} \frac{[E_{\pi_{\pm}} + E_{\sigma} - \frac{\Omega}{2}] \pm \sqrt{\left[E_{\pi_{\pm}} - \frac{\Omega}{2} + E_{\sigma}\right]^2 - 4\left[E_{\pi_{\pm}} + \left(E_{\sigma} - \frac{\Omega}{2}\right) - \frac{\Omega^2}{2}\right]}}{2} \quad (4.2.6b)$$

Since Ω is an unknown constant, it was evaluated finding the best value which reproduces the relativistic energies computed through the Breit-Pauli operator at CIS level. Once we evaluated Ω , we used the CISDT method to compute the energies in Eq. 4.2.5 and diagonalize the matrix in order to obtain more accurate SOC energies.

A system which has $2p^{-1}$ final state with singlet or triplet multiplicity possesses 12 wavefunction and the derivation of the effective matrix is more tedious. This work is under progress.

For the silicon molecular ions different cases are possible: closed-shell case, SiH_n^+ ($n=1, 3$), where $2p_{x,y}$ are degenerate (Fig. 4.2b) and the open-shell case, SiH_2^+ , where the degeneracy is completely suppressed owing to MF (Fig. 4.2c). In Chapter 7, the results of the XPS spectra of SiH^+ and SiH_3^+ are presented. The vibrational analysis of the spectrum was carried out using the LCM afore presented.

A general scheme of the calculation of the core binding energies is reported in Fig. 4.4.

4.3 Computational details

The electronic structure calculations were carried out with the quantum chemistry package GAMESS-US [85]. For all calculations, a aug-cc-pvQz basis set [86] was used on all atoms and 7s,6p,5d,3f diffuse functions were added on the elements involved in the excitation to improve the description of the Rydberg transitions.

The equilibrium geometries as well as the energy gap between the ground and metastable molecular ions were computed using the Becke three parameter hybrid exchange [87] and the Lee-Yang-Parr gradient-corrected correlation functional [88, 89].

The RHF orbitals obtained for the ground state of each species were used as guess for the ROHF (or GVB) optimization of the orbitals when the 1s or 2p hole is created. The relaxed orbitals are then used to compute the PESs and the transition dipole moments on the length

gauge. The vertical cross sections were computed using a Voigt's profile (Eq. 2.4.5).

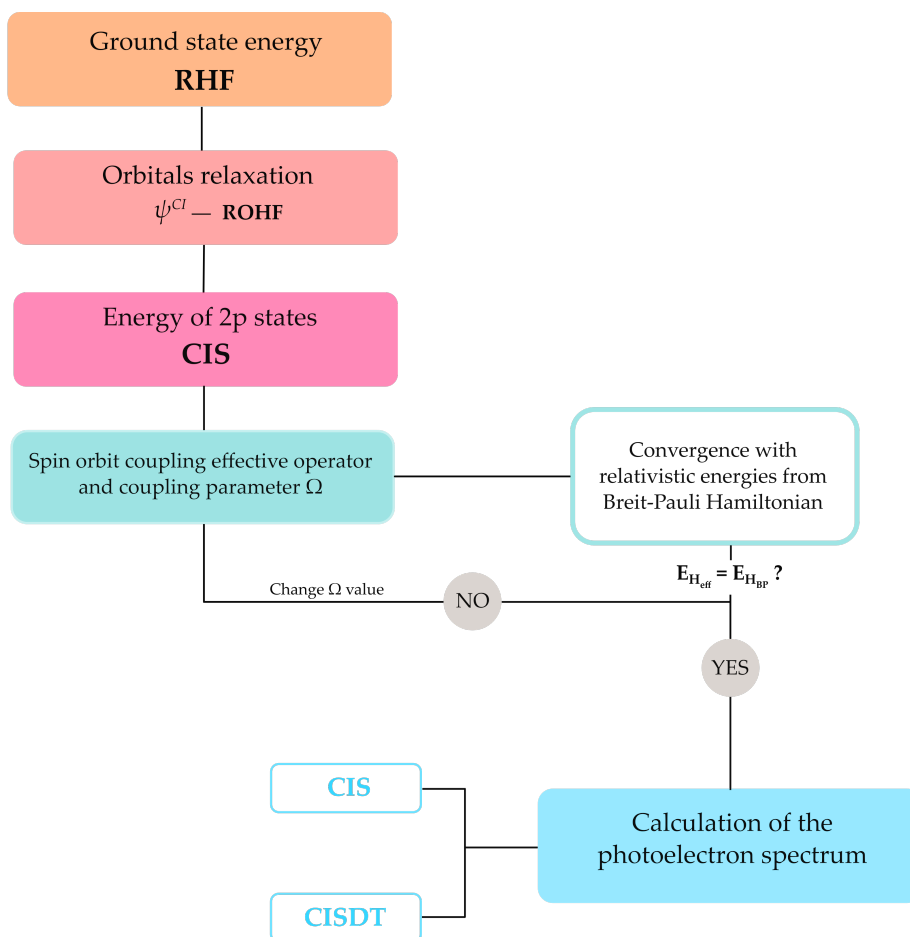


Figure 4.4: Scheme of the calculation of photoelectron spectra

Energies at the CISDT level were obtained with the Occupation Restricted Multiple Active Space (ORMAS) method [90] implemented in GAMESS-US package. It should be noticed that within the ORMAS method it is not possible to compute the dipole moment transitions.

The wavepacket propagation calculations were performed using a code developed in our group. The Auger decay widths for all systems were taken from literature [91, 92] and were assumed to be independent on both the core-excited electronic states and internuclear distance. Their values were fixed at 109 meV (6 fs), 160 meV (4 fs) and 45 meV (15 fs) for CH_n^+ , OH_n^+ and SiH_n^+ , respectively. The cross sections were computed as Fourier transform of the autocorrelation function (Eq.2.4.26) including the convolution with the Gaussian profile in order to include the

experimental band pass.

Molecular ion	Core-hole lifetime (fs)	Broadening Γ (meV)	Experimental band pass (meV)
CH_n^+	6	109	280
OH_n^+	4	160	200
SiH_n^+	15	45	80

Table 4.3: Core hole lifetime and experimental band pass for the XH_n^+ ($X = \text{C}, \text{O}, \text{Si} - n = 1, 2, 3$) molecular ions

Results and discussion

*“You can only analyze the data you have.
Be strategic about what to gather and how to store it”*
— Marie Skłodowska Curie

5

X-ray absorption spectra of CH_n^+ and OH_n^+ molecular ions

In Chapter 5 are presented the results of the calibration of the protocol for the K-shell molecular ions and its application to the study of the X-ray photoabsorption spectra of Carbon and Oxygen based molecular ions CH_n^+ and OH_n^+ ($n=1-3$).

The Chapter is divided in three main sections. In Section 5.1 is presented the study concerning the development of the protocol for K-shell excited molecular ions using CH^+ as case study. Point by point, the different aspects presented in the previous Chapter are analysed: starting from the equilibrium geometry and IP calculations going then deeply in the X-ray photoabsorption spectra calculations. We investigate the effects of the spin-orbitals relaxation and the importance of the nuclear dynamics in the core-excited state. Finally, the comparison with experimental data is carried out.

In Section 5.2 and 5.3, the chosen methodology is applied to CH_n^+ and OH_n^+ molecular ions ($n = 2, 3$), respectively. In these cases, results from the experimental set-up, presented in the Introduction, predict a nearly zero XAS in disagreement with our calculations. Reasons for this discrepancy are discussed.

5.1 CH^+ as case study to the calibration of the method

5.1.1 Geometry optimization and ionization potential

In the ground state CH^+ is a closed shell system with electronic configuration of $(1s\sigma)^2 (2s\sigma)^2 (3\sigma^2)$. It is termed $^1\Sigma^+$ and $^3\Pi$ in ground and valence excited states, respectively. The energy gap between the two was computed at DFT/B3-LYP level and it is estimated to be 0.927 eV close to the value computed by Green *et al.* [93] (1.14 eV).

The computed internuclear distance for CH^+ ground state is 1.135 Å which is good agreement with the theoretical literature value of 1.130 Å [93]. For this molecular ion no experimental bond distance are available in literature. However, the bond length of CH^+ can be compared to that of the neutral species CH since the difference between the bond distance for the neutral XH and ionized species XH^+ for X = B, N, O are small [94, 95]. The CH bond length is 1.131 Å which is close to the value we obtained for CH^+ . The computed ionization threshold for the 1s electron of the Carbon is 312 eV at DFT/B3-LYP level.

5.1.2 Optimization of the spin-orbitals and the active space choice

The photoabsorption spectrum for CH^+ was computed using three different sets of spin-orbitals: optimized for the core ionized *CIon* and lowest triplet *TCE* and singlet *SCE* core-excited states. Using the ground state orbitals computed at RHF level as guess, the ROHF method was used for the optimization of the first two while the lowest singlet core-excited state was optimized through the GVB method. This step of the study was carried out using a aug-cc-pvQz basis set.

For the three sets we use the complete active space (i.e. all spin-orbitals available) or a smaller set of it. In the latter we kept all orbitals with energy lower than 350 eV which corresponds to energy slightly greater than the K-shell ionization energy. This permits to reduce the active space from more than 200 MOs to 52 and with it the computational cost.

In Table 5.1, we compare the energy position and oscillator strength of the lowest (and most intense) transition at the equilibrium distance obtained with the different approaches. The energy position of this transition is compared to the more accurate values obtained at the CISDT level using the singlet core-excited set of spin-orbitals. At CISDT level, the values of the energy transition are 285.86 eV for the complete active space calculations and 285.65 eV for the reduced active space ones.

Guess reference	Transition involved	Active Space	E transition (eV)	Oscillator strength	ΔE
Core ionized	$1s \rightarrow \pi$	Complete	284.74	0.10870	1.12
		Reduced	283.23	0.11636	2.42
Singlet core excited	$1s \rightarrow \pi$	Complete	285.91	0.14762	0.05
		Reduced	283.31	0.15049	2.34
Triplet core excited	$1s \rightarrow \pi$	Complete	285.49	0.13805	0.37
		Reduced	283.84	0.14699	1.81

Table 5.1: Energy and oscillator strength associated to the lowest transition ($1s \rightarrow 1\pi$). ΔE is the energy difference between the first transition computed at CIS level and the energy difference computed at CISDT level.

The energy position is best described when the spin-orbitals optimized for the singlet core-excited orbitals are used with complete active space. The difference with the CISDT calculations is only 0.05 eV. However, when the active space is reduced the best choice is the set of spin-orbitals optimized for the triplet core excited reference. The oscillator strength changes by at most 50% depending on the choice of the initial guess of spin-orbitals.

We further study the effects of the chosen set of spin-orbitals and active space on the higher transitions. In Fig. 5.1 are reported the simulated spectra for the different optimized spin-orbitals and actives spaces. The spectra were simulated using a Voigt profile (Eq. 2.4.5) using a FWHM of the Gaussian profile equal to 200 meV which corresponds to the experimental band pass [32]. For comparison, all spectra were shifted such that the first transition matches that obtained at the CISDT level.

The Fig. 5.1 shows that the global shape of the spectra and the electronic transitions involved in the excitation are invariant with respect to the choice of the spin-orbitals and active space. This is better shown in Fig. 5.2 where the simulated spectra are reported in logarithmic scale.

In Fig. 5.3 are reported the principal orbitals involved in the electronic transition. The most intense peak corresponds to the transition from the $1s$ toward the first two π MOs that are degenerate and the second is assigned to the $1s \rightarrow 1\sigma^*$ transition. Absorption lines at higher photon energy correspond to transitions towards Rydberg states.

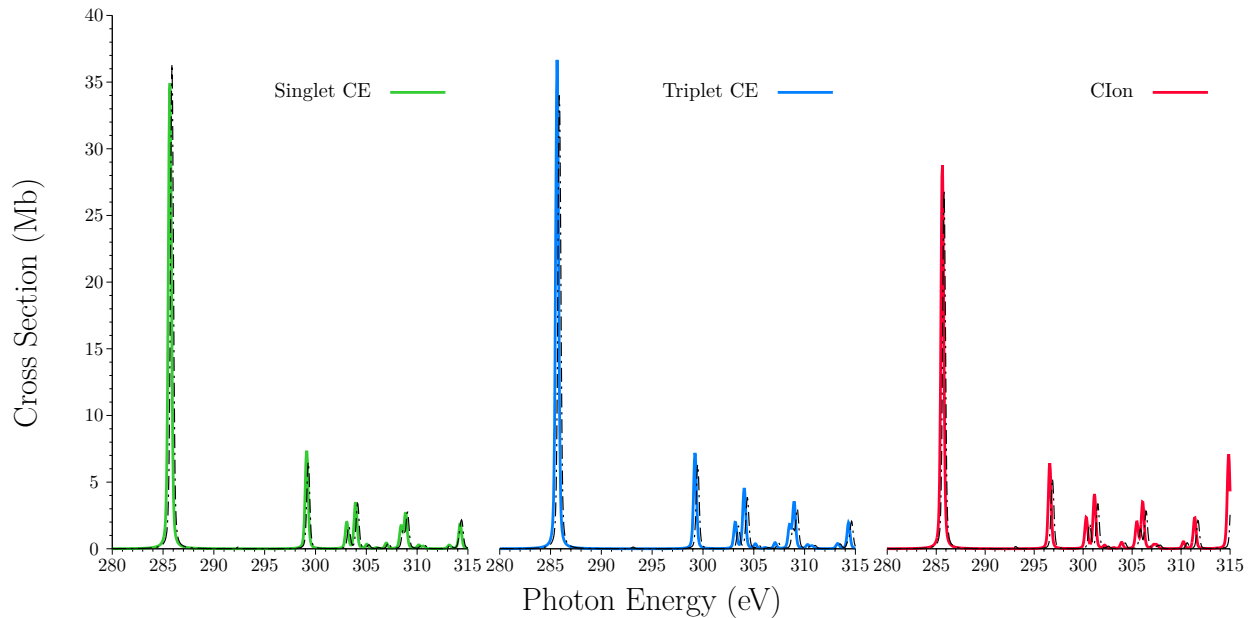


Figure 5.1: Simulated photoabsorption spectra of CH^+ at CIS level with the three different sets of spin-orbitals: singlet core excited (green), triplet core excited (blue) and core ionized (red) spin-orbitals for the complete active space (black dotted line) and the reduced active space (full color line).

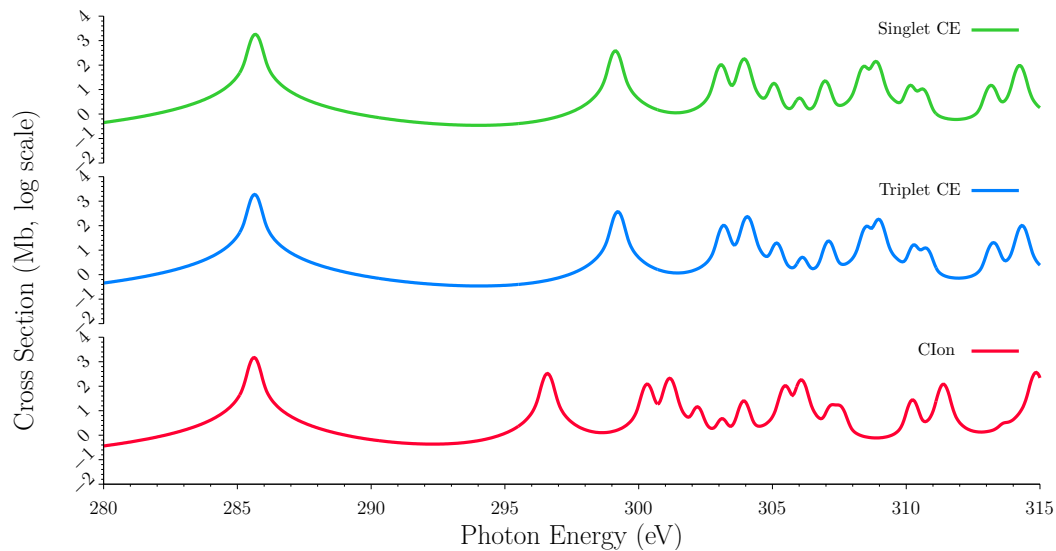


Figure 5.2: Simulated photoabsorption spectra of CH^+ in logarithmic scale. The spectra were computed at CIS level with the reduced active space for the three different sets of spin-orbitals: singlet excited (green), triplet core excited (blue) and core ionized (red) reference.

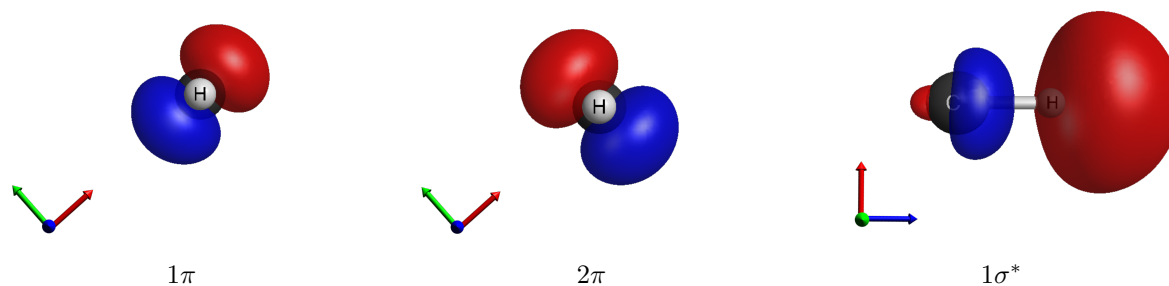


Figure 5.3: CH^+ molecular orbitals involved in the electronic transition.

For the peak at 285.65 eV, it should be noted that for the core excited set of spin-orbitals, we optimize the orbitals fixing the electron in one of the first two π orbitals which slightly lifts the degeneracy, especially for the singlet core excited spin-orbitals. It results in a broader and less intense peak.

As discussed above, the overall shape of the spectra is weakly dependent on the choice of the spin-orbitals and active space. However, the gap between the first two peaks depends significantly on the choice of the spin-orbitals. The core-excited spin-orbitals predict an energy gap of about 13.5 eV while the latter obtained with core-ionized spin-orbitals is only 11.02 eV. In order to determine which set of spin-orbitals provides the best estimate we have calculated this energy difference at CISDT level with the complete active space. The computed energy gap is 11.22 eV which shows that the core excited spin-orbitals overestimate the energy gap by about 2 eV. As shown by Ågren et al [96], spin-orbitals optimized for core-excited state systematically predict larger energy difference between the lowest core-excited state and states in the Rydberg region because of the limited penetration of the latter in the core region. It should be noted that the reduction of active space does not lead to significant changes in the spectra. As shown in Table 5.1, it only introduces a global shift. However, the gain in computational time compared to the complete active space calculations is remarkable (3 times faster).

5.1.3 Nuclear dynamics results

The effects of the dynamics in the core-excited state were evaluated using three different approaches:

- Using the complete PESs computed at CISDT (ND-I.A) level (Fig. 5.4)

- Using the harmonic approximation at CISDT level (ND-I.B)
- Using the harmonic approximation at CIS level (ND-II)

In these calculations we augmented the basis set with 7s, 6p, 5d, 3f diffuse functions in order to improve the description of the Rydberg region. It should be noticed that the dipole moment transitions used in the following were computed at CIS level since they are not available in the package used to the CISDT calculation (ORMAS).

In Table 5.2 are reported the energies and FC factors for the transitions from the fundamental vibrational level ν_0 towards the first five vibrational levels ν'_n ($n = 0 - 4$) of the lowest core-excited state computed using the three methods.

		Frank - Condon factor				
		$\nu_0 - \nu'_0$	$\nu_0 - \nu'_1$	$\nu_0 - \nu'_2$	$\nu_0 - \nu'_3$	$\nu_0 - \nu'_4$
ND-I.A	E	287.26	287.62	287.94	288.26	288.55
	FC factor	0.7773	0.2077	0.0145	0.0002	$< 10^{-6}$
ND-I.B	E	287.28	287.71	288.12	288.52	288.90
	FC factor	0.6730	0.2002	0.0829	0.0277	0.0102
ND-II	E	283.61	283.94	284.26	284.58	284.88
	FC factor	0.4831	0.3726	0.1204	0.0214	0.0023

Table 5.2: Energies and Franck-Condon factors for the transition $\nu_0 - \nu'_n$ ($n = 0 - 4$) computed within the methods ND-I.A, ND-I.B and ND-II.

Comparing the results of the CISDT calculations, we notice that the introduction of the HA does not affect strongly the distribution of the FC factor but influences the vibrational frequencies. Conversely, the comparison between the CIS and the CISDT calculation within the HA shows a strong difference in the FC factor distribution. This effect is probably related to the location of the minimum in the ground and core-excited state which is better described in the CISDT calculation.

Comparing the results reported in Table 5.2 and the vertical energy computed at CISDT level, we observe that the CISDT calculations using the triplet core-excited spin-orbitals overestimate the first transition energy while the CIS calculations underestimate it. This behaviour could be attribute to the fact that the CI method has a slow energy convergence [97] and then the introduction of the triple excitations could not be enough to recover all the correlation

and get the correct transition energies. Nevertheless, we chose to use the CIS since it is less time-demanding.

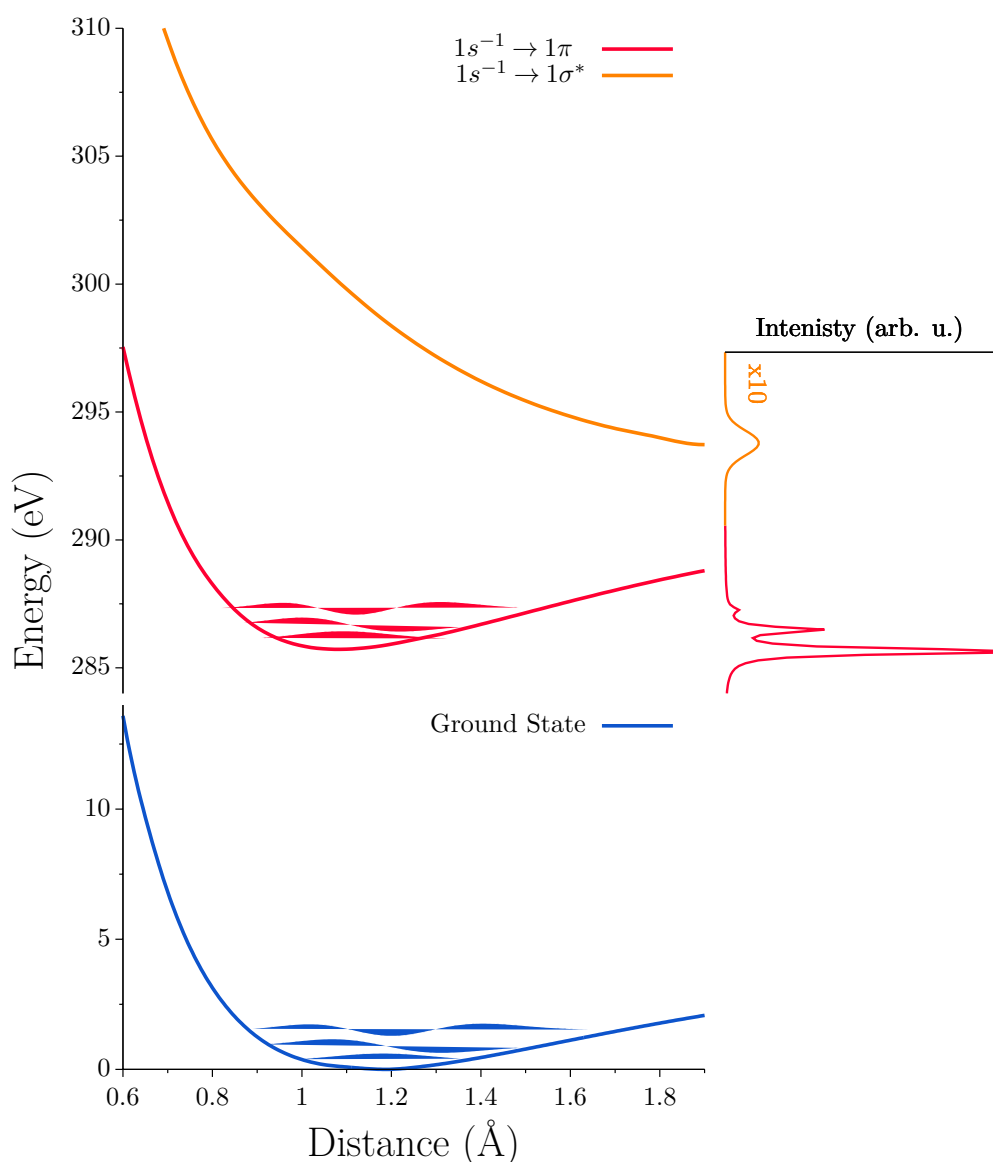


Figure 5.4: Potential energy curves of CH^+ : ground state and relative wavefunctions in blue, first and second core excited state with non zero dipole moment in red and orange, respectively.

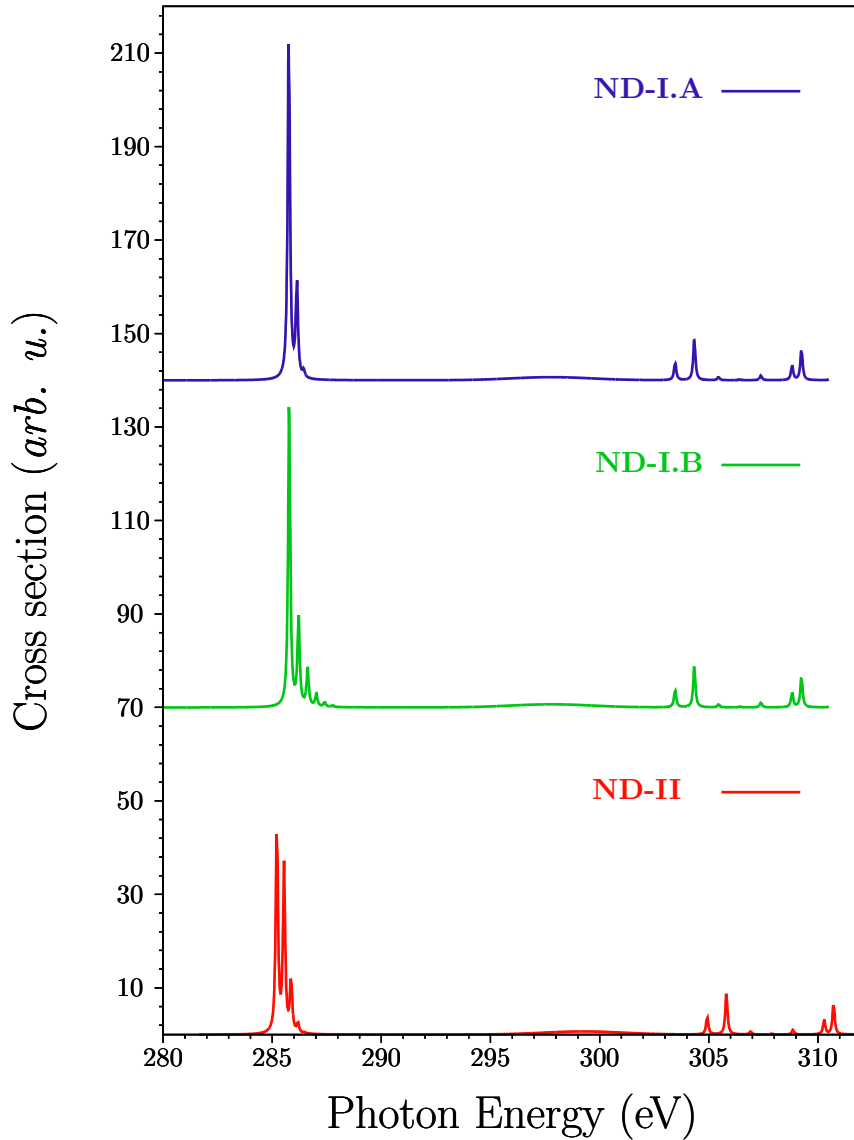


Figure 5.5: Computed Lorentzian spectra within the methods ND-I.A, ND-I.B and ND-II.

We now investigate the effects of the nuclear dynamics on the absorption spectrum comparing in Fig. 5.6 the results from the vertical spectrum (Eq. 2.4.5) and the ones obtained with the nuclear wavepacket propagation (Eq. 2.4.26). The potential energy curves and dipole moment transitions were computed at CIS level with the triplet core excited reference and re-

duced active space were used. The first line centered at 285.65 eV is splitted into three peaks corresponding to transition to the three lowest vibrational levels of the $1, 2\pi$ core-excited state, as seen before. The energy differences between the successive vibrational levels are larger than the lifetime broadening such that with sufficient resolution it is experimentally possible to resolve these structures. On contrary to the first line, the intensity of the second peak (≈ 299 eV) is significantly decreased and broadened over more than 3 eV. This is a demonstration of the dissociative nature of the potential energy curve corresponding to this core-excited state. For higher lines, we see alternance of dissociative and bound states. Owing to small energy separation between the electronic states in this region it is not possible to resolve the vibrational levels of each bound state.

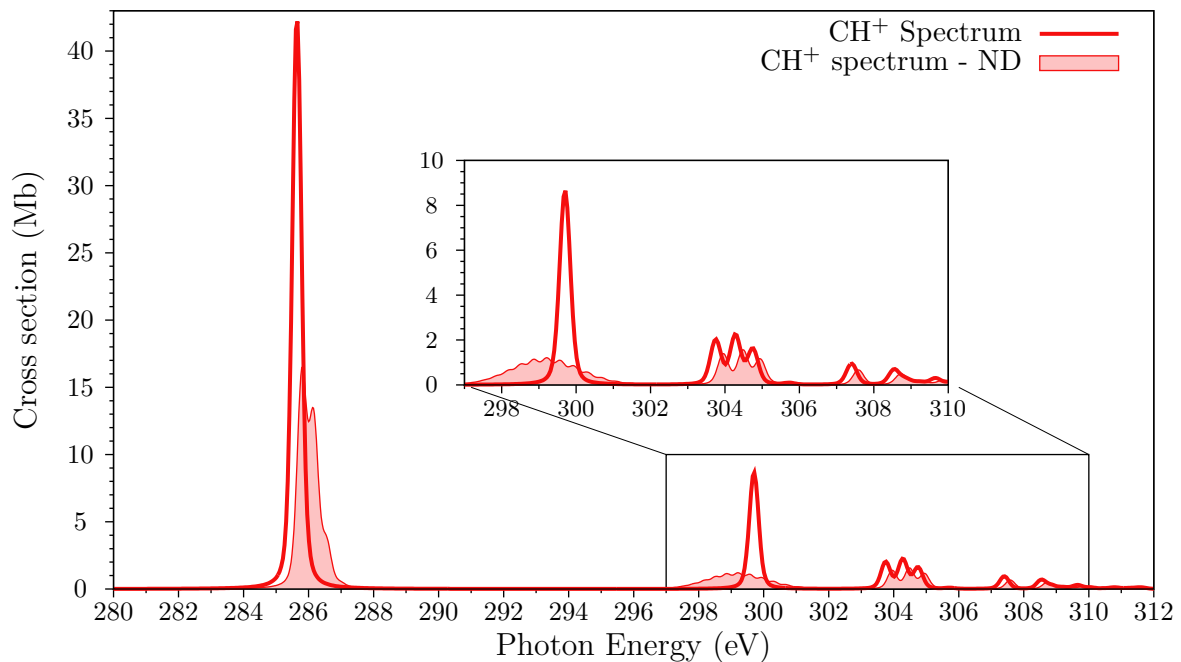


Figure 5.6: Comparison of simulated photoabsorption spectra of CH^+ with and without nuclear dynamics, respectively in filled curve and full line.

The X-ray photoabsorption spectrum of the metastable state presents the same characteristic of the ground electronic state.

From the above presented results appear the important role of the nuclear dynamics. In order to have a good representation of the spectral features, it is necessary to include it in particular when dissociative states are present.

5.1.4 Comparison with experimental data

The comparison between the results from the nuclear wavepacket propagation and the experimental data is reported in Fig. 5.7.

The results of the population fit suggests that 90% of the population is in the ground electronic state and the remaining percentage is in the valence excited state. A global shift of 2.9 eV on the CIS transition energies was applied corresponding to an error of the 1% on the energy position.

The vibrational progression of the main peak at 286.84 eV is experimentally observed since the spacing between $\nu_0 - \nu'_0$ and $\nu_0 - \nu'_1$ is 241 meV, just above the experimental resolution of 200 meV. The agreement between computed and theoretical oscillator strength of the vibrational progression is not perfect (Table 5.3). The experimental oscillator strength distribution is closest to the one computed at CISDT level (Table 5.2) indicating that it is important to take into account the correct displacement of the core excited PESs. The assignment of the transitions toward the $1\sigma^*$ and Ryberg states in the experimental spectrum is difficult to perform because the low photoabsorption cross sections in this region.

According to our simulation, the peak at 283.4 eV in the experimental spectrum is due to the metastable state.

Transition	E_{theory} (eV)	E_{exp} (eV)	f_{theory}	f_{exp}
$\nu_0 - \nu'_0$	286.60	286.84	0.48	0.80
$\nu_0 - \nu'_1$	286.95	287.24	0.38	0.23

Table 5.3: Energy E and oscillator strength f for the $1s \rightarrow \pi$ transitions

In conclusion, the results presented above show that spin-orbitals optimized for the first triplet core-excited state represent a good reference to the CIS calculation. Nevertheless, it is necessary to include in the calculation the nuclear dynamics effects in order to describe the dynamics of the excited state especially for core-excited states with dissociative character. Then this protocol was used to compute the photoabsorption spectra of the CH_n^+ ($n=2, 3$) and OH_n^+ ($n=1, 2, 3$) molecular ions.

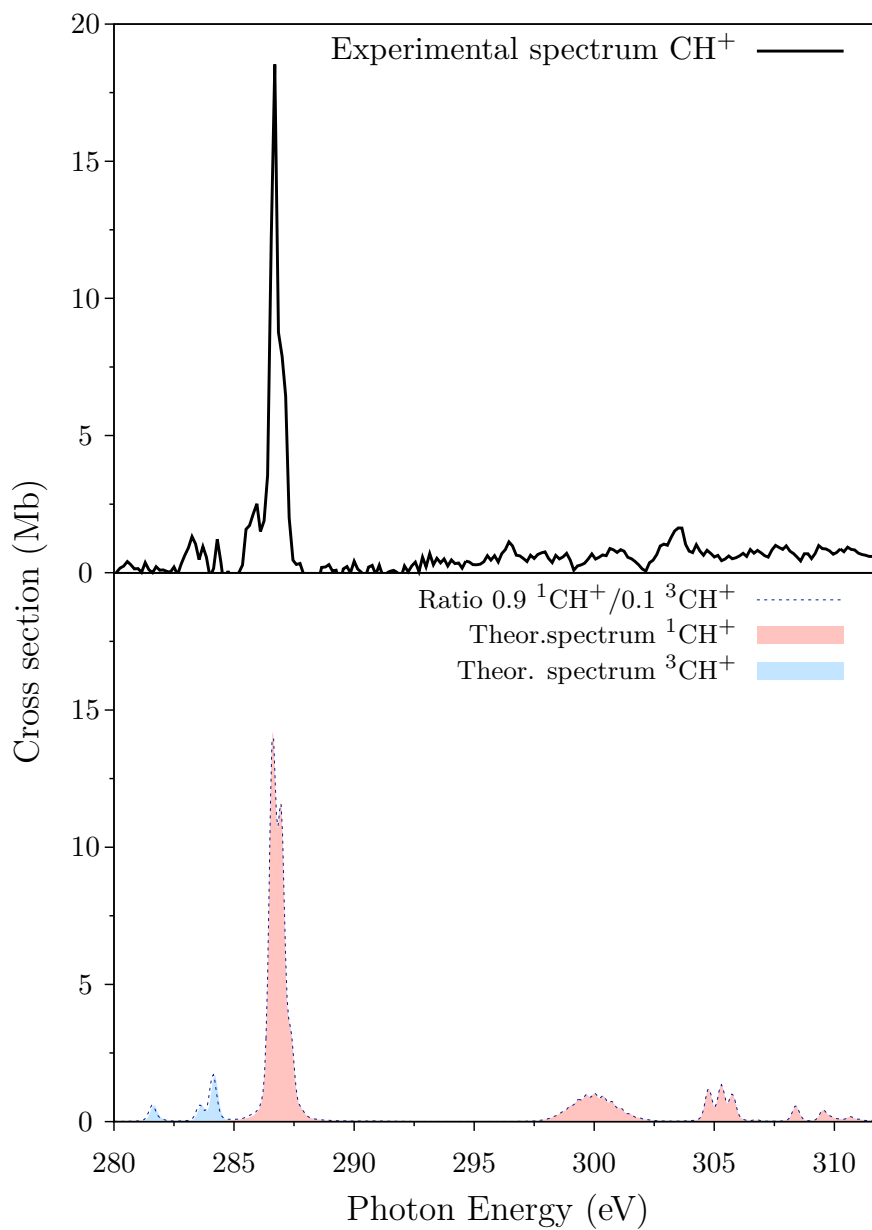


Figure 5.7: Comparison between theoretical (bottom) and experimental (top) results. In the theoretical data, the red and blue filled curve are the computed spectra for the ground and metastable state, respectively and the dashed line is the sum of the two.

5.2 Calculations of the photoabsorption spectra of CH_n^+

In the chosen methodology, the geometry optimization and the K-shell IP calculations are performed with the DFT/B3-LYP method. The spin-orbital relaxation is carried out for the lowest triplet core-excited state. The energies and dipole moment transitions are computed at CIS level. The CH_n^+ spectra were computed neglecting the nuclear dynamic effects.

Experimental spectra for CH_2^+ and OH_2^+ are shown in Fig. 5.8. They are nearly zero. Spectra for CH_3^+ and OH_3^+ are not available. As presented in the Introduction, in the experimental set-up, upon the core-excitation, the double charged atomic ion X^{2+} ($\text{X} = \text{C}, \text{O}, \text{Si}$) formed after Auger decay is detected. Then the low cross sections in Fig. 5.8 correspond to the lack of production of the X^{2+} species. Two hypothesis are moved forward: either for the XH_n^+ ($\text{X} = \text{C}, \text{O}; n=2,3$) systems the electronic transitions present a very low cross section or these molecular ions follow fragmentation pathways that are not detectable in the experimental set-up.

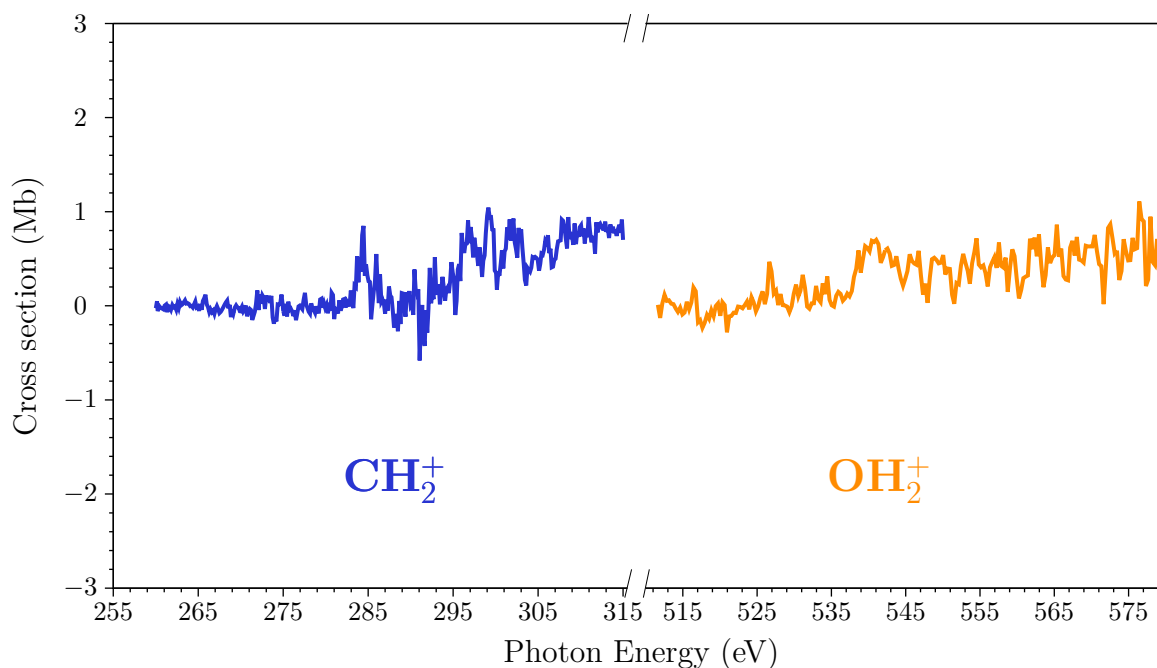


Figure 5.8: CH_2^+ and OH_2^+ experimental spectra.

In the following sections the photoabsorption spectra of XH_n^+ ($\text{X} = \text{C}, \text{O}; n=2,3$) in the

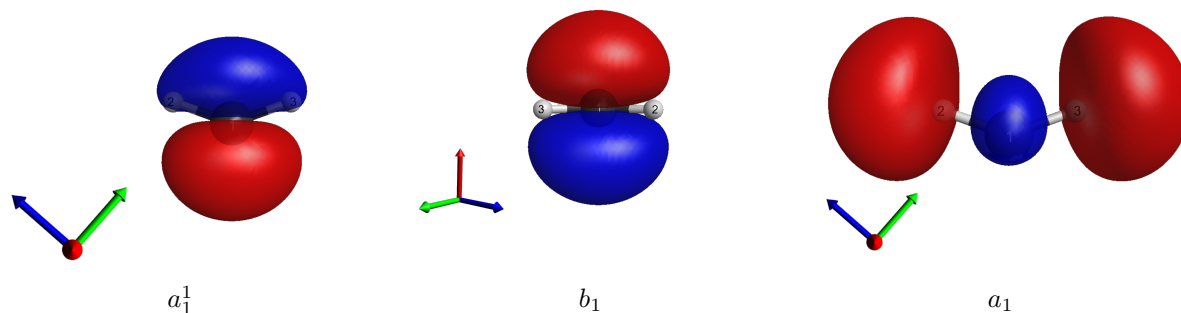


Figure 5.9: CH_2^+ molecular orbitals involved in the electronic transition.

ground state are simulated in order to exclude one of the two possibilities.

CH_2^+

The methylene cation, CH_2^+ in its ground state is a doublet spin system with C_{2v} symmetry and electronic configuration $1a_1^2 2a_1^2 1b_1^2 3a_1^1$. The computed IP for the Carbon 1s shell is 307.5 eV. The geometry and IP data for the CH_n^+ molecular ions are summarized in Table 5.4. As can be observed from this Table, the addition of a proton leads to a lowering if the K-shell potential of 4.5 eV.

	Bond distance C—H (Å) (exp)	$\theta_{\text{H}_2-\text{C}-\text{H}_1}$ (exp)	IP (eV)
$^1\text{CH}^+$	1.135 ^a	—	312
$^2\text{CH}_2^+$	1.09638 ^a	140.47 (144.6 ^b)	307.5
$^1\text{CH}_3^+$	1.0980 ^a	119.9	306.6

a experimental data not available
a data from Ref. [27]

Table 5.4: Geometries and K-shell ionization threshold for CH_n^+ ($n=1, 2, 3$) molecular ions.

In Fig. 5.10 is depicted the computed spectrum for CH_2^+ . It was shifted with respect to the value of the first transition computed at CISD level ($E_{1s \rightarrow a_1^1} = 281.7$ eV). The spectrum has the same features seen before for CH^+ : a main peak centered at 281.7 eV which involves the transition $1s \rightarrow 3a_1$ and $1s \rightarrow 2b_1$. The peak at 295.8 eV corresponds to the transitions $1s \rightarrow 3b_2$ state while the region above corresponds to the Rydberg transitions. The MOs involved in the

excitation are reported in Fig. 5.9.

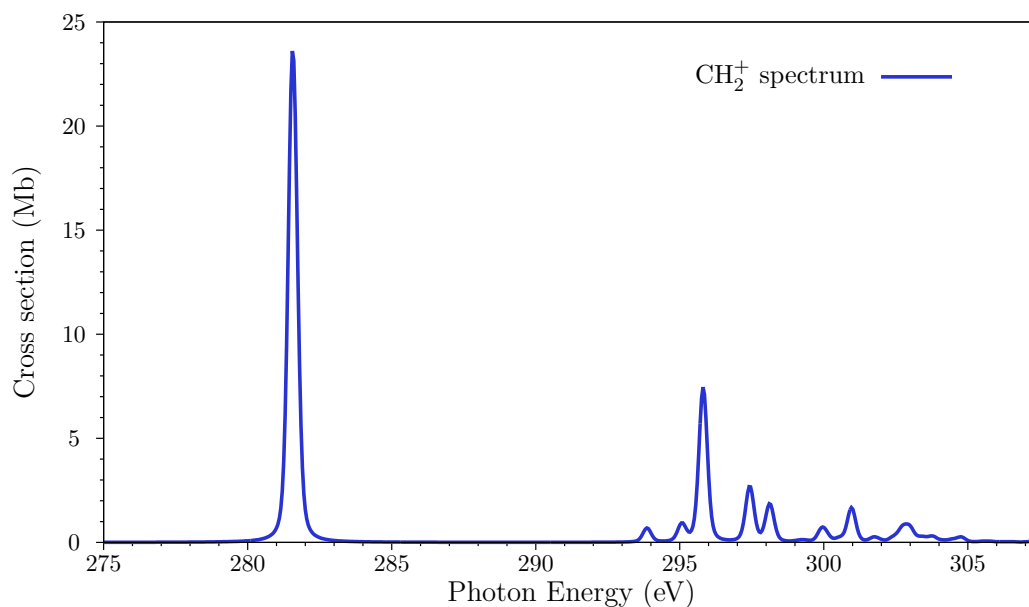


Figure 5.10: CH_2^+ computed X-ray photoabsorption spectrum.

CH_3^+

The CH_3^+ molecular ion has a trigonal planar geometry with point group D_{3h} and it has electronic configuration $1a_1'^2 2a_1'^2 1e'^4$. As reported in Table 5.4, the K-edge IP is computed to be 306.6 eV.

The computed spectrum is shown in Fig. 5.11. The first transition computed at CISD level has value of 280.08 eV therefore a shift of 0.92 eV was applied to the CIS spectrum. Unlike what we saw before for CH^+ and CH_2^+ , the spectrum presents two peaks at 280.08 eV and 293.28 eV with comparable photoabsorption cross section. The former corresponds to the transition towards the $1a_2'$ molecular orbitals while for the second one the assignment of the electronic character was not possible since the CI state presents a strong CSF mixing.

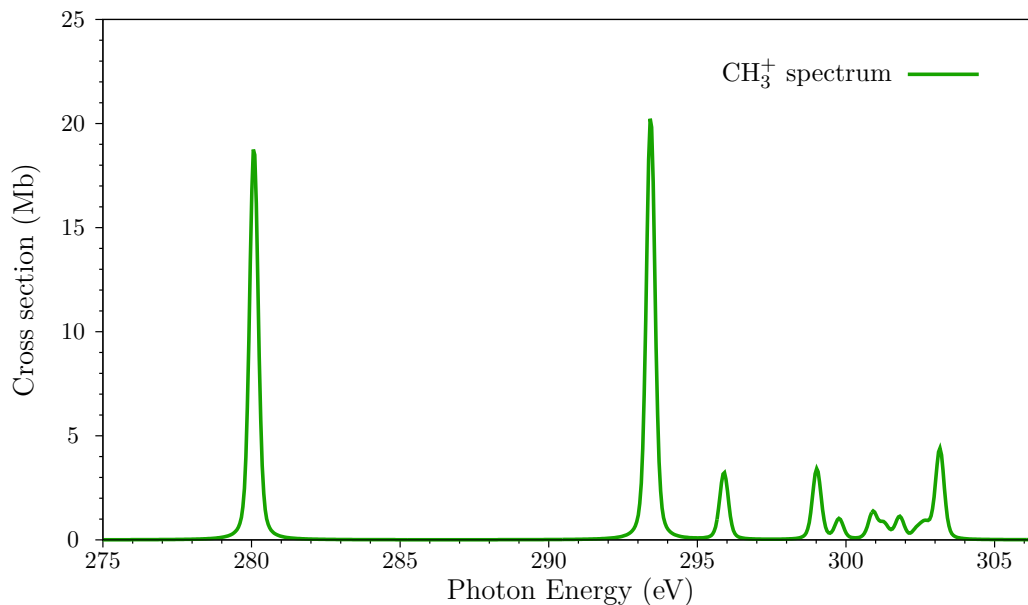


Figure 5.11: CH_3^+ computed X-ray photoabsorption spectrum.

5.3 Calculation of the photoabsorption spectra of OH_n^+

OH^+

Conversely to CH^+ , OH^+ in the ground state is a triplet spin system ($^3\Sigma^-$) and its electronic configuration is $(1s\sigma)^2 (2s\sigma)^2 (2\sigma)^2 (1\pi)^1 (2\pi)^1$. The ground ($^3\Sigma^-$) - metastable ($^1\Delta$) energy gap was computed first at the DFT/B3LYP level and it has the value of 2.91 eV. For this system, the energy gap, measured through the photoelectron spectrum [98] is 2.19 eV.

The computed ground state equilibrium internuclear distance is 1.024 Å which agrees well with the experimental value (1.029 Å [95]). Its K-shell ionization potential is found at 555.9 eV. Geometries and K-shell IPs for the OH_n^+ ($n=1,2,3$) molecular ions are summarized in Table 5.5.

In Figure 5.12 is reported the comparison between the absorption spectra computed at CIS level with and without nuclear dynamics. The spectra were shifted by 1.68 eV according to the first transition energy value computed at CISD level ($E_{1s \rightarrow 1\pi CISD} = 527.44$ eV). Unlike CH^+ , the main peak corresponds to the $1s \rightarrow 1\pi$ transitions toward the singly occupied MOs and no vibrational progression is present. The higher transitions are toward Rydberg states.

In particular, the core-excited transitions at 543.3 and 546.4 eV involve states with dissociative character since the peaks spread over 8 eV.

	Bond distance O—H (Å) (exp)	$\theta_{H_2-O-H_1}$ (exp)	IP (eV)
${}^3\text{OH}^+$	1.025 ^a (1.029)	—	555.9
${}^2\text{OH}_2^+$	1.0048 ^b	109.8 ^b	555.1
${}^1\text{OH}_3^+$	0.9793 ^c (0.976)	112.9 ^a (111.3)	551.8

a data from Ref. [99]
b experimental data not available
c data from Ref. [100]

Table 5.5: Geometries and K-shell edge ionization potentials for OH_n^+ ($n=1,2,3$) molecular ions.

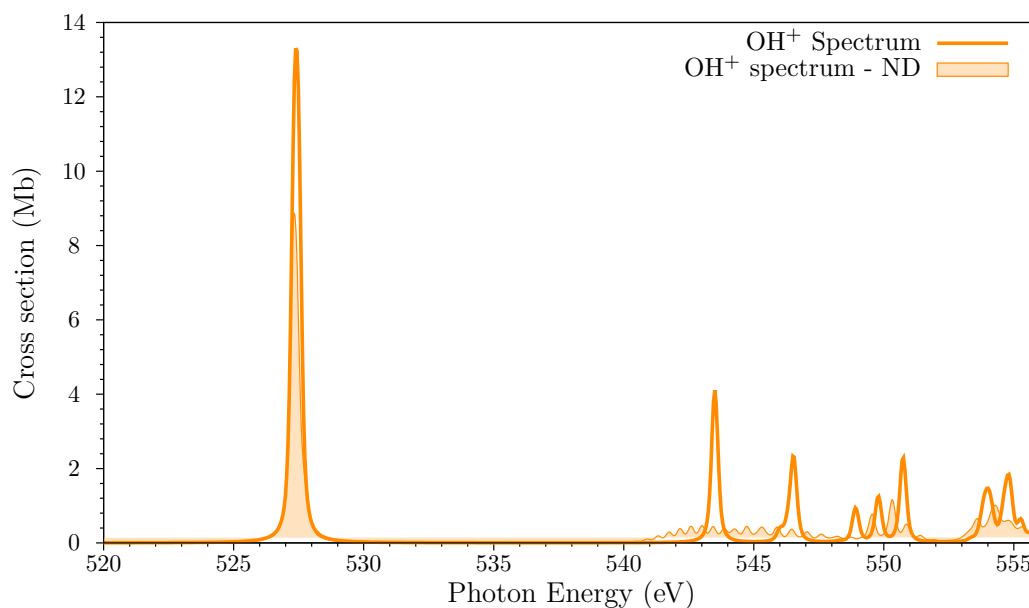


Figure 5.12: OH^+ computed spectrum, comparison between the vertical and nuclear wavepacket results respectively in full line and filled curve.

The results from the nuclear wavepacket propagation were then compared with the experimental ones as reported in Fig. 5.13. The fit of the population suggests that for this system the molecular ions are in the ground state. This ratio was recovered shifting the computed spectrum of 2.7 eV respect to the CIS vertical transition. The lack of vibrational progression of

the $1s \rightarrow 2p\pi$ transition as well as the broad peak around 545 eV are seen in the experimental data. Fig. 5.13 shows a very good agreement between the computed and experimental data.

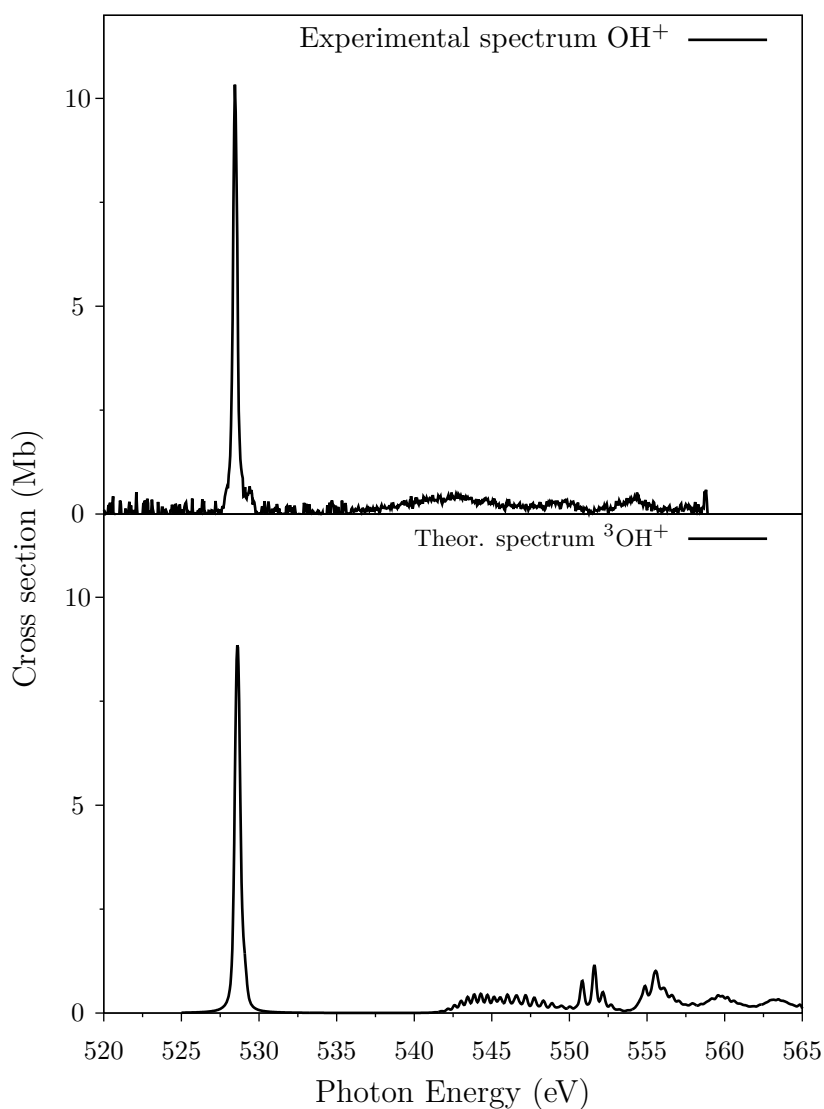


Figure 5.13: Comparison between the theoretical (bottom) and experimental (top) spectrum of OH^+ .

OH_2^+

Similarly to CH_2^+ , the diprotonated oxygen molecular ion OH_2^+ possesses C_{2v} symmetry with electronic configuration $1a_1^2 2a_1^2 1b_1^2 3a_1^2 2b_1^1$. Its K-shell IP is computed to be 555.1 eV (Table

5.5).

In Fig. 5.15 is reported the computed spectrum for OH_2^+ , the spectrum is shifted by 1.65 eV with respect to the transition computed at CISD level ($E_{CISD1s \rightarrow 2b_1} = 525.42$) The main peak at 525.42 eV corresponds at the transition towards the singly occupied MOs (Fig. 5.14). Compared to OH^+ and CH_2^+ , the OH_2^+ computed spectrum presents more transitions in the region above 535 eV. Transitions through the $3b_1$ and $4a_1$ molecular orbitals characterize the family of peaks between 538 and 544 eV. Transition in higher photon energy are toward Rydberg states.

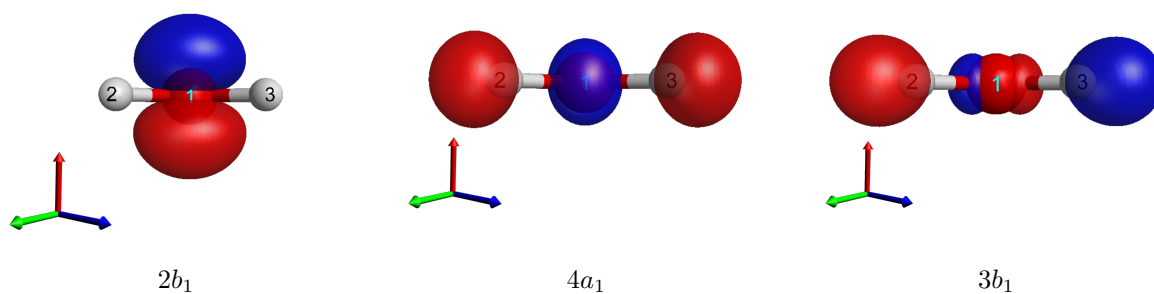


Figure 5.14: OH_2^+ molecular orbitals involved in the electronic transition.

OH_3^+

In its ground state, the hydronium cation OH_3^+ belongs to the C_{3v} point group with electronic configuration $1a_1^2 2a_1^2 1e^4 3a_1^2$. The oxygen K-shell IP is computed to be 551.8 eV. Conversely to what observed before, the addition of the H leads to a lowering of 3.3 eV of the 1s shell IP.

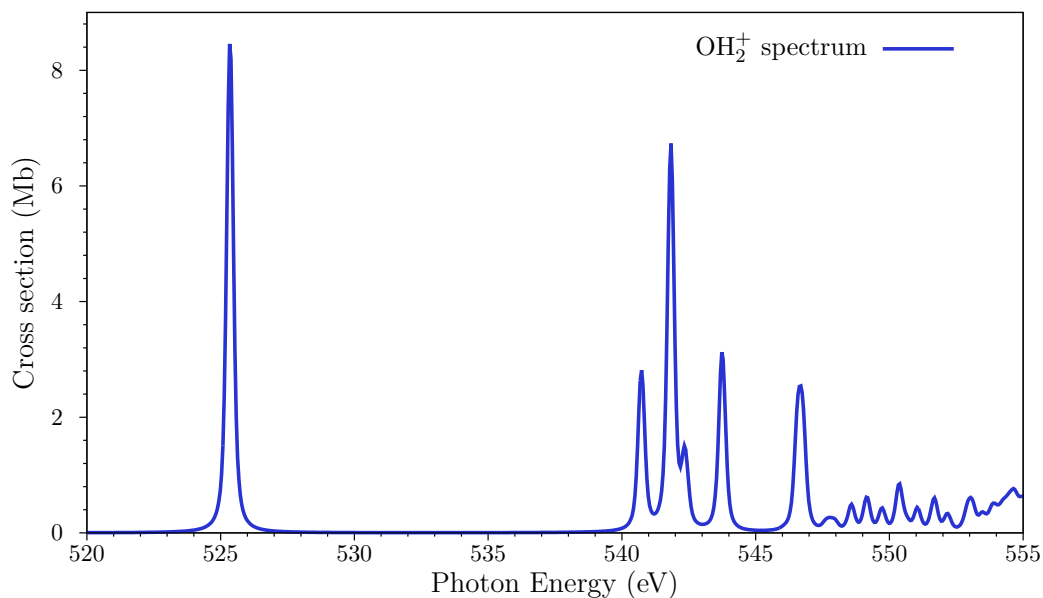


Figure 5.15: OH_2^+ computed X-ray photoabsorption spectrum.

The computed spectrum (Fig. 5.17) was shifted of 1.41 eV with respect the computed transition at CISD level ($E_{CISD1s \rightarrow 4a_1} = 533.74$ eV)

As can be seen from pictures Fig. 5.17, the OH_3^+ has significantly different features. The energy difference between the first peak and the IP (also named *term value*) is sensitive lower than OH^+ and OH_2^+ . It goes from 28.5 and 29.7 eV for OH^+ and OH_2^+ , respectively, to 18.1 eV for OH_3^+ . Furthermore, the first transition have very low intensity.

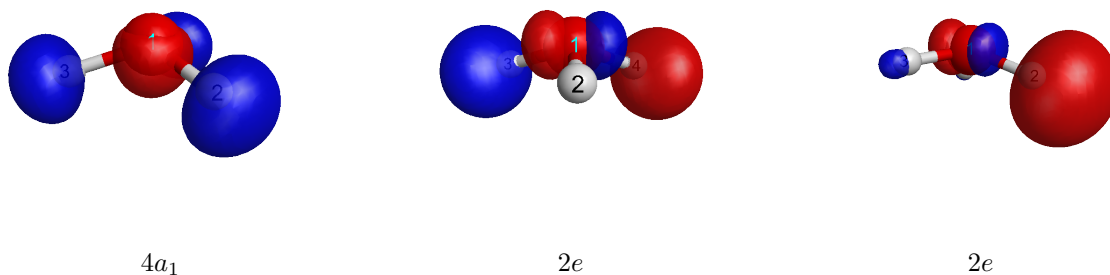


Figure 5.16: OH_3^+ molecular orbitals involved in the electronic transition.

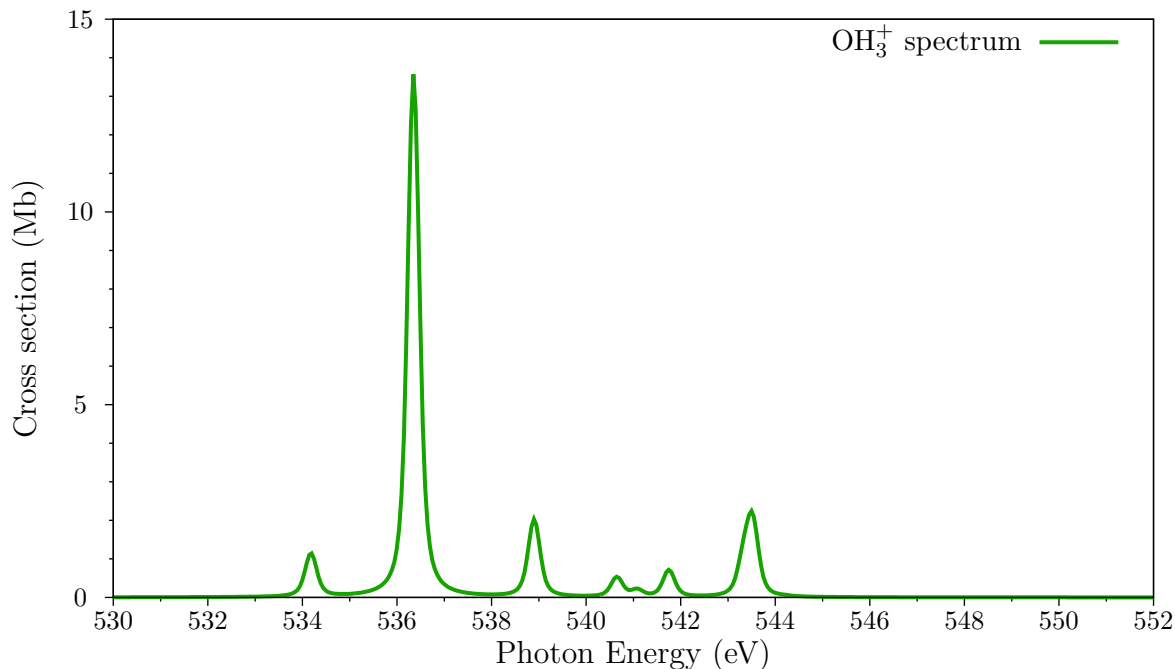


Figure 5.17: OH_3^+ X-ray photoabsorption spectrum.

The change in the trend can be explained looking at the MOs characteristics, in the previous cases the first transition involves MOs which have a contribution from the $2p$ orbitals of the excited atom. Conversely in this last case the $2p$ orbitals are filled by the bonding electrons and the empty MOs are placed at higher energy.

The above discussed data of XH_n^+ ($X = C, O$; $n=2,3$) molecular ions show that all the systems present a very well defined spectrum with photoabsorption cross sections higher than 10 Mb. Then the hypothesis of the negligible dipole moment transitions for this system is discarded and the fragmentation pathways for these molecular ions have to be investigated. Such studies are under progress.

6 | X-ray absorption spectra of SiH_n^+ molecular ions

In this Chapter are reported and discussed the results of the calibration and application of the protocol for the calculations of X-ray photoabsorption spectra on the L-edge of silicon molecular ions. As introduced in Chapter 4, we used SiH^+ as case study. The protocol was then applied to SiH_2^+ and SiH_3^+ .

The first Section is dedicated to SiH^+ molecular ion. First, the ground state properties are presented. The choice of spin-orbit coupling operator and the active space are then discussed. The Section continues with the discussion of the nuclear dynamics results by comparison of the results from the nuclear wavepacket propagation and linear coupling model. It ends with the comparison with the experimental results.

In Section 6.2 and 6.3, the SiH_2^+ and SiH_3^+ results are reported within the same framework of the first Section.

In Section 6.4, the Infrared spectroscopy (IR) is proposed as diagnostic method to probe the production of metastable states of SiH_2^+ and SiH_3^+ in the ECRIS source.

6.1 SiH^+

SiH^+ in the ground state has $(1s\sigma)^2(2s\sigma)^2(2p\pi)^4(2p\sigma)^2(4\sigma)^2(5\sigma)^2$ electronic configuration and it is termed $^1\Sigma^+$. The bond distance is computed to be 1.514 Å which is in good agreement with the experimental data (1.504 Å[95]). The bond distance for the metastable state was computed to be 1.5469 Å, slightly greater than in the ground state.

The ionization threshold for the 2p shell is 119.5 eV, the calculations were carried out neglecting spin orbit coupling effects. The L-shell IP is the same for the valence excited state.

The energy gap between SiH^+ and its valence excited state, $^3\text{SiH}^+$, computed at the DFT/B3-LYP level is 2.29 eV (Fig. 6.9).

6.1.1 Spin Orbit Coupling operator

As presented by the previous Chapter, the relaxation effects upon core-excitation are taken into account optimizing the spin orbitals for the first triplet core-excited state within a ROHF procedure. In the case of the 2p excitation, fixing the occupancy of one of the $2p_{x,y,z}$ orbitals to one, leads to a preferential direction. To avoid it, we performed the optimization in the 2s shell which is close in energy to the 2p shell.

For all the calculations, the active space was restricted from 220 to 100 MOs which corresponds to discard the spin-orbitals with energy above 154 eV, slightly higher than the L-shell IP.

As previously introduced, we computed the spectra using the one-electron $1e$, two-electrons $2e$ and partial two-electrons $2ep$ method. For each of them, we studied the effect of the inclusion of the valence excitations. The 1s and 2s orbitals are always inactive (or *frozen*) while the 2p electrons are always active. In the following, we applied a labelling according to the number of valence MOs : $3/n_{val}/100$ where 3 and n_{val} indicate the number of active 2p and valence orbitals, respectively and 100 represents the number of orbitals in the active space. A general picture is presented in Fig. 6.1.

In Table 6.1 are reported the energy values of transition computed for the different SOC operators and active spaces. From these data, it is possible observe that for a given number of excited electrons the excitation energy at CIS level is nearly the same for all three SOC operators. For example, for the calculation with the 3/2/100 active space the energy change of 0.03 eV going from the $1e$ to the $2e$ operator.

In Figure 6.2 are reported the spectra for the different type SOC operator and active space. On the top panel, it is possible to observe that, going from 3/2/100 to 3/0/100 active space even if the number of active electrons is increased the features of the spectra do not undergo any changes. Therefore, when the of the valence excitation are included the $\hat{H}_{act-act}^{1e}$ operator compensates the \hat{H}^{2e} terms.



Figure 6.1: Scheme of active orbitals in the calibration of L-shell protocol

SOC operator	Frozen Orbitals	Energy CIS (eV)
	3/2/100	97.62
1e	3/1/100	97.35
	3/0/100	98.08
2ep	3/2/100	97.64
	3/1/100	97.38
	3/0/100	98.10
2e	3/2/100	97.65
	3/1/100	97.40
	3/0/100	98.16

Table 6.1: Values of the first excitation energy ($1s \rightarrow 1\pi^*$) computed at CIS level with the one-electron $1e$, two-electrons $2e$ and partial two-electrons $2ep$ operators and CISD level without spin-orbit coupling.

This compensation is lost when the valence orbitals are inactive and, as we can see from the bottom panel in Fig 6.2, the spectra computed within the different SOC operator present different profiles. This can be associated to the fact that when the active electrons decrease the \hat{H}^{2e} terms became more important.

The results show that including all the valence excitations in the calculations, we can

reliably use only the $1e$ term in the calculation of the XAS spectra.

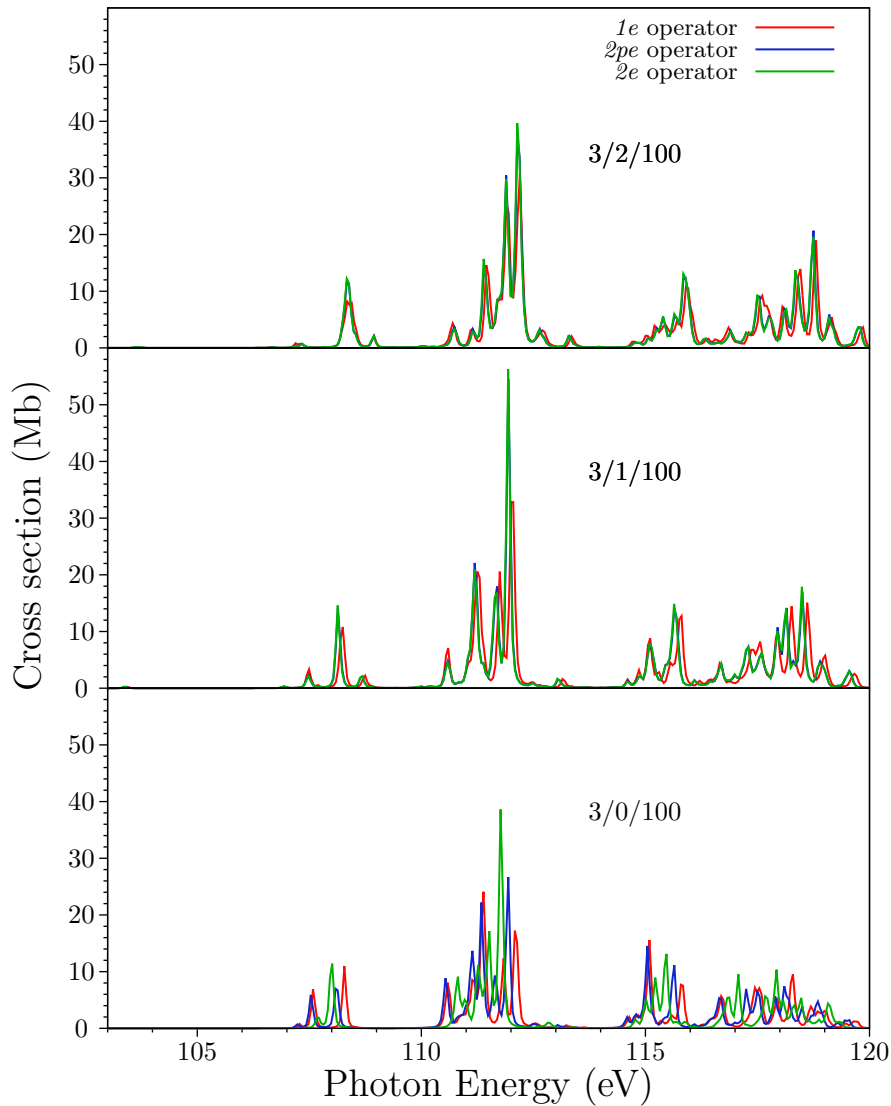


Figure 6.2: Simulated spectra for the different SOC methods: $1e$ (red line), $2e$ (blue line) and $2pe$ (green line) with different number of excited electrons. In bottom panel are reported the spectra computed exciting only $2p$ electrons, in the middle and top panels are reported the spectra computed allowing the excitation of the excitation from one and two valence orbitals, respectively

Furthermore, we analysed the CPU-time for the spin-orbit coupling calculations with the different terms. In Fig. 6.3 is reported the time (in hour) for the different SOC method and

active space. The calculations carried out using the full Breit-Pauli operator are the most time expensive ones. As we can see from Fig. 6.3, within the 3/2/100 active space the calculations for a single point using the $2e$ method is 16 times longer than the $1e$ method. Since the 3/2/100 active space provides results independent from the chosen spin-orbit operators, we decided to perform the calculations using this active space and the one-electron term for all the systems.

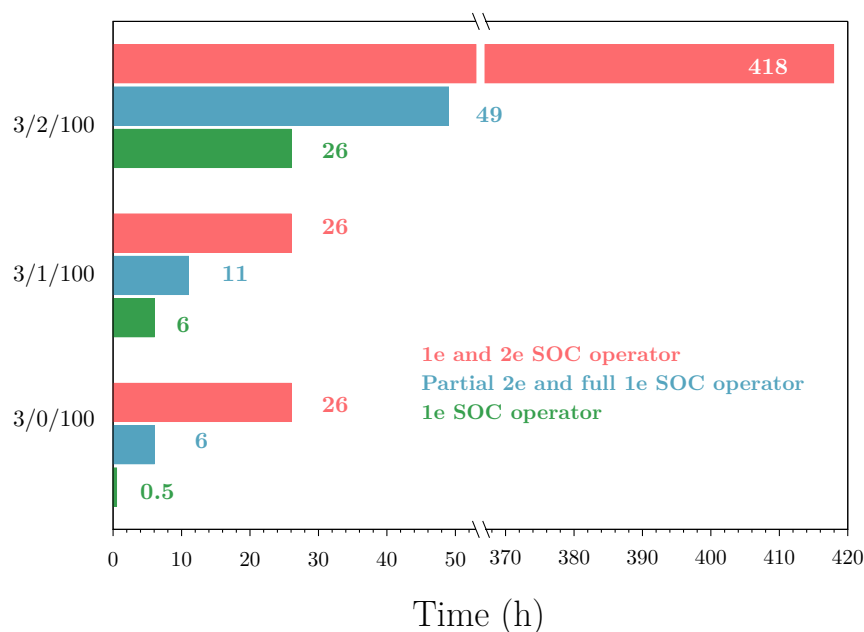


Figure 6.3: CPU-time for the SOC calculations. In red and blue are reported, respectively, the time for the calculations with complete Breit-Pauli operator and the partial 2e and full 1e operator. The time consuming for the calculations with the mono-electronic SOC operator is shown in green.

6.1.2 Electronic transitions analysis

The analysis of the electronic transitions for the L-shell excited systems is more complicated due to the high number of transitions upon spin-orbit interaction. In the simplest case, SiH^+ in its ground state, the electronic transitions arising from the spin-orbit-coupling interaction are around 1900, this scenario makes a detailed analysis not feasible. In order to identify the electronic characteristics of each region, we compared the spectra with and without spin-orbit coupling (Fig. B.1a in Appendix B) and then for each family of peaks we analysed the electronic

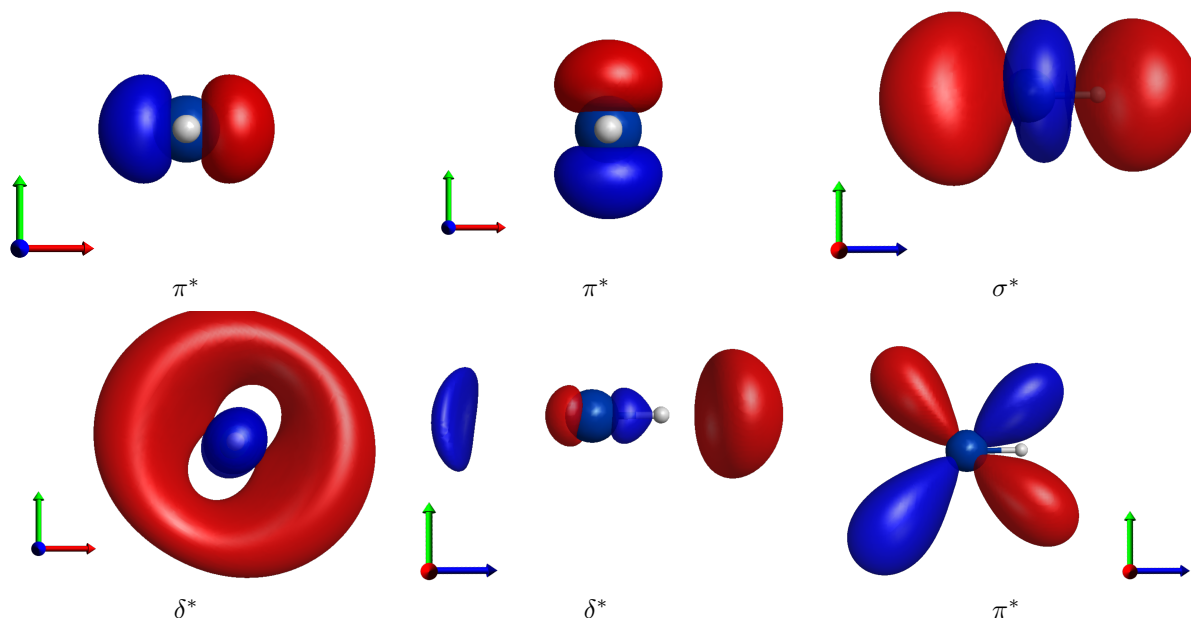


Figure 6.4: Molecular orbitals involved in the electronic transitions of SiH^+

structure of the most intense transitions without SOC. The same treatment has been done for the spectrum of the metastable state.

In the ground state SiH^+ , the first transitions occur toward the $1-2\pi^*$, Fig. 6.4a and 6.4b, in the region at 99-104 eV. These transitions exhibit really low cross sections (below 0.02 Mb). In the region between 105 and 109 eV, the transitions $2p^{-1} \rightarrow \sigma^*$ take place (Fig. 6.4c). The family of very intense peaks at 109-113 eV corresponds to states with $n\delta^*$ and $n\pi^*$ characters (Fig. 6.4d, 6.4e and 6.4f). Rydberg states are implicated in the region above 113 eV.

For $^3\text{SiH}^+$, the first transitions towards the singly occupied MO having π character occur below 98 eV. The spectrum above 98 eV presents the same electronic characteristics of the aforementioned ground state.

6.1.3 Nuclear dynamic simulation

As introduced in Chapter 4, the core-excited state nuclear dynamics of the $2p$ -excited system was carried out using the nuclear wavepacket propagation and the linear coupling model (LCM).

Furthermore, we used the HA to approximate the PESs because the long CPU-time of the SOC calculations. We computed three points around the equilibrium geometry using 3/2/100

	Region	FWHM (eV)		Region	FWHM (eV)
$^1\text{SiH}^+$	I	< 102 eV	$^3\text{SiH}^+$	I	< 99.0 eV
	II	102 - 108.2 eV		II	99.0 - 104.0 eV
	III	> 108.2 eV		III	104.0 - 108.0 eV
		IV		> 108.0 eV	

Table 6.2: Full width at half maximum (FWHM) in eV for the different region of ground and metastable states of SiH^+ , respectively $^1\text{SiH}^+$ and $^3\text{SiH}^+$.

active space and one-electron spin-orbit coupling operator. The nuclear wavepacket was performed using a core hole lifetime of 45 meV.

For the linear coupling model, the vertical spectrum without SOC was divided in three regions according the involved electronic transitions. The gradient was computed for representative core-excited states, *i.e.* those with higher photoabsorption cross section. In Table 6.2 are reported the FWHM of the Gaussian broadening (Eq. 2.4.12) used in the simulation of the spectrum. More details about the complete procedure can be found in Appendix B.

In Fig. 6.5 is shown the comparison between the vertical spectra computed with the LCM and the nuclear wavepacket propagation. The region strongly affected by the dynamics is the one located around 107 eV due to the dissociative character of these states. The LCM predicts for these transitions a Gaussian broadening with FWHM of 1.28 eV which reproduces well the broadening obtained with the nuclear wavepacket simulation. Moreover, the last method shows that the peaks between 108 and 112 eV undergo only small changes in the photoabsorption cross sections.

The same treatment was carried out for the metastable state spectrum. According to the transitions features, the spectrum was divided in four regions as reported in Table 6.2. Only the Region III presented a large vibrational distribution and a Gaussian broadening of 2.11 eV was used in the simulation. The comparison between the spectra computed within the vertical approximation, LCM and nuclear wavepacket propagation is reported in Fig 6.6. The LCM is able to reproduce well the broadening over 2 eV in Region III. In Regions I and III, the nuclear wavepacket propagation leads to a larger FC distribution which makes the peaks in those regions broader and less intense.

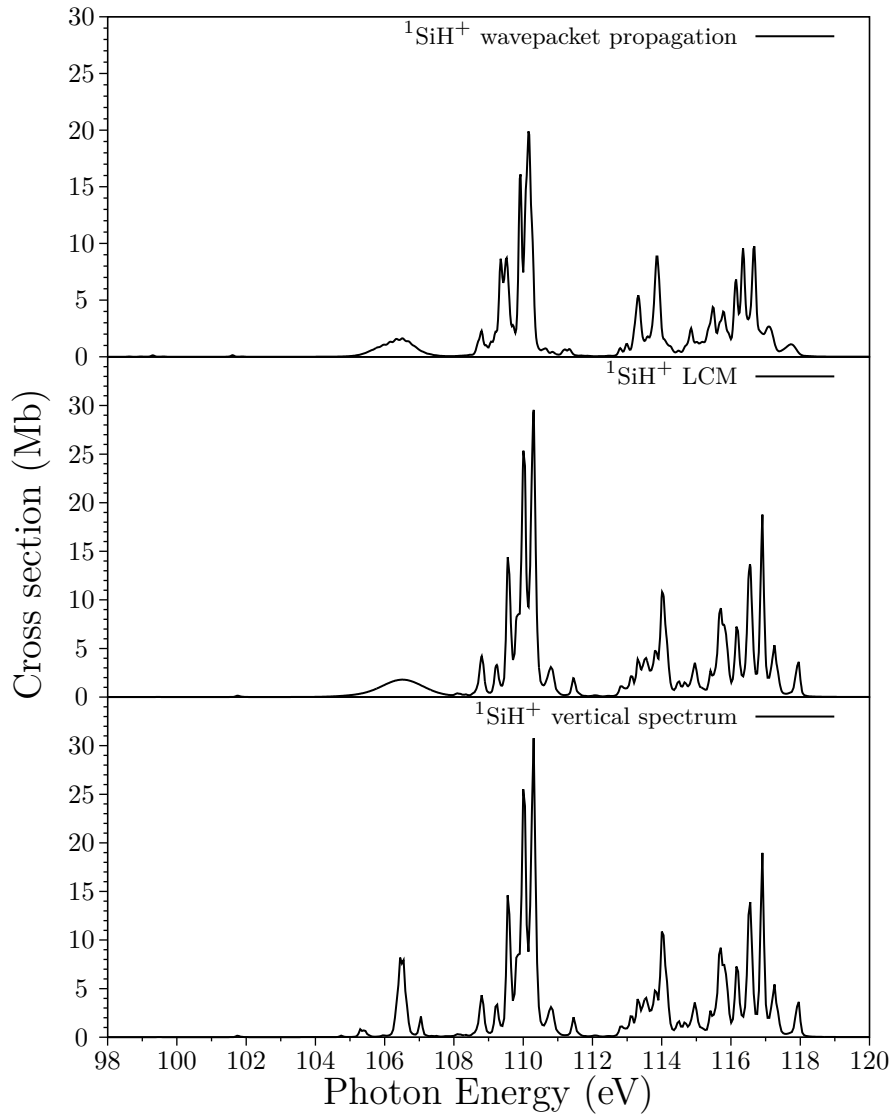


Figure 6.5: Spectra computed with vertical approximation (bottom), linear coupling model (middle) and nuclear wavepacket propagation (top) approaches for ground state SiH^+ molecular ion.

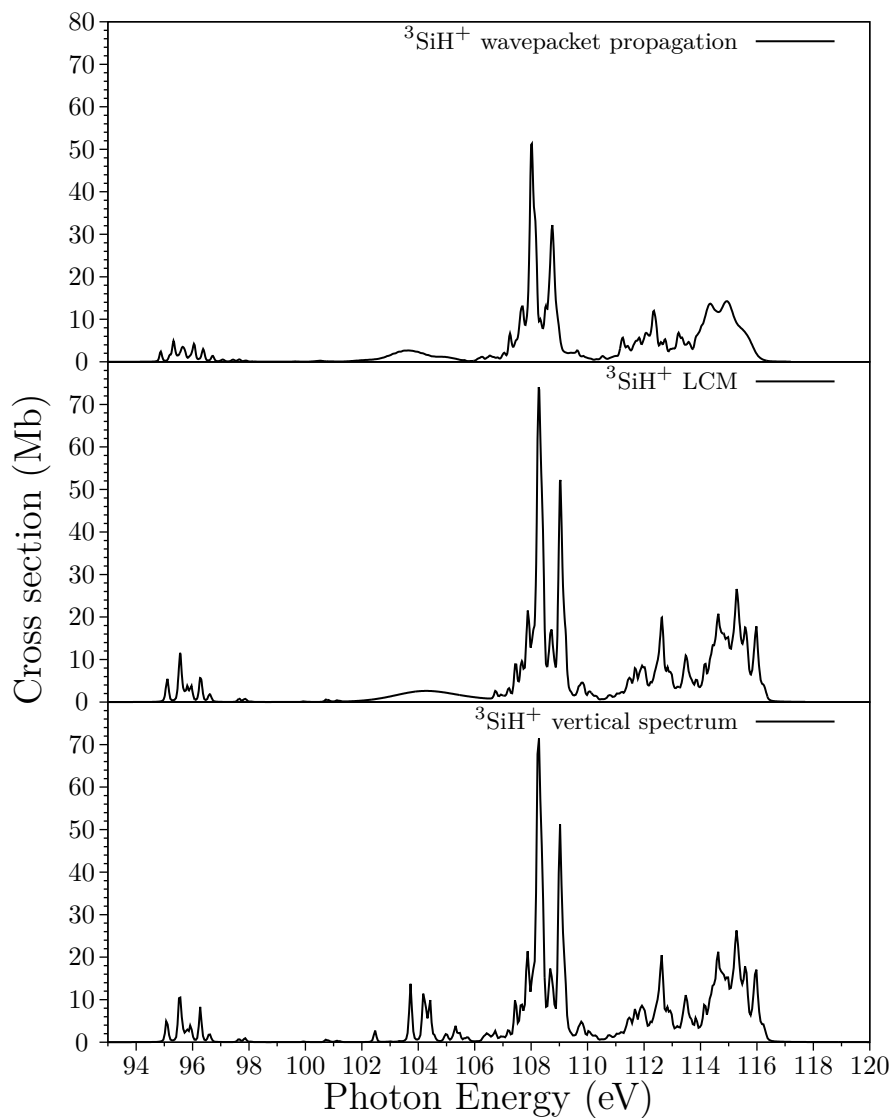


Figure 6.6: Spectra computed with vertical approximation (bottom), linear coupling model (middle) and nuclear wavepacket propagation (top) approaches for metastable state SiH^+ molecular ion.

6.1.4 Comparison with experimental data

The comparison with the experimental data was performed using both the results from the LCM and the nuclear wavepacket propagation.

The results from the nuclear wavepacket propagation are compared with the experimental

data in Fig. 6.7. The spectrum was obtained from the fitting procedure which suggest that 56% of the ground state and the 44% of the metastable state contribute to the spectrum. A global shift of 2.5 eV was applied to the spectrum computed at CIS level.

The comparison permits to assign the electronic structure and contributions in the experimental spectrum. In the region below 100 eV, the experimental data presents a cross section lower than 1 Mb and the theoretical data overestimate the cross section in this region. Only the metastable state contribute to this part of the spectrum. In the rest of the spectrum, the contributions from $^1\text{SiH}^+$ and $^3\text{SiH}^+$ are comparable. The family of peak between 109 and 114 eV has a structure formed by two main peaks having maximum at 111.0 and 112.4 eV which can be attributed to the triplet and singlet states, respectively.

The simulations of the experimental spectrum from the LCM and nuclear wavepacket calculations are compared in Fig. 6.8. The LCM was shifted in order to have a direct comparison with the last one. The LCM method overestimates the region below 100 eV of a factor of 2. The peaks distribution in the $n\delta^* - n\pi^*$ region (108 - 112 eV) is not well reproduced. Because within the LCM method only few representative states were considered, the width of the peaks is underestimated. The fit procedure on the results from the LCM indicates a contribution of the 66% from the ground state and of 34% from the valence excited state. The spectrum was shifted of 2.0 eV. The electronic structure of the spectrum is the same as discussed before.

Furthermore, the $^1\text{SiH}^+ / ^3\text{SiH}^+$ distribution computed within the LCM method differs slightly from the one computed with the nuclear wavepacket propagation method. Nevertheless its simplicity permits to adopt it to probe the dynamics for bigger systems where the computational cost spin-orbit interactions does not allow to perform the PESs calculation and the wavepacket propagation.

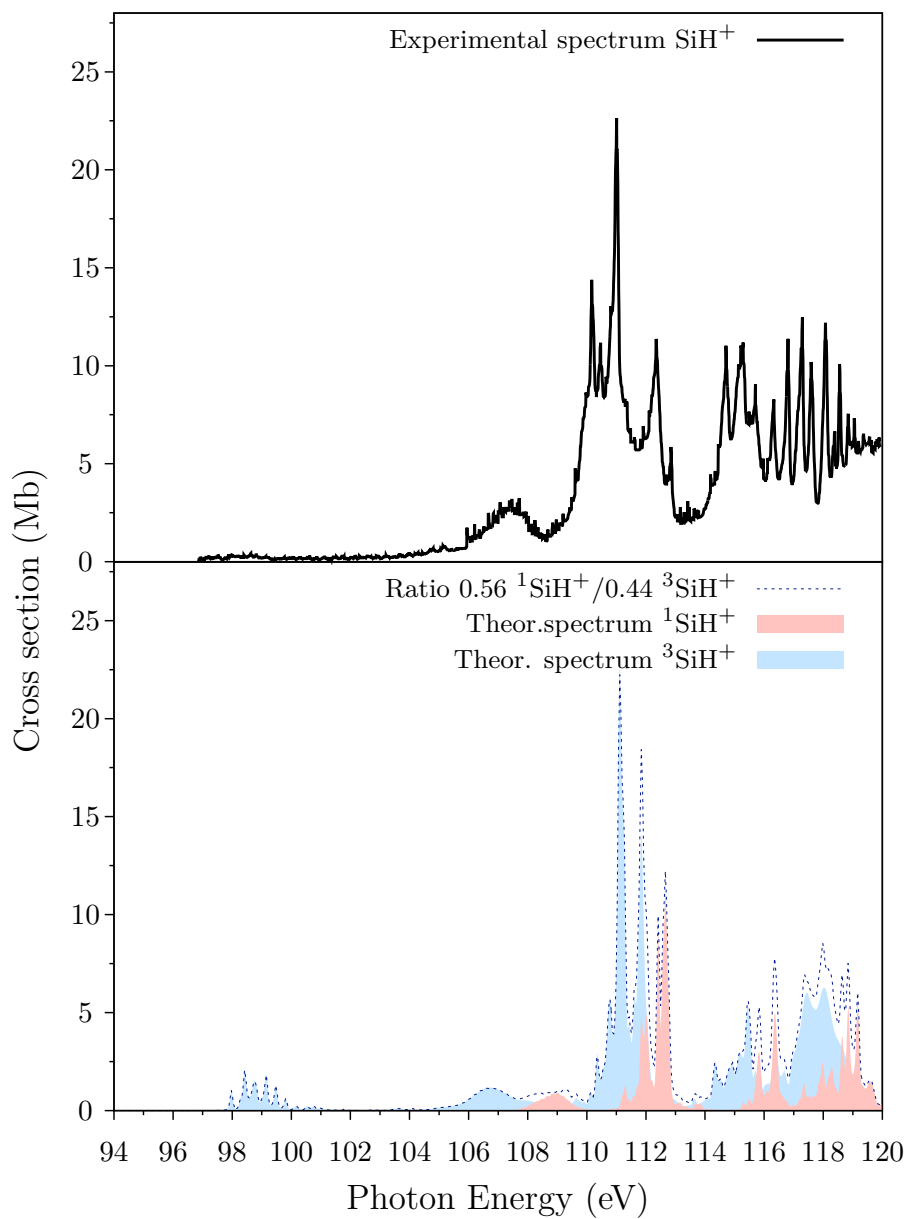


Figure 6.7: Experimental (top) and theoretical (bottom) spectra photoabsorption cross section for SiH^+ molecular ion

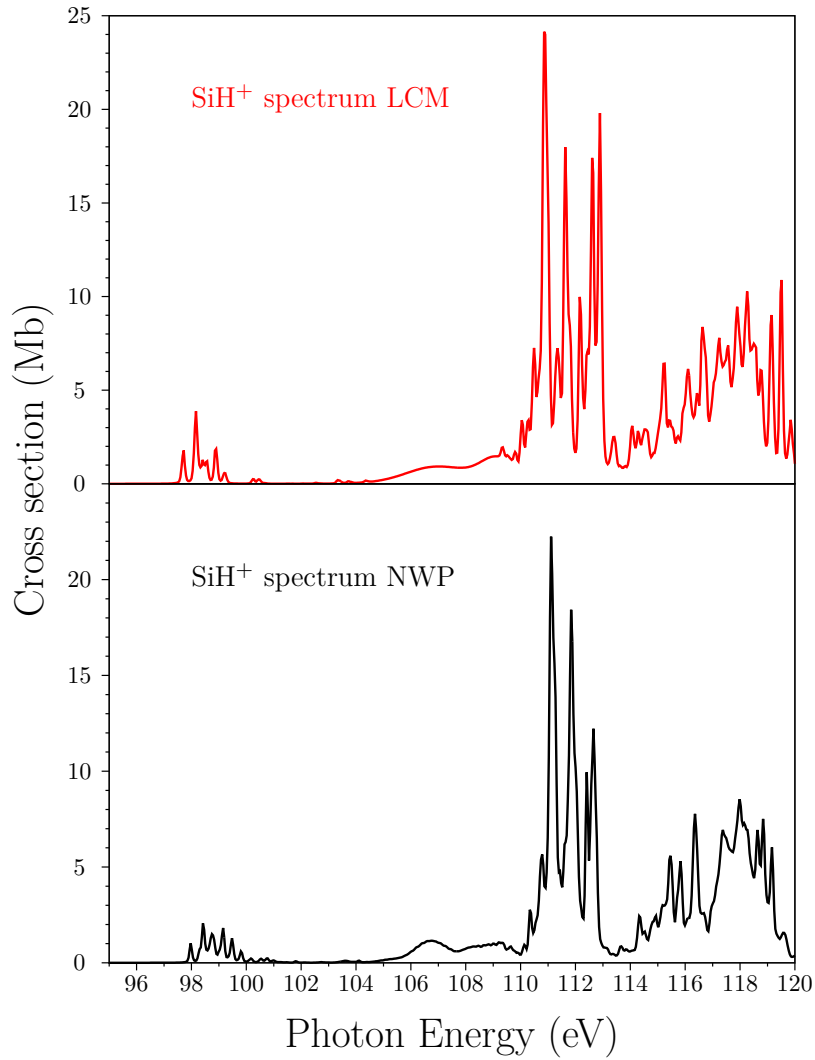


Figure 6.8: Photoabsorption cross section spectra computed with the nuclear wavepacket propagation (bottom) and linear coupling method (top) for SiH^+

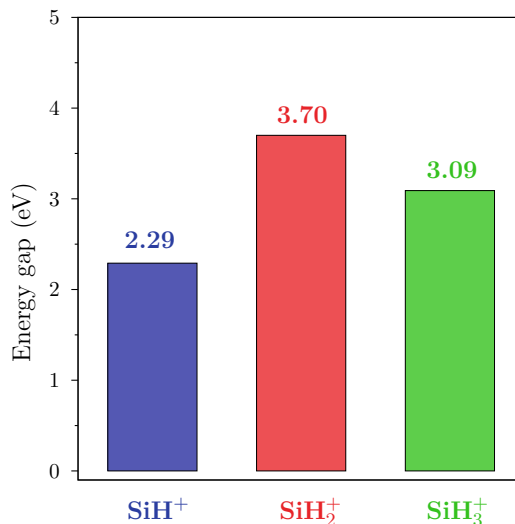


Figure 6.9: Ground state - metastable state energy gap for SiH_n^+ ($n=1, 2, 3$) molecular ions.

6.2 SiH_2^+

SiH_2^+ in the ground state has a doublet spin multiplicity with electronic configuration $1a_1^2 2a_1^2 1b_1^2 1b_2^2 3a_1^2 4a_1^2 2b_1^2 5a_1^1$ belonging to the C_{2v} point group, as shown in Figure 6.10. The geometry optimization indicates a very different geometry for the system in the ground and metastable state without changing in the point group. The $^2\text{SiH}_2^+ / ^4\text{SiH}_2^+$ energy gap is computed to be 3.7 eV. The bond distance in the ground and metastable states are, respectively, 1.4828 Å and 1.6043 Å. The valence excitation strongly affects the $H_2 - Si - H_3$ angle with a decreasing from 119.49° in the ground state to 69.02° in the metastable state. The geometries data are reported in Table 6.3. Experimental data about the geometries are not available for SiH_2^+ .

	ΔE (eV)	Bond distance Si-H (Å)	$\theta_{H_2-Si-H_3}$	Ionization Potential (eV)
$^2\text{SiH}_2^+$	3.7	1.48275	119.49	116.8
$^4\text{SiH}_2^+$		1.6043	69.02	115.9

Table 6.3: Geometry data for the ground state and the metastable state of SiH_2^+ molecular ion.

The bond distance and angle for SiH_2^+ were compared with the ones for the neutral silicon

dihydride, SiH_2 [101]. It has bond distance and $H_2 - \text{Si} - H_3$ angle of 1.514 Å and 92.0° , respectively. The removal of one electron leads to the enhancement of strength of the Si - H bond with a shorter bond length. On the contrary the $H_2 - \text{Si} - H_3$ angle is larger in the molecular ion.

The IP was computed for both systems neglecting the spin-orbit couplings, the values are 116.8 and 115.9 eV for ${}^2\text{SiH}_2^+$ and ${}^4\text{SiH}_2^+$, respectively (Table 6.3).

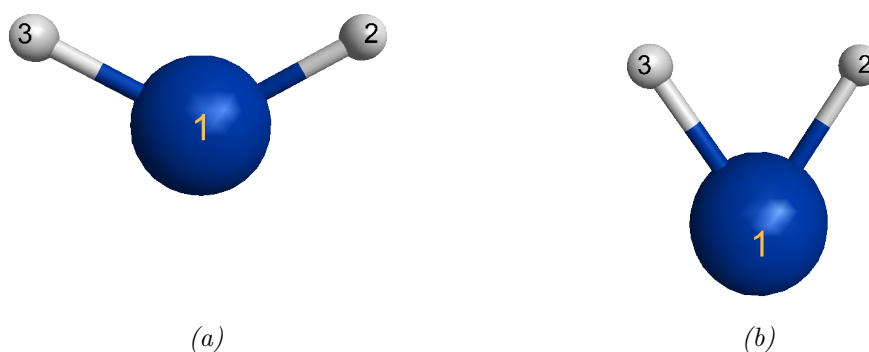


Figure 6.10: Geometry of ${}^2\text{SiH}_2^+$ (a) and ${}^4\text{SiH}_2^+$ (b).

The electronic transition analysis was performed on the vertical spectrum of ${}^2\text{SiH}_2^+$ and ${}^4\text{SiH}_2^+$. For the ground state system, the first region is located between 95 and 102 eV and is characterized by transitions toward the singly occupied MO. Two families of peaks are present between 102.0 and 107.0 eV which correspond to transitions toward a_1 orbitals (Fig. 6.11b and 6.11c). Next, transitions up to 112 eV involve a_2 and b_1 orbitals. The Rydberg transitions take place in the rest of the spectrum.

The metastable spectrum has five different regions characterized by transitions with the same nature of the ground state spectrum.

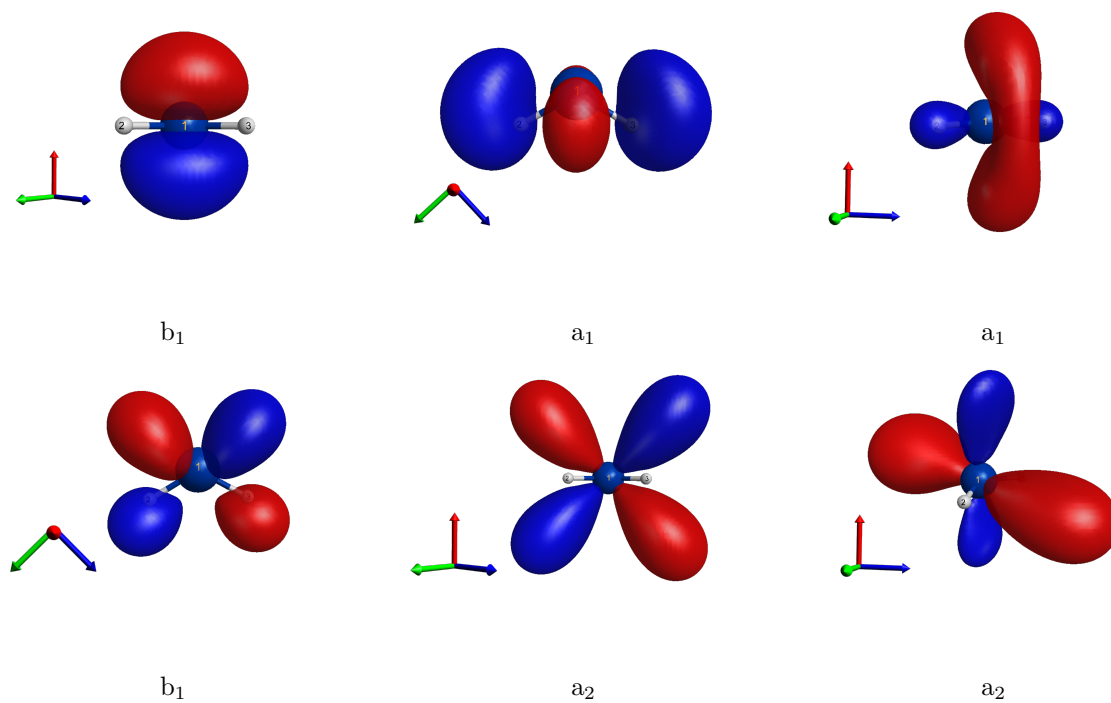


Figure 6.11: Molecular orbitals involved in the electronic transitions of SiH_2^+ ground state

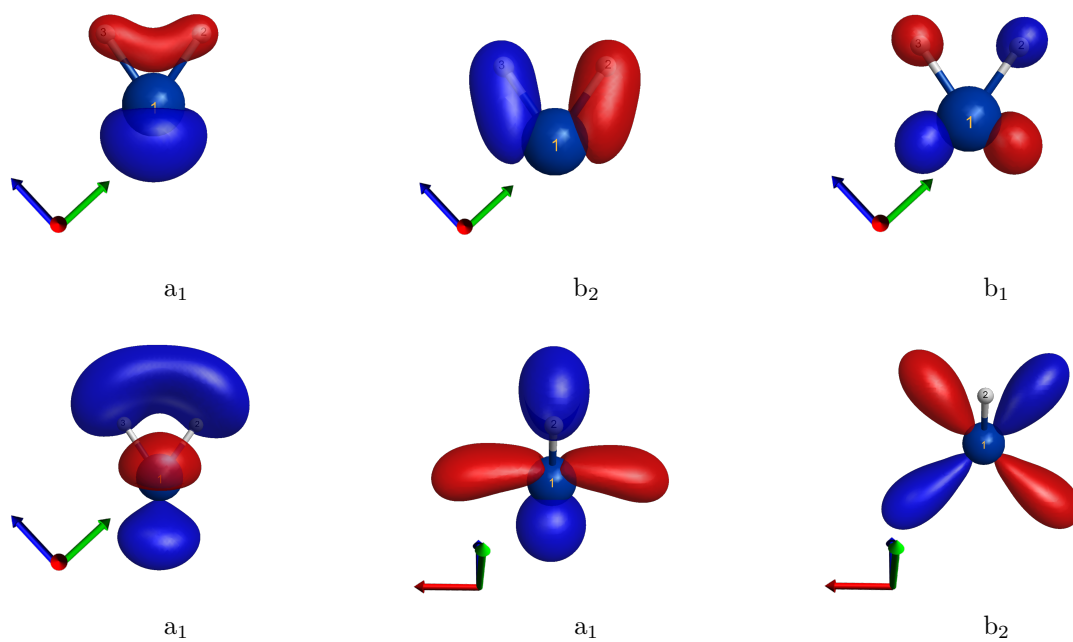


Figure 6.12: Molecular orbitals involved in the electronic transitions of SiH_2^+ metastable state

Region			FWHM (eV)	Region			FWHM (eV)
$^2\text{SiH}_4^+$	I	95.0 - 102.0 eV	1.58	$^4\text{SiH}_4^+$	I	95 - 100 eV	1.31
	II	102.0 - 105.5 eV	1.18		II	98.8 - 103.2 eV	0.9
	III	105.5 - 107 eV	1.58		III	103.2- 107.3 eV	2.93
	IV	107 - 120 eV	0.08		IV	107.3 - 120 eV	0.08

Table 6.4: Full width at half maximum (FWHM) in eV for the different region of ground and metastable states of SiH_2^+ , respectively $^2\text{SiH}_2^+$ and $^4\text{SiH}_2^+$.

As for SiH^+ , we identified the most intense peaks in the spectrum without SOC. These peaks are used as representative in the LCM for the entire region.

For the ground state molecular ion, the spectral regions above 107 eV were joined and the nuclear dynamics was not probed because the high number of transitions involved and the strong CSF mixing of many of them. The values of the Gaussian FWHM for both states are reported in Table 6.4.

In Fig. 6.13, the vertical spectrum of $^2\text{SiH}_2^+$ is compared with the one obtained with the LCM. The broadening in the Region I and III of $^2\text{SiH}_2^+$ is due to the activation of the bending vibrational mode while the symmetric stretching is activated in Region II.

The spectrum resulting from the LCM of $^4\text{SiH}_2^+$ is reported in Fig. 6.14. For the valence excited state, in Region I both the bending and symmetric stretching are activated. Conversely, in Region II the broadening is due to the asymmetric vibrational mode. The large vibrational progression in Region III is caused by the concerted activation of all three normal modes (details in Appendix B).

The spectra obtained from the LCM simulations were used for the comparison with the experimental data. The population fitting process suggests that the molecular ions are mainly in the ground state (85%). The weighted spectrum was shifted by 0.7 eV. The theoretical spectrum agrees well with the experimental one. The broadening regions at 98-102 and 103-107 eV are well reproduced but in the second one the photoabsorption cross section is overestimated.

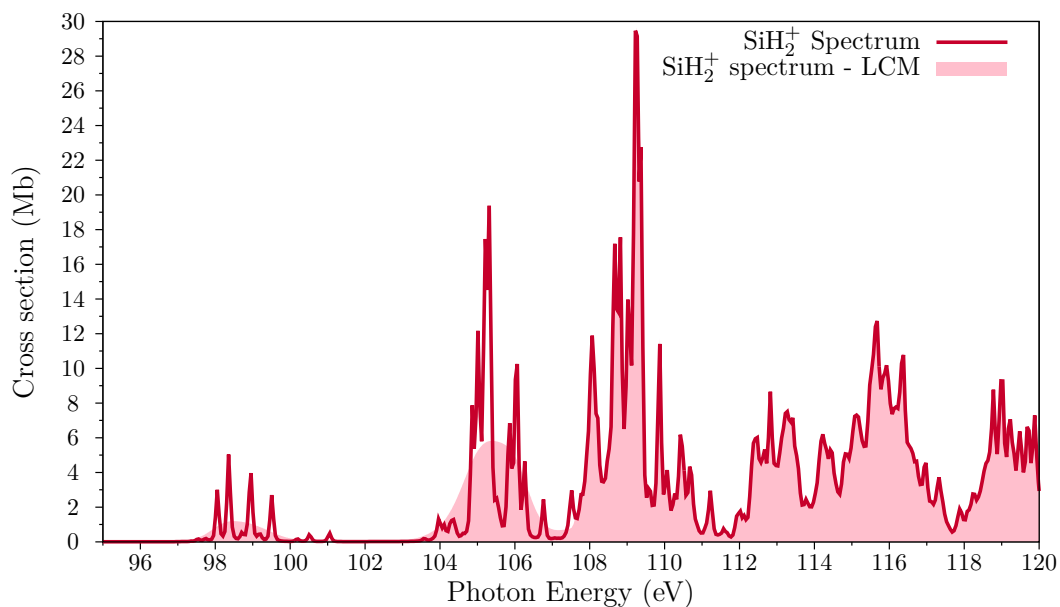


Figure 6.13: Comparison between the spectra computed within the vertical and linear coupling model for ${}^2\text{SiH}_2^+$

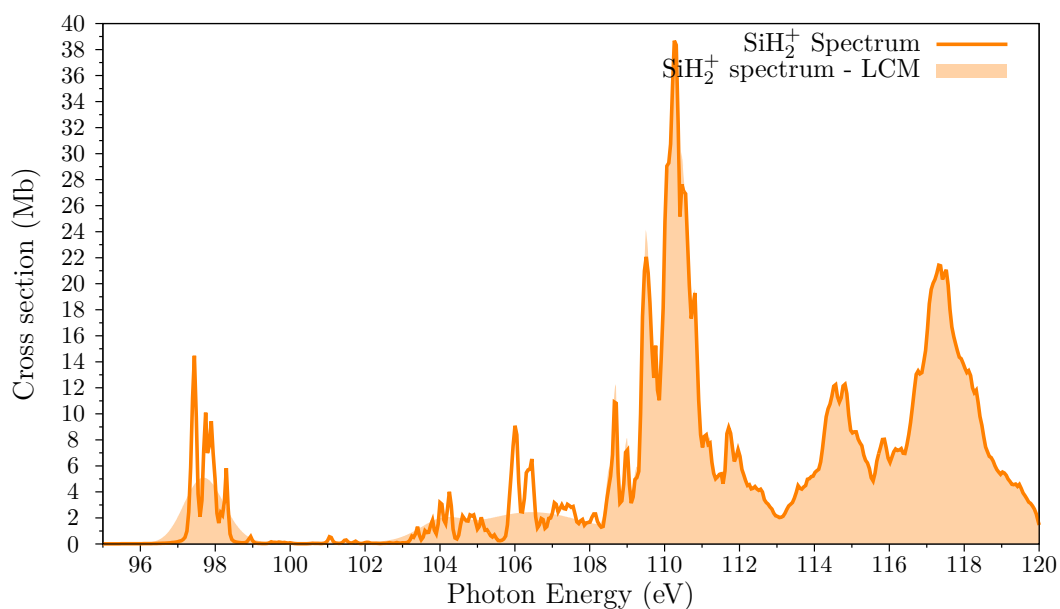


Figure 6.14: Comparison between the spectra computed within the vertical and linear coupling model for ${}^4\text{SiH}_2^+$

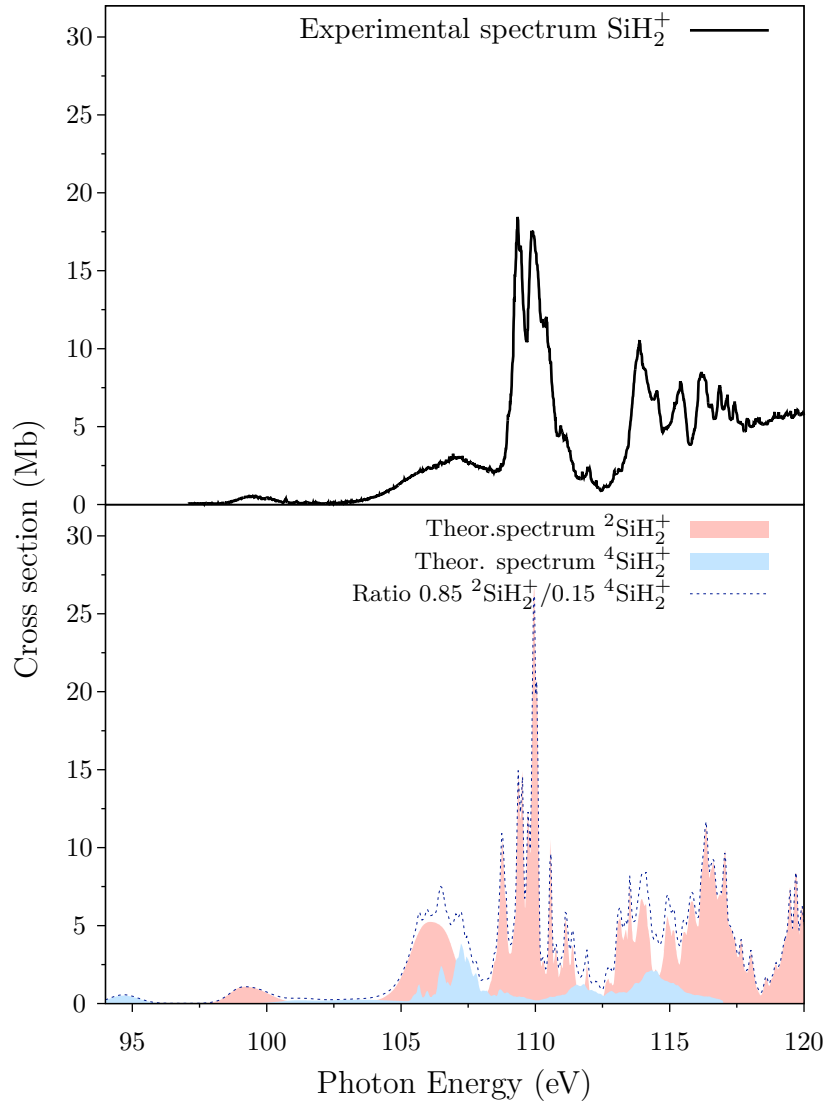


Figure 6.15: Experimental (top) and theoretical (bottom) spectra photoabsorption cross sections for SiH_2^+ molecular ion

As can be observed in Fig. 6.15, the experimental data were recorded starting from 97 eV, from our calculations we found that the metastable state exhibits transitions at lower energies then for this system the extension of the experimental set up to lower energies could provide a way to estimate the production of the metastable state and quantify the ground/metastable state ratio.

6.3 SiH_3^+

SiH_3^+ in the ground state has $1a_1'^2 2a_1'^2 1a_2'^2 1e'^4 3a_1'^2 2e'^4$ electronic configuration within the D_{3h} point group. The metastable state has C_s symmetry (Fig. 6.16) and it is triplet spin system. The energy gap between the $^1\text{SiH}_3^+$ and $^3\text{SiH}_3^+$ is 3.02 eV (Fig 6.9).

The geometries and relative data are reported in Figure 6.16 and Table 6.5, respectively. Geometries data are not available for SiH_3^+ but we compared the system with the neutral species SiH_3 [102]. The Si-H bond distance for the neutral and the ground state molecular ion are 1.468 Å and 1.467 Å, respectively. The angle between the H atoms is slightly changed being 110.5° and 120.0° for the silyl radical and cation, respectively. Unlike what seen for the other molecular ion, the removal of one electron does not affect the bond distance but the point group changes from C_{3v} to D_{3h} .

The L-shell thresholds computed without spin orbit coupling are 116.9 and 116.8 eV for the ground and metastable state, respectively.

	ΔE (eV)	Bond Distance(Å)		Angle		IP (eV)
		Si-H x ($x = 2, 4$)	Si-H $_3$	$\theta_{H_3-Si-H_x}$ ($x=2,4$)	$\theta_{H_2-Si-H_4}$	
$^1\text{SiH}_3^+$	3.02	1.467	1.467	120.0	120.0	116.9
$^3\text{SiH}_3^+$		1.713	1.490	105.4	20.0	116.8

Table 6.5: Geometry data for the ground state and the metastable state of SiH_3^+ molecular ion.

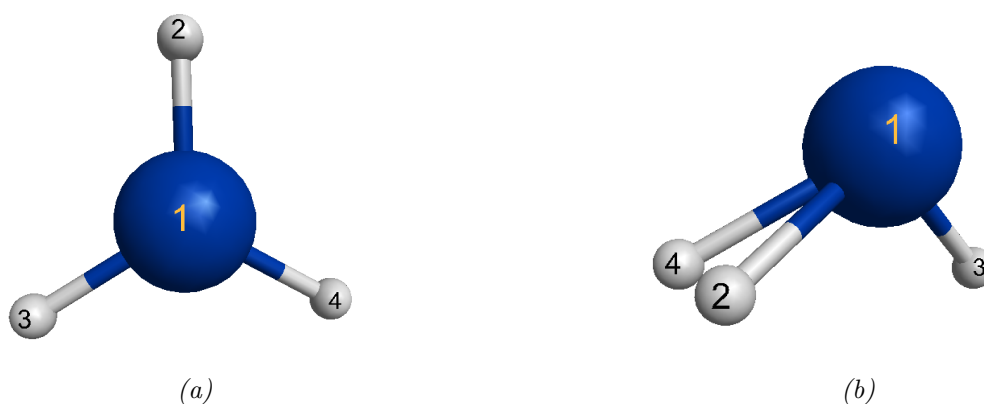


Figure 6.16: Geometry of $^1\text{SiH}_3^+$ (a) and $^3\text{SiH}_3^+$ (b).

The SiH_3^+ ground state spectrum is characterized by two regions, the first between 96.0 and 106.5 eV and the second one above 106.5 eV, characterized by transitions toward a'_1 (Fig. 6.17a) and e' orbitals, respectively (Fig. 6.17b - 6.17c).

For the $^3\text{SiH}_3^+$, the first region, below 98 eV, involves the singly occupied MOs (Fig. 6.18a). The photon energy up to 107 eV excite the 2p electron toward the a' and a'' MOs. Higher transition are difficult to identify because the strong CSFs mixing.

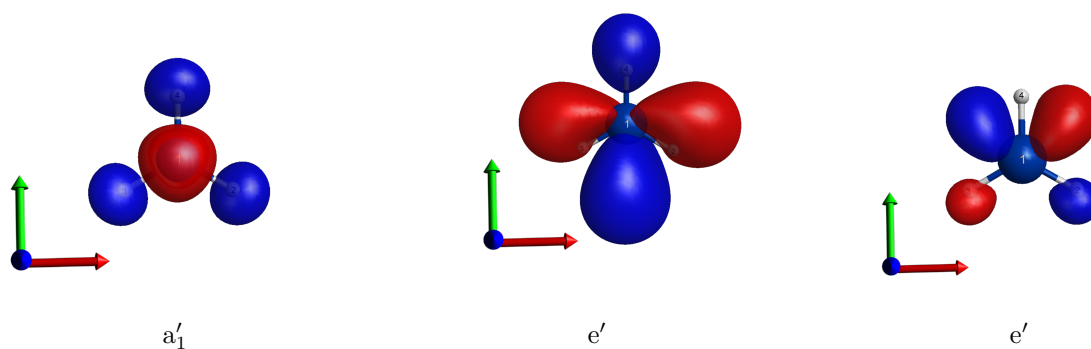


Figure 6.17: Molecular orbitals involved in the electronic transitions of SiH_3^+ ground state

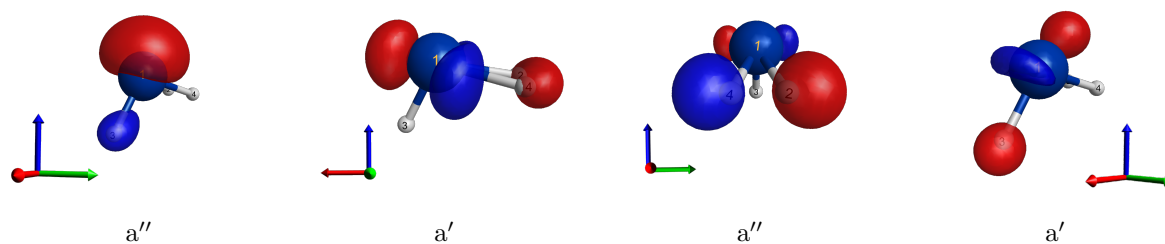


Figure 6.18: Molecular orbitals involved in the electronic transitions of SiH_3^+ metastable state

As seen previously for the SiH_2^+ case, the nuclear wavepacket propagation is not applicable and the cross sections were obtained using the LCM (details provided in Appendix B).

As can be seen in Fig. 6.19, for the ground state the LCM affects only in the first region. There, core-excitation activates the vibrational mode associated to the symmetric stretching (ν_4) by producing a broadening of 1.01 eV, as reported in Table 6.6.

Spectrum for $^3\text{SiH}_3^+$ exhibits more transitions, many leading to large vibrational deforma-

tion after core-excitation as seen in the results from LCM. Following the electronic transition analysis, the vertical spectrum was divided in four regions: 96 - 98.8 eV , 98.8 - 103.2 eV, 103.2 - 107.3 eV and 107.3 - 120 eV. The dynamics effects in the region above 107.3 eV were neglected since the strong CSFs mixing and the large numbers of transitions makes a correct analysis not possible. The comparison between the vertical and LCM spectrum is reported in Fig. 6.20. The regions I - III present a large vibrational progression which were fitted using a Gaussian FWHM of 1.31, 0.73 and 2.99 eV, respectively. In the former region, the wagging (ν_1) and the twisting (ν_2) vibrational mode of atoms 2 and 4 are activated. In Region II, a second wagging (ν_3) vibrational mode is activated in addition to the two presented before. The excitations in Region III activate, further the modes ν_1 and ν_2 , the asymmetric stretching (ν_5) is activated. Details about the vibrational modes can be found in Appendix B.

	Region	FWHM (eV)					
$^1\text{SiH}_3^+$	I	96 - 106.5 eV	1.01	$^3\text{SiH}_3^+$	I	96 - 98.8 eV	1.23
	II	106.5 - 120 eV	0.08		II	98.8 - 103.2 eV	0.68
			III		103.2- 107.3 eV	2.91	
			IV		107.3 - 120 eV	0.08	

Table 6.6: Full width half maximum (FWHM) in eV for the different region of ground and metastable states of SiH_3^+ , respectively $^1\text{SiH}_3^+$ and $^3\text{SiH}_3^+$.

The comparison between the theoretical and the experimental spectra is reported in Fig. 6.21. The fit of the population suggests a ratio between the ground and metastable state of 2:8 with a global shift of 3.7 eV. This behaviour is very different from the ones seen in the previous cases, two hypothesis can be proposed: whether a higher percentage of metastable state is produced in the ECRIS source or the fragmentation pathway for the ground and valence excited state leads to different products (Si^{2+} would be the most abundant product only for the last one).

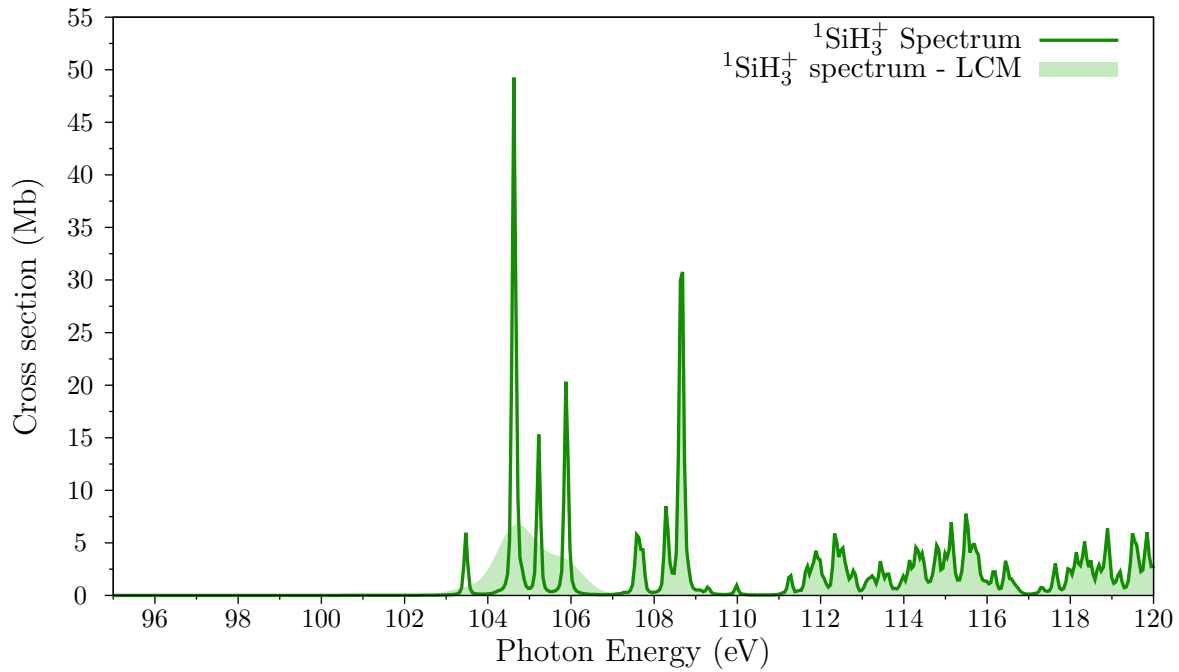


Figure 6.19: Comparison between the spectra computed within the vertical and linear coupling model for ${}^1\text{SiH}_3^+$

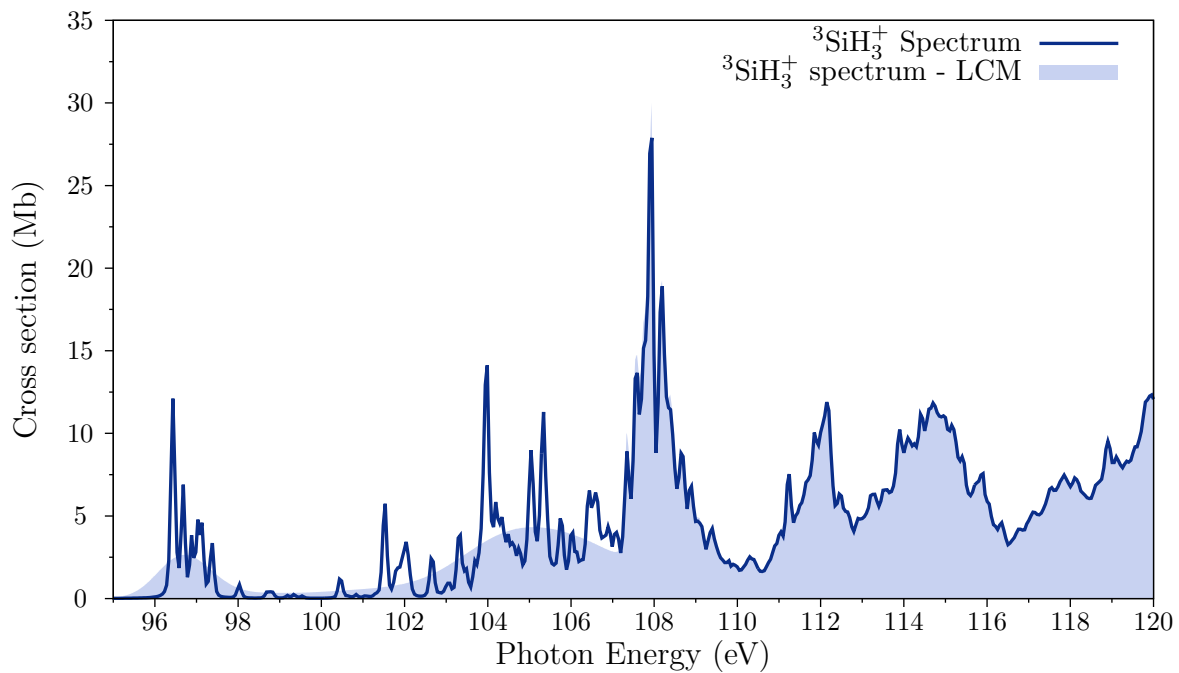


Figure 6.20: Comparison between the spectra computed within the vertical and linear coupling model for ${}^3\text{SiH}_3^+$

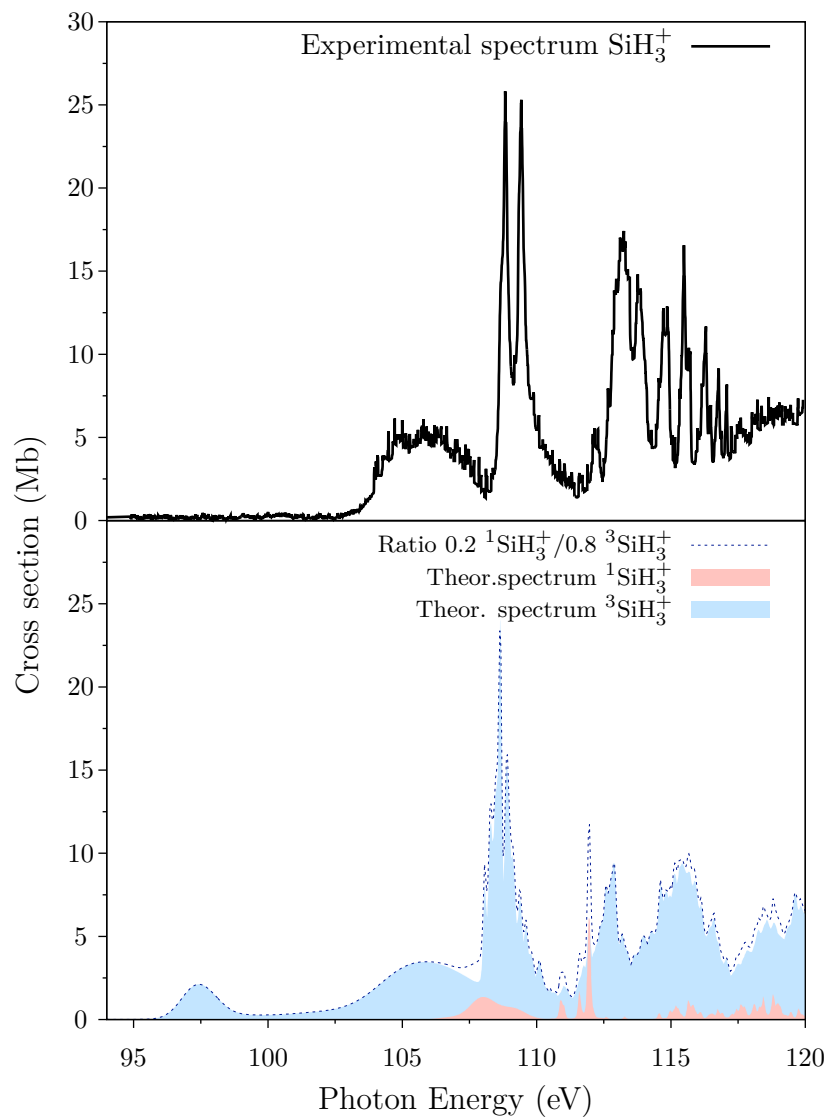


Figure 6.21: Experimental (top) and theoretical (bottom) spectra photoabsorption cross section for SiH_3^+ molecular ion

6.4 Infrared spectroscopy for the study of silicon molecular ions

As seen in the previous sections, our results suggest different ratios of ground/metastable state. This trend does not follow the energy gap between the states. Indeed, we could expect that a changing in the ratio from $\sim 60\%$ to $\sim 85\%$ is reasonable going from SiH^+ to SiH_2^+ since the energy gap increases (Fig. 6.9) the presence of the metastable species decrease. The results of SiH_3^+ provide a completely different scenario: even if the energy gap decreases again the ground state is present only for the 20%. Using the Boltzmann distribution, we obtain temperature in the order of $2 \cdot 10^3$ K for the first two systems and $2 \cdot 10^4$ K for SiH_3^+ . The use of a population distribution more suitable for the complex plasma sources are more complicated and go beyond the scope of this thesis.

In order to estimate the population ratio between the ground and metastable states, without requiring the fit employed so far, we proposed to use the IR spectroscopy.

We compute the IR spectra as follow. The vibrational frequencies and intensities were computed at Møller-Plesset second order perturbation (MP2) theory and the IR spectra were computed with a Lorentzian profile with FWHM of 35 cm^{-1} .

In Fig.6.22 are reported the IR spectra for the ground and metastable states of SiH^+ . The two species present only one vibrational modes but the energy and intensisty for the ground and metastable state are different. The peak for the two systems are far apart 134 cm^{-1} which permit to identify separately the different states.

The $^x\text{SiH}_2^+$ ($x= 2, 4$) IR spectra are shown in Fig. 6.23 and the different vibrational modes are reported in Appendix B. Since the two systems present very different spectra, we can identify each species.

In a similar way, the IR spectra of $^x\text{SiH}_3^+$ ($x= 1, 3$) are shown in Fig. 6.24 and the vibrational modes are reported in Appendix B. Differently from the SiH_2^+ molecular ions, the $\nu_4 - \nu_6$ vibrational modes of the ground state molecular ion have zero or very low intensities. Furthermore, because of the high symmetry of the $^1\text{SiH}_3^+$, the ν_4 mode (corresponding to the symmetric stretching) has zero intensity. The ν_5 and ν_6 modes (asymmetric stretching vibrational modes) have very low intensity and do not appear in the spectrum. Once again, we can recognize regions characteristic of one of the two systems, i. e. in the region above 1500 cm^{-1} only transitions of the metastable state are present.

In conclusion, the characteristics of the IR spectra presented above suggest that this spectroscopy could provide a powerful method to probe, in complement to x-ray absorption spectroscopy, the production of the metastable state in the ECRIS source.

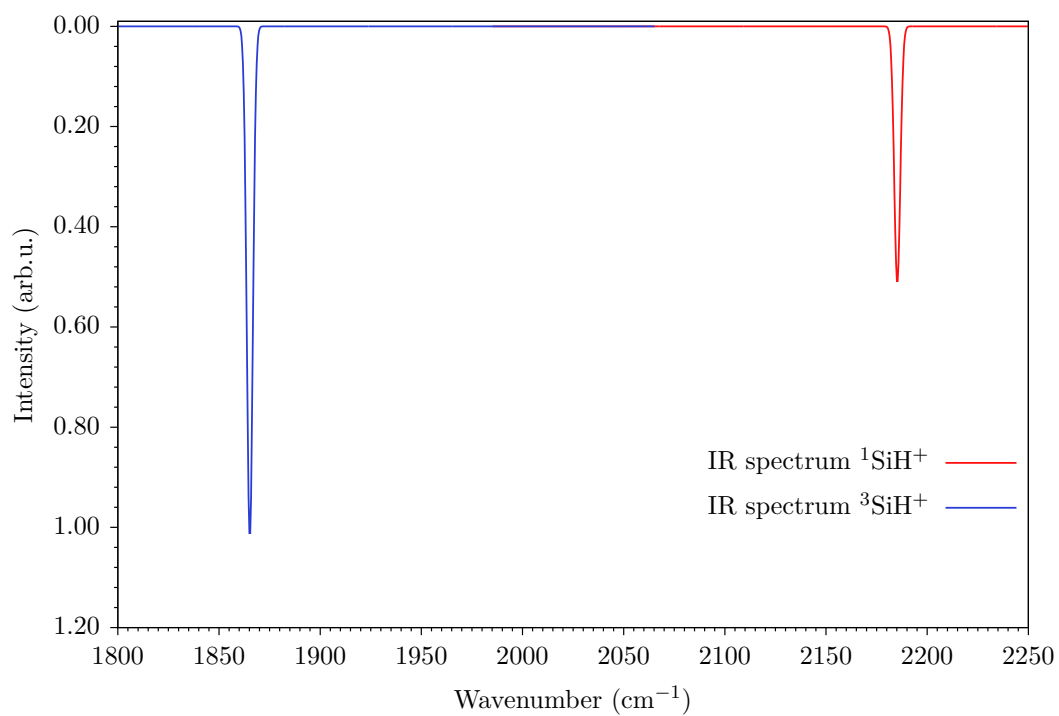


Figure 6.22: Simulated Infrared spectra of SiH^+ in the ground (red line) and metastable (blue line) state.

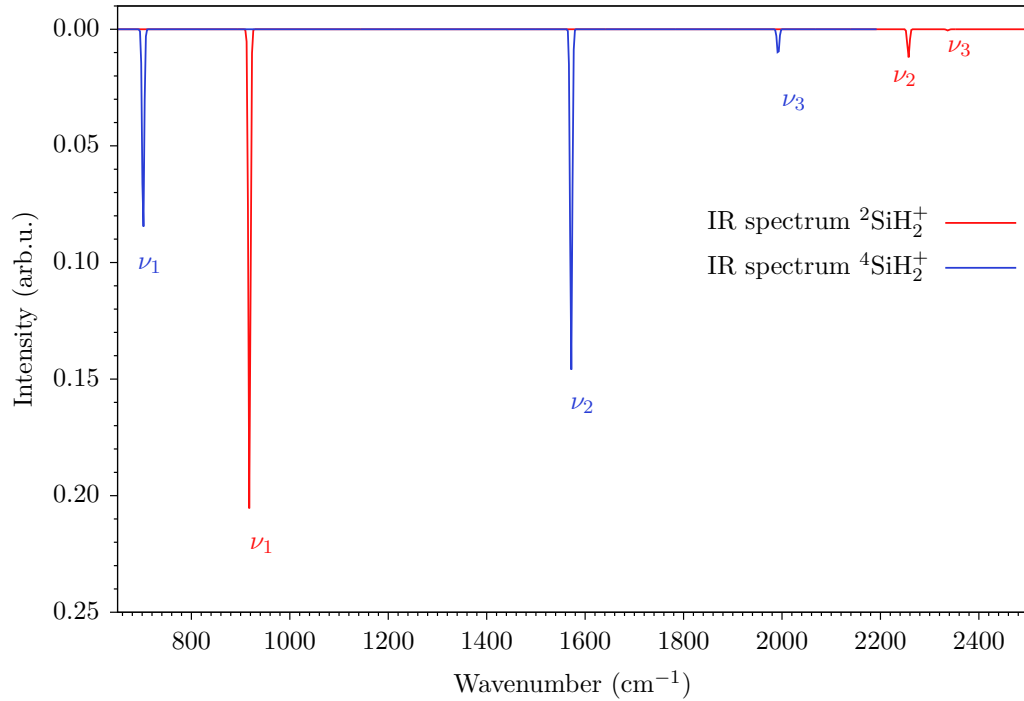


Figure 6.23: Simulated Infrared spectra of SiH_2^+ in the ground (red line) and metastable (blue line) state.

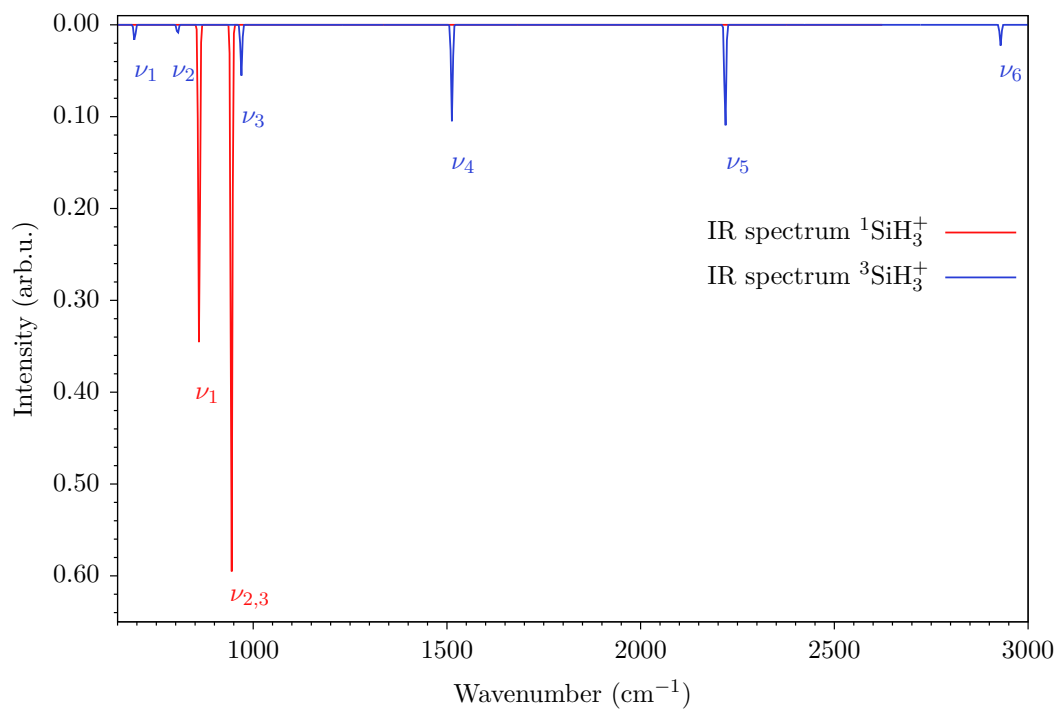


Figure 6.24: Simulated Infrared spectra of SiH_3^+ in the ground (red line) and metastable (blue line) state.

7 | Spin-orbit coupling correction to the 2p ionization potential of Silicon molecular ions

In this Chapter are reported the results concerning the spin-orbit correction of the silicon 2p ionization threshold through the use of an effective Hamiltonian. As reported in Chapter 4, we derived the matrix elements of the effective Hamiltonian for systems which present a doublet spin multiplicity in the core-ionized final state. Therefore, the ionization potential for SiH^+ and SiH_3^+ have been computed.

In Section 1 are discussed the results for the SiH^+ molecular ion. Firstly, the ground state properties and the binding energy using the Koopman's theorem are presented. Then the relaxation effects are taken into account and the effective spin-orbit constant is computed. Finally, using the effective Hamiltonian, the binding energies were computed including correlation effects with the CISD method. The SiH^+ results are compared to the benchmark molecule HCl and the prototype molecular ion HCl^{4+} .

The SiH_3^+ results are presented in Section 2 following the same pathway.

7.1 SiH^+

As seen in the previous Chapter, the silicon monohydrated cation has $(1s\sigma)^2(2s\sigma)^2(2p\pi)^4(2p\sigma)^2(4\sigma)^2(5\sigma)^2$ electronic configuration where the $(2p\pi)$ and $(2p\sigma)$ are the $2p_{x,y}$ and $2p_z$ silicon orbitals, respectively.

In the HF calculations, the $2p_{x,y}$ orbitals lie 30 meV lower than the $2p_z$ one. This order is inverted with respect to other linear molecules such as HCl (see in the following). The binding energies computed within the Koopman's theorem, e.g. $-\epsilon_{x,y}$ and $-\epsilon_z$ are 125.15 eV and 125.12 eV, respectively.

As seen before in Chapter 6, the relaxation effects due to the core-hole creation were taken into account by optimizing the orbitals for the $2s^{-1}$ core ionized state. The choice of this shell is dictated by the aim to avoid a preferential 2p sub-shell direction.

Using the relaxed orbitals, the $2p_{x,y} - 2p_z$ separation of the core ionized final states was computed within the 3/0/0 active space at CIS level. The energy values are respectively 118.650 eV and 118.55 eV with a splitting of 100 meV. Thus these energies were used to compute the value of Ω which permits to recover the energies computed using the Breit-Pauli $2e$ operator (Eq. 4.2.1). We found a good agreement between the energies using the Breit-Pauli operator and the effective Hamiltonian for $\Omega = 0.407$ eV. The spectra simulated within the two methods are reported in Fig. 7.1 (left) and they are in excellent agreement. The photoelectron spectrum presents two main bands the first of which presents a fine structure. The band at lower energy is formed by two sub-components corresponding to the $2p_{M_J=1/2}(^2\Sigma_{1/2}^+)$ and $2p_{M_J=3/2}(^2\Pi_{3/2})$ final states. The second band is due to the $2p_{M_J=1/2}(^2\Pi_{1/2})$ final state. The estimated $L_{II,III}$ spin-orbit splitting of the Si was found in the order of 0.08 eV. As can be seen in Fig. 7.1, the branching ratio (peaks height) is ≈ 1.51 , clearly different from the atomic case (ratio of 2).

The results discussed above show that the effective Hamiltonian can replace the Breit-Pauli operator and then permits to include the SOC in CI calculations including higher excitations.

Correlation effects were included through the CISD calculations allowing the excitation from the outermost electrons ($3s\sigma^2$)($3p\sigma^2$) in the extended active space 3/2/150. The introduction of correlation effects leads to a $2p_{x,y} - 2p_z$ separation of ≈ 373 meV. The energy of the states from the CIS-3/0/0 and CISD-3/0/150 calculations accounting the SOC are reported in Table 7.1 and the related spectra are shown in Fig. 7.1 left and right panel, respectively.

The results from the CISD-3/2/150 calculations change both the absolute and relative positions of the peaks. The spectrum is red-shifted by 0.65 eV and the fine structure presents a larger gap, as can be seen from Table 7.1. The energy difference between the first two peaks goes from 0.07 for the 3/0/0 active space to 0.65 eV for the 3/2/150 active space.

Config.	CIS-3/0/0					CISD-3/2/150				
	E (eV)	Composition			Splitting	E (eV)	Composition			Splitting
		2p _x	2p _y	2p _z		2p _x	2p _y	2p _z		
$^2\Sigma_{1/2}^+$	118.37	13.3	13.3	73.3	—	117.72	6.12	6.12	87.5	—
$^2\Pi_{3/2}$	118.45	50.0	50.0	0.0	0.08	118.07	50.0	50.0	0.0	0.65
$^2\Pi_{1/2}$	119.03	36.6	36.6	26.7	0.58	118.59	43.7	43.7	12.5	0.52

Table 7.1: SiH⁺ 2p⁻¹ relativistic states computed with the CIS-3/0/0 and CISD-3/2/150 methods

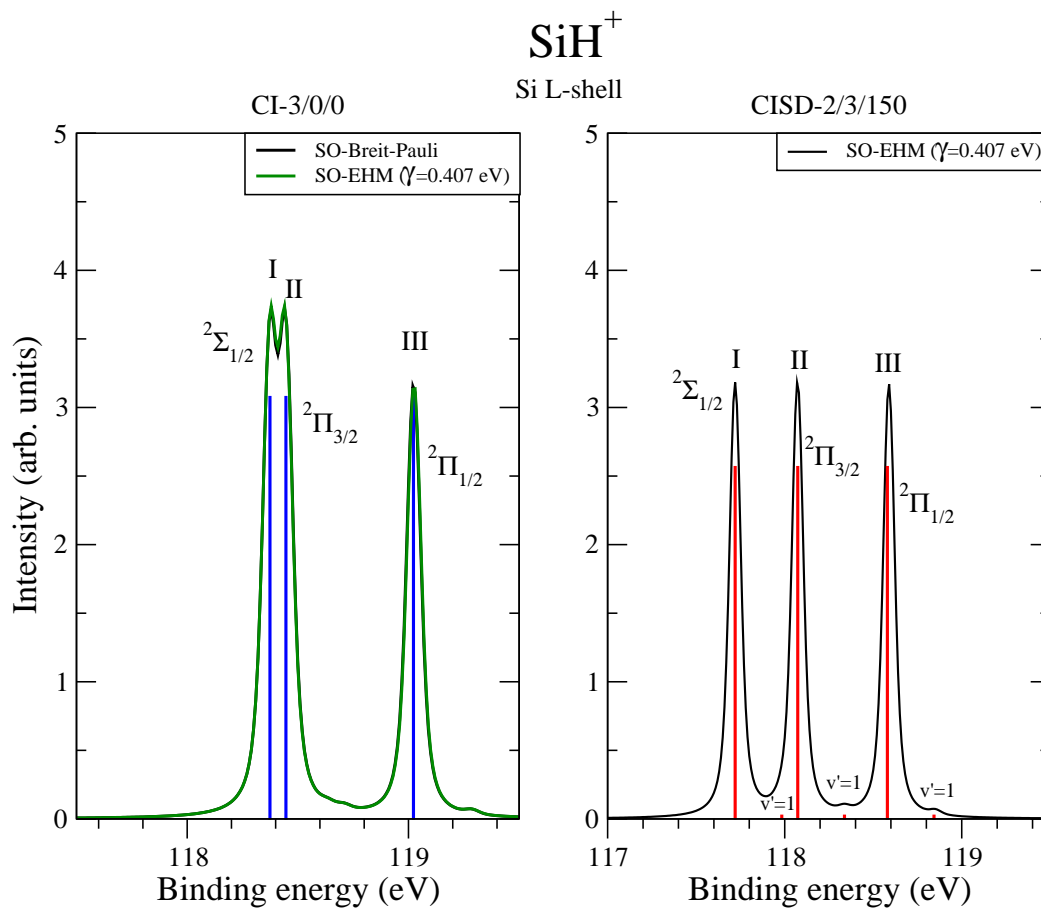


Figure 7.1: SiH⁺ binding energy spectra computed with the CIS-3/0/0 (left) and CISD-3/2/150 (right) methods

The vibrational progression was accounted for the binding energy spectrum through the LCM. We observed that the peaks present a shoulder due to the transition toward the ν'_1 vibrational excited states.

The above presented method was tested on the benchmark molecule HCl since its photoelectron spectrum was studied from the theoretical and experimental point of view [83]. Then the prototype molecular ions HCl^{4+} was used to have a direct comparison with SiH^+ because it belongs to the $C_{\infty v}$ point group and is isoelectronic to SiH^+ .

HCl has electronic configuration $(1s\sigma)^2(2s\sigma)^2(2p\sigma)^2(2p\pi)^4(3\sigma)^2(4\sigma)^2(2\pi)^4$ where the $(2p\sigma)^2$ and $(2p\pi)^4$ are essentially the z and $2p_{x,y}$ of the chlorine. The bond distance and frequency were computed at DFT/B3LYP level of theory. The computed values are 1.2804 Å and 2923 cm^{-1} , respectively, and they are in good agreement with the experimental data (1.275 Å and 2990.9 cm^{-1} [103]).

In the ground state, the $2p_z$ orbital is 40 meV below the $2p_{x,y}$ ones. This splitting is in the same order of magnitude of the one computed for the SiH^+ molecular ion but the 2p orbitals order is inverted. The energy binding computed with the Koopman's theorem are 218.78 eV and 218.82 for the $2p_{x,y}$ and $2p_z$, respectively.

The binding energy spectrum computed at CIS-3/0/0 level is reported in Fig. 7.2. Using the effective Hamiltonian the $\Omega_{Cl_{2p}}$ value was found to be 1.08 eV, which agrees with the parameter determined both theoretically [83] and experimentally [104]. The fine structure of the first peak is due to the ${}^2\Pi_{3/2}$ and ${}^2\Sigma_{1/2}^+$ state which have inverted order with respect to the SiH^+ case. As reported in Table 7.2, the energy splitting between these states is found to be 45 meV underestimating the experimental value (85 ± 6 meV [83]).

Correlation effects were accounted for by computing the non relativistic energies with the CISD method and the 3/4/150 active space. The resulting energy values and the $\Omega_{Cl_{2p}}$ were used to diagonalize the effective Hamiltonian matrix and to obtain the relativistic energies. The calculations lead to an energy splitting ${}^2\Pi_{3/2} - {}^2\Sigma_{1/2}^+$ of 78 meV which is in good agreement with the experimental value of 86 ± 6 meV [83].

As can be seen from Table 7.2 and Fig. 7.2, the introduction of correlation effects play a role in the absolute and relative position of the peaks. The absolute energy of the first band is shifted to lower energy and the fine structure of the first peak presents a larger splitting, the separation between the ${}^2\Sigma_{1/2}^+$ and ${}^2\Pi_{1/2}$ remains almost unchanged.

Config.	CIS-3/0/0					CISD-3/4/150				
	E (eV)	Composition			Splitting	E (eV)	Composition			Splitting
		2p _x	2p _y	2p _z		2p _x	2p _y	2p _z		
$^2\Pi_{3/2}$	207.024	50.0	50.0	0.0		206.554	50.0	50.0	0.0	
$^2\Sigma_{1/2}^+$	207.069	17.6	17.6	64.8	0.045	206.662	18.4	18.4	63.3	0.078
$^2\Pi_{1/2}$	208.660	32.4	32.4	35.2	1.591	208.200	36.8	36.8	26.7	1.538

Table 7.2: HCl $2p^{-1}$ relativistic states computed with the CIS-3/0/0 and CISD-3/2/150 methods

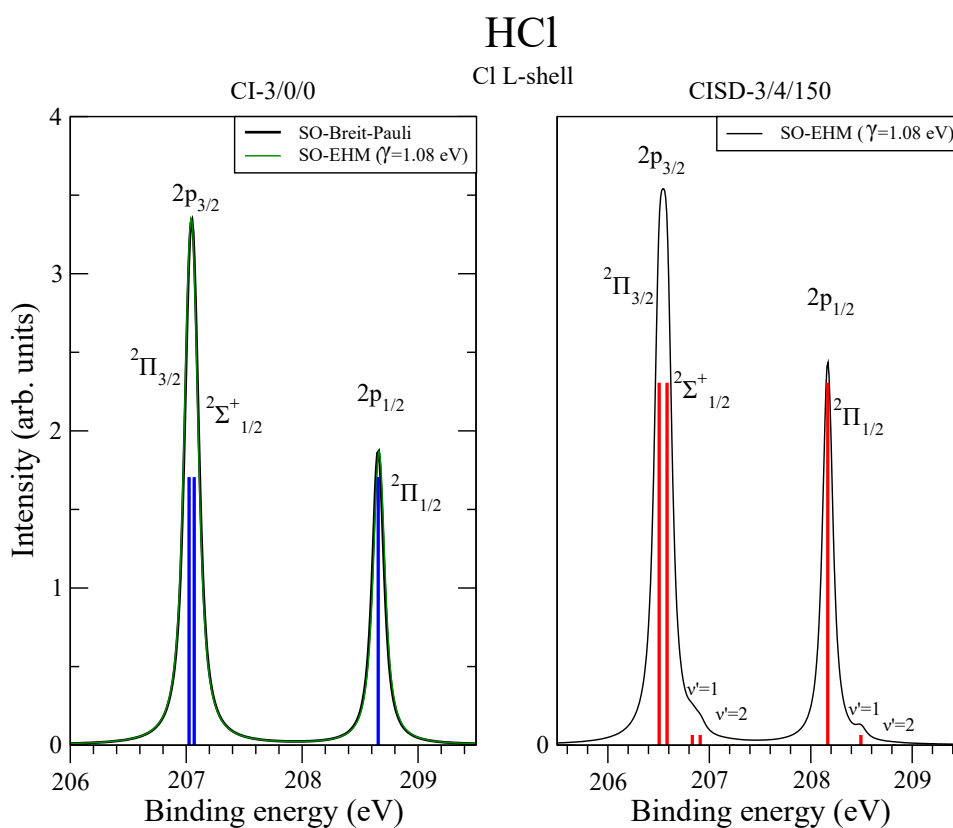


Figure 7.2: HCl photoelectron spectra computed with the CIS-3/0/0 (left) and CISD-3/2/150 (right) methods

In the CISD-3/4/150 calculations, the vibrational effects were included throughout the

LCM (Fig. 7.2, right panel). The spectrum exhibits a weak shoulder, experimentally observed [83].

It should be mentioned that HCl^{4+} , which is isoelectronic to SiH^+ , presents the same orbitals ordering than the latter. The $2p^{-1}$ ionization potential computed with the Koopman's theorem are 277.68 and 277.16 eV for the $2p_{x,y}$ and $2p_z$ state, respectively. The energy gap is thus 68 meV.

The comparison between SiH^+ , HCl and HCl^{4+} is qualitative and based on the electronic structure of the systems in their ground state. As well as SiH^+ , the isoelectronic HCl^{4+} exhibits the same $2p_z$ - $2p_{x,y}$ inversion with respect to the benchmark molecule HCl . Our suggestion is that the order of the 2p orbitals is strictly related to the 14 electrons of the linear molecules which leads to an incomplete filling of the MOs corresponding to the 3p level of the central atom. In order to elucidate the particular behaviour related to this electronic configuration, a deeper analysis of these systems is ongoing.

The above illustrated method to the calculations of the binding energy spectrum was applied to the SiH_3^+ molecular ion.

7.2 SiH_3^+

As presented in Chapter 6, the SiH_3^+ molecular ion has a planar geometry and it belongs to the D_{3h} point group with electronic configuration $1a_1'^2 2a_1'^2 1a_2'^2 1e'^4 3a_1'^2 2e'^4$. The $1e'^4$ and $3a_1'^2$ correspond to the $2p_z$ and $2p_{x,y}$ orbitals of the silicon and, unlike SiH^+ , the $2p_z$ orbital lies 84 meV lower than the $2p_{x,y}$. The $2p_{x,y}$ and $2p_z$ binding energies computed within the Koopman's theorem are 124.22 eV and 124.31 eV, respectively.

The $2p_z$ - $2p_{x,y}$ splitting of the core ionized final states computed at the CIS level within the 3/0/0 active space leads to a non-relativistic energy splitting of ≈ 150 meV. These states have binding energy of 116.90 eV and 117.50 eV, respectively. The 2p splitting is strongly increased with respect to the one computed within the Koopman's approximation. Once that the spin-orbit coupling interaction is explicitly taken into account three different peaks appear and are termed respectively $^2\Pi_{3/2}$, $^2\Sigma_{1/2}^+$ and $^2\Pi_{1/2}$. The energies including the SOC were computed with the 3/0/0 active space using the effective Hamiltonian and then they were compared with the results from the Breit-Pauli operator ($2e$ method). As shown in Fig. 7.3 (left), the spectra resulting from the two methods are nearly identical. The relative positions were computed at 116.75 eV and 116.80 eV for $^2\Pi_{3/2}$ and $^2\Sigma_{1/2}^+$ states and 117.9 eV for the $^2\Pi_{1/2}$ state.

The correlation effects were included through CISD calculations with the 3/3/150 active space and the SOC is taken into account through the effective Hamiltonian. The IPs are reported in Fig. 7.3 (right). As seen before for the SiH^+ case, the introduction of correlation effects has two different effects: a red shift of the first peak and a larger energy splitting between the ${}^2\Pi_{3/2}$ and ${}^2\Sigma_{1/2}^+$ states.

Config.	CIS-3/0/0					CISD-3/3/150				
	E (eV)	Composition			Splitting	E (eV)	Composition			Splitting
		$2p_x$	$2p_y$	$2p_z$		$2p_x$	$2p_y$	$2p_z$		
I,II	116.69	50.0	50.0	0.0	—	116.23	50.0	50.0	0.0	
III,IV	116.79	22.7	22.7	54.6	0.10	116.79	28.5	28.5	42.9	0.56
V,VI	117.36	27.3	27.3	45.4	0.57	116.97	21.9	21.9	57.1	0.18

Table 7.3: SiH_3^+ $2p^{-1}$ relativistic state computed with the CIS-3/0/0 and CISD-3/2/150 methods

In conclusion, we computed the binding energy spectra for SiH^+ and SiH_3^+ molecular ions. The calculations were carried out at CIS-3/0/0 level with both the effective Hamiltonian and Breit-Pauli operator. The results shown that the effective Hamiltonian reproduces the energies obtained from the Breit-Pauli operator. The computed value of the SOC constant Ω for the Silicon is 0.407 eV. Unlike the computationally expensive Breit-Pauli operator, the effective Hamiltonian permits to include correlation effects in the SOC calculations leading to a better description of absolute and relative energies.

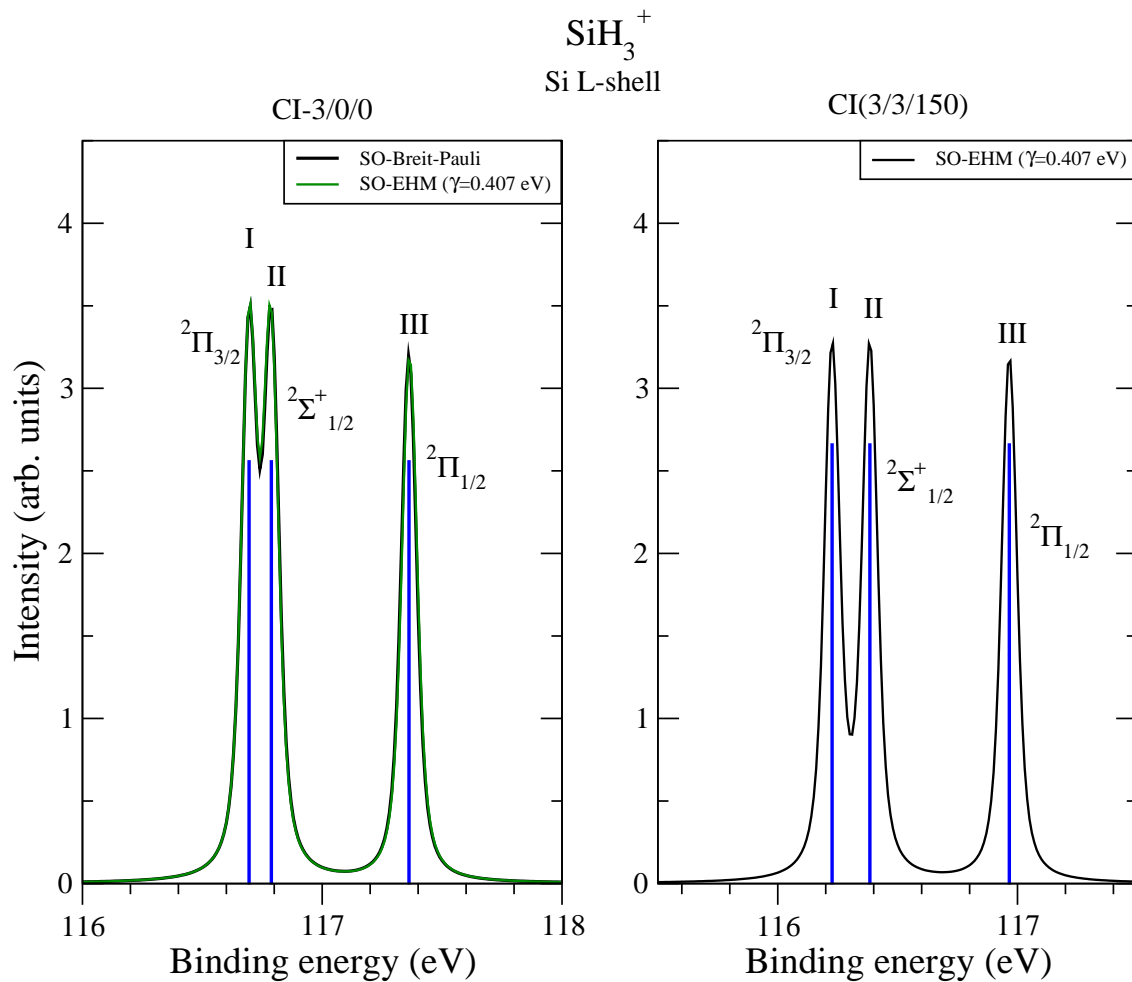


Figure 7.3: SiH_3^+ photoelectron spectra computed with the CIS-3/0/0 (left) and CISD-3/2/150 (right) methods

8 | Conclusions and perspectives

In this thesis work the X-ray photoabsorption spectra of various protonated molecular ions of C, O and Si generally labelled XH_n^+ ($X = \text{C, O, Si}$; $n = 1, 2, 3$) have been investigated. We used a combination of electronic structure and nuclear dynamics methods to study the electronic properties of the systems. The protocols have been developed separately for the K and L-shell excitation edge since the states involved have different characteristics.

The most important accomplishments and perspective for the K-shell systems are summarized in the following points.

- The K-shell photoabsorption spectra were calibrated using the simplest molecular ion, CH^+ as case study. The optimal size of the active space and the spin-orbitals optimization were evaluated. The use of an active space reduced to spin-orbitals having energy up to the 1s ionization threshold permits to reduce by 3 the time of the calculations. Within this smaller active space, the set of spin-orbitals optimized for the lowest triplet core-excited state provides the best reference for the PESs and transition dipole moment calculations. Furthermore, we have shown that the harmonic approximation allows to reduce further the cost of the computations while keeping accurate spectra.

Using this protocols, we computed the XAS spectra for CH^+ and OH^+ in their ground state but also in their lowest metastable state. We have demonstrated that, in the ECRIS source used by our colleagues experimentalist, a significant account of molecular ions are in the latter state. The comparison between theory and experiment allowed to estimate the population ratio.

- The K-shell protocol was applied to the CH_n^+ and OH_n^+ ($n = 2, 3$) molecular ions. The experimental data for diprotonated systems suggest low cross sections (below 1 Mb). Two

hypothesis have been put forward: either for these systems the electronic transitions indeed present a very low cross section or these molecular ions follow fragmentation pathways that are not detectable in the experimental set-up (final product different from X^{2+}). Results show that the XAS exhibit intense transitions (cross sections higher than 10 Mb). The second hypothesis must be investigated.

As perspective of this work, we would like to study of the fragmentation pathways. The Auger decay will be probed through the FANO-CI method [105]. The subsequent fragmentation states will be investigated via a combination of quantum chemistry (MCSCF) and surface hopping ab-initio molecular dynamics methods [106, 107].

The achievement and perspective arising from the development of the L-shell protocol are reported in the following point.

- Computing L-shell XAS is much more demanding than the corresponding K-shell spectra owing to the strong spin-orbit coupling. Therefore we studied this effects by evaluating the inclusion of the valence orbitals and different spin-orbit coupling operators. The dynamics of the core-excited states was probed both with nuclear wavepacket propagation and the linear coupling model. We observed that, even if the linear coupling model is rather simple, it represents a good method to probe the dynamics for bigger systems.
- In the last part of this thesis work, we derived a simple approach for the accurate calculations of ionization potential which includes explicitly the spin-orbit coupling without the need of the Breit-Pauli operator. This method includes the use of an effective Hamiltonian and permits to include the correlation effects since it requires only the accurate energies without spin-orbit coupling.

The matrices for the effective Hamiltonian have been derived only for system which present a singlet spin multiplicity in the ground state. Therefore, it was applied to the SiH^+ and SiH_3^+ molecular ions.

As perspective of this work, we want to develop the expressions to the effective Hamiltonian for all the possible cases where $2p_x, y, z$ or only $2p_x, y$ are degenerate and where the degeneracy is lifted.

Appendix

Appendix A:

Effective Hamiltonian derivation

In this appendix the details concerning the derivation of the effective spin-orbit Hamiltonian presented in Section 4.2.2 are reported.

Effective Hamiltonian derivation

The effective spin-orbit Hamiltonian can generally written as

$$H_{SO} = \sum_{i=1}^{n_{el}} \hat{P}_{2p}(\Omega \hat{l}_i \hat{s}_i) \hat{P}_{2p} \quad (\text{A.1})$$

where \hat{P}_{2p} is the projection operator on the 2p orbitals of the silicon, \hat{l}_i and \hat{s}_i are the angular and spin operator and Ω is the spin orbit coupling parameter associated to the silicon 2p shell.

Being $l_{\pm} = l_x \pm il_y$ and ψ_{m_l} the electronic wavefunction characterized by the magnetic quantum number m_l we obtain the following equations

$$l_z |\psi_{m_l}\rangle = \hbar m_l |\psi_{m_l}\rangle \quad (\text{A.2})$$

$$l_{\pm} |\psi_{m_l}\rangle = \hbar \sqrt{l(l+1) \pm m_l(m_l \pm 1)} |\psi_{m_l \pm 1}\rangle \quad (\text{A.3})$$

In a similar way, for a wavefunction characterized by spin s with m_s spin quantum number we have

$$s_z|\psi_{m_s}\rangle = m_s|\psi_{m_s}\rangle \quad (\text{A.4})$$

$$s_{\pm}|\psi_{m_s}\rangle = \hbar\sqrt{s(s+1) \pm m_s(m_s \pm 1)}|\psi_{m_s \pm 1}\rangle \quad (\text{A.5})$$

The $\hat{l}\hat{s}$ coupling for the i^{th} electron is

$$\hat{l}_i\hat{s}_i = \left(\frac{1}{2}l_{+,i}s_{-,i} + \frac{1}{2}l_{-,i}s_{+,i} + l_{z,i}s_{z,i} \right) \quad (\text{A.6})$$

For a system which is closed-shell in the ground state, the $2p^{-1}$ ionized state has a doublet spin multiplicity, this is the case of SiH^+ and SiH_3^+ systems. The results of Eq. A.3 and A.5 for this final states are reported in Table A.1 and A.2 respectively.

l	m_l	l_+	l_-
1	-1	$\hbar\sqrt{2} 0\rangle$	0
	0	$\hbar\sqrt{2} 1\rangle$	$\hbar\sqrt{2} -1\rangle$
	1	0	$\hbar\sqrt{2} 0\rangle$

Table A.1: Eigenvalue of \hat{l}_i , the m_{l_i} is contained in the ket notation

s	m_s	s_+	s_-
$\frac{1}{2}$	$\frac{1}{2}$	0	$\hbar \beta\rangle$
	$-\frac{1}{2}$	$\hbar \alpha\rangle$	0

Table A.2: Eigenvalue of \hat{s}_i , the m_{s_i} is contained in the ket notation where α and β stand for spin "up" and "down"

The final relativistic final states for the different values of m_l and m_s are reported in Table A.3

Applying Eq. A.6 on the $2p^{-1}$ wavefunctions, $2p_{\pi_+}^{\alpha,\beta}$, $2p_{\pi_-}^{\alpha,\beta}$ and $2p_{\sigma}^{\alpha,\beta}$ using the eigenvalue in Tables A.1 and A.2 we obtain

$$H_{SO}^{2p}2p_{\pi_+}^{\alpha} = \frac{\hbar^2}{2}2p_{\pi_+}^{\alpha} \quad (\text{A.7})$$

Relativistic state	l	m_l	m_s
$2p_{\pi_+}^\alpha$		+1	1/2
$2p_{\pi_+}^\beta$		+1	-1/2
$2p_\sigma^\alpha$	1	0	1/2
$2p_\sigma^\beta$		0	-1/2
$2p_{\pi_-}^\alpha$		-1	1/2
$2p_{\pi_-}^\beta$		-1	-1/2

Table A.3: Relativistic states for the possible m_l and m_s quantum number.

$$H_{SO}^{2p} 2p_{\pi_+}^\beta = \frac{\hbar^2 \sqrt{2}}{2} 2p_{\pi_\sigma}^\alpha - \frac{\hbar^2}{2} 2p_{\pi_+}^\beta \quad (\text{A.8})$$

$$H_{SO}^{2p} 2p_{\pi_-}^\alpha = \frac{\hbar^2 \sqrt{2}}{2} 2p_{\pi_\sigma}^\beta - \frac{\hbar^2}{2} 2p_{\pi_-}^\alpha \quad (\text{A.9})$$

$$H_{SO}^{2p} 2p_{\pi_-}^\beta = \frac{\hbar^2 \sqrt{2}}{2} 2p_{\pi_-}^\beta \quad (\text{A.10})$$

$$H_{SO}^{2p} 2p_\sigma^\alpha = \frac{\hbar^2 \sqrt{2}}{2} 2p_{\pi_+}^\beta \quad (\text{A.11})$$

$$H_{SO}^{2p} 2p_\sigma^\beta = \frac{\hbar^2 \sqrt{2}}{2} 2p_{\pi_-}^\alpha \quad (\text{A.12})$$

Projecting on the states we obtain the coupling matrix

$$H_{SO}(2p^{-1}) = \begin{pmatrix} E(^2\pi_+) + \Omega/2 & 0 & 0 & 0 & 0 & 0 \\ 0 & E(^2\pi_-) - \Omega/2 & 0 & 0 & 0 & \Omega/2 \\ 0 & 0 & E(^2\sigma) & \Omega/2 & 0 & 0 \\ 0 & 0 & \Omega/2 & E(^2\pi_+) - \Omega/2 & 0 & 0 \\ 0 & 0 & 0 & 0 & E(^2\pi_-) + \Omega/2 & 0 \\ 0 & \Omega/2 & 0 & 0 & 0 & E(^2\sigma) \end{pmatrix} \quad (\text{A.13})$$

where the energies on the diagonal are the non-relativistic energies of the 2p states. From the diagonalization of the matrix in Eq. A.13, the relativistic energies of the 2p states are obtained.

Appendix B:

Application of the linear coupling model to the SiH_n^+ ($n=1,2,3$) molecular ions

In this Appendix are reported the details of the calculations on the linear coupling model are applied to SiH_n^+ ($n= 1 - 3$) molecular ions.

For the di- and tri-protonated silicon molecular ions, the evaluation of the core-excited state dynamics through the nuclear wavepacket propagation is not affordable. The reasons lie in the very different equilibrium geometry of the ground and metastable state which make the HA not sufficient to explore the minimum of the PESs and in the high computational cost to carry out complete calculations, i.e. about 20 days for SiH_2^+ for a single point calculation. For these reasons, we choose to use the linear coupling model, which is presented in Chapter 4. The results are then compared with the experimental data and are presented in Chapter 6.

The LCM was applied as illustrated in the following points:

1. The most intense transitions were identified from the calculation without SOC.
2. The spectrum with SOC was divided in different regions accordingly to the transitions identify in 1.
3. For each transition, we compute the coupling constant of each normal mode. The vibrational distribution is thus obtained. When the number of vibrational level populated was large, the corresponding region was convoluted with a Gaussian profile (Eq. 2.4.10) otherwise a Voigt's profile was used. In the former case the Gaussian FWHM was the sum of the experimental band pass (200 meV) and the results of the calculations.

In the following sections the results for each molecular ion are presented separately.

SiH⁺

The monoprotonated molecular ion SiH⁺ is a singlet spin system in its ground state and triplet in the metastable state. It belongs to the C_{∞v} point group and it has only one normal mode. Frequency and reduced masses both ground and metastable state are reported in Table B.4.

Molecular ion	Frequency (cm ⁻¹)	Normal mode
	Reduced mass (a.m.u.)	ν_1
¹ SiH ⁺	ω	2233.4
	μ	1.04278
³ SiH ⁺	ω	2161.9
	μ	1.04278

Table B.4: Normal modes $^x\text{SiH}^+$ ($x = 1, 3$)

In Fig. B.1 are reported the spectra for ¹SiH⁺ and ³SiH⁺ without and with spin-orbit coupling. The ground state spectrum was divided in three regions, the first, below 102 eV, corresponds to the transition toward the 1 π state, the second one located between 102.0 and 108.2 eV and corresponds to the 2 $p^{-1} \rightarrow n\pi^*$ states. The region above is characterized by transition to $n\delta^*$, $n\pi^*$ and Rydberg states. The last region presents high density of transition and the presence of states with strong CSFs mixing does not permit to have a clear picture of the electronic transitions. The dynamics was neglected. As reported in Table B.7, the Region II is affected by the excited state dynamics and for this transitions convolution with a Gaussian of a FWHM of 1.28 eV was applied.

The vertical spectrum for ³SiH⁺ was divided in four regions. The first one below 99 eV corresponds to the transitions toward the singly occupied MOs. The other transitions have the same characters of the ¹SiH⁺. As well as for the ground state, the region which presents a large vibrational progression is the one involving the 2 $p \rightarrow n\pi^*$ transition between 104 and 108 eV.

The vibrational distribution for a representative of each region for ¹SiH⁺ and ³SiH₃⁺ are given in Tables B.7 and B.8, respectively. The comparison between the spectra with and without nuclear dynamics is reported in Section 6.1.3.

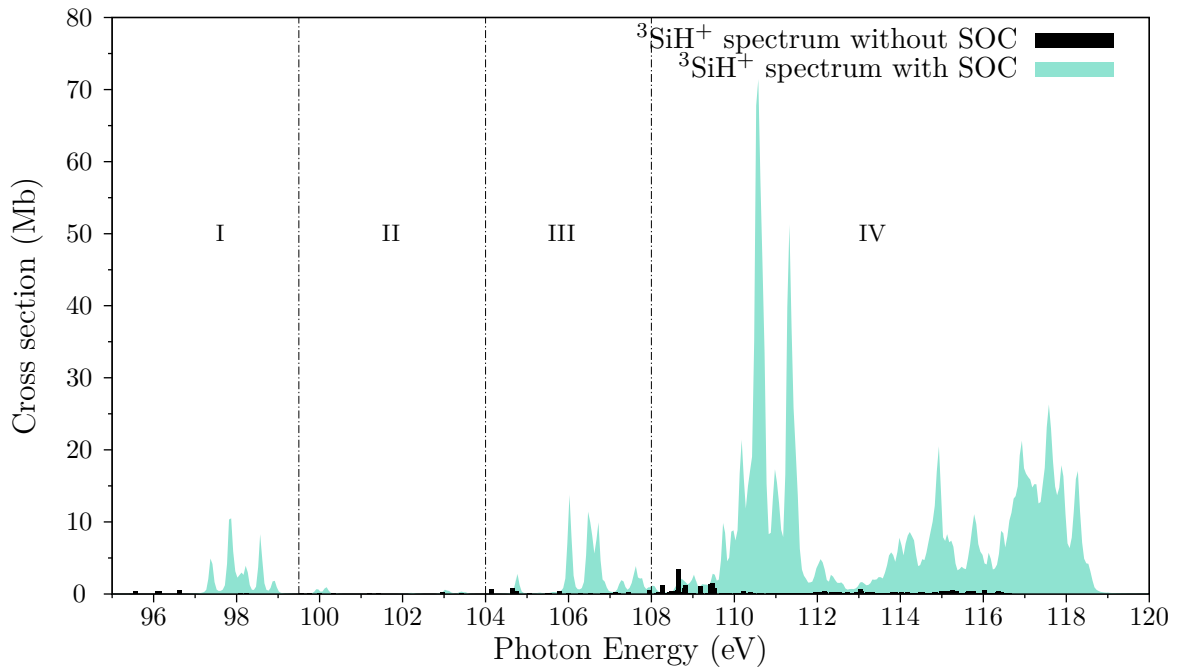
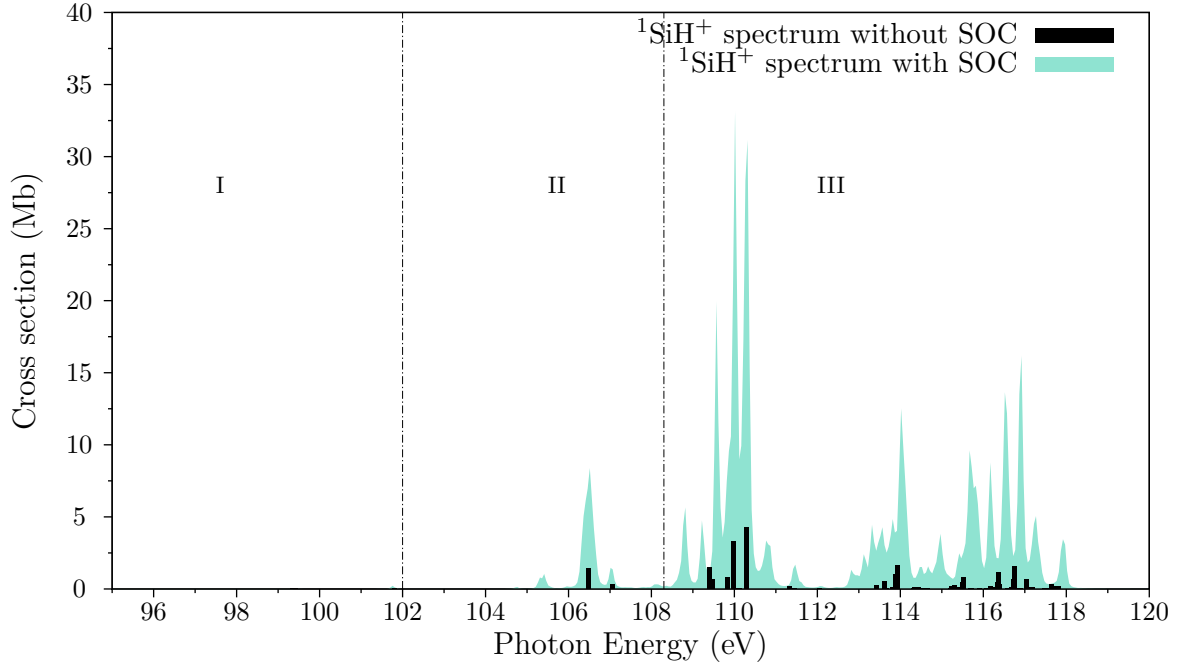


Figure B.1: Vertical X-ray photoabsorption spectra of $^1\text{SiH}^+$ (top) and $^3\text{SiH}^+$ (bottom)

SiH₂⁺

SiH₂⁺ is a doublet spin system in the ground state and a quadruplet in the metastable state.s Both state belong to the C_{2v} point group. It has three vibrational modes represented in Fig.B.2 and B.3 for the ground and valence excited state, respectively.

For both states, frequencies and the reduced masses associated to the vibrational modes are reported in Table B.5.

Molecular ion	Frequency (cm ⁻¹)	Normal mode		
	Reduced mass (a.m.u.)	ν_1	ν_2	ν_3
² SiH ₂ ⁺	ω	967.	2313	2380
	μ	1.059	1.025	1.060
⁴ SiH ₂ ⁺	ω	692	744	1710
	μ	1.080	1.020	1.064

Table B.5: Normal modes $^xSiH_2^+$ ($x = 2, 4$)

For both systems the spectrum computed within the vertical approximation was divided in four parts (Fig.B.4) but the dynamics effects were considered only in the first three for the same reasons previously described for SiH⁺.

For SiH₂⁺ ground state, the evaluation of the vibrational distribution suggests that the transition involved in the Region I - III presents important nuclear dynamics. The photon absorption in Regions I and II activates of the bending normal mode, ν_1 in Fig. B.2. Differently, the broadening in Region II is due to the symmetric stretching vibrational mode, ν_2 in Fig. B.2.

The picture is different for ⁴SiH₂⁺ where the broadening in Region I -III has a different nature. The excitation below 100 eV causes the concomitant activation of the bending and symmetric stretching modes, ν_2 and ν_3 in Fig. B.3, while Region II activates the asymmetric stretching modes. All vibrational modes are responsible of the large FC distribution in the third region.

The FC distribution for the ground and metastable state are reported in Table B.9 and B.10, respectively.

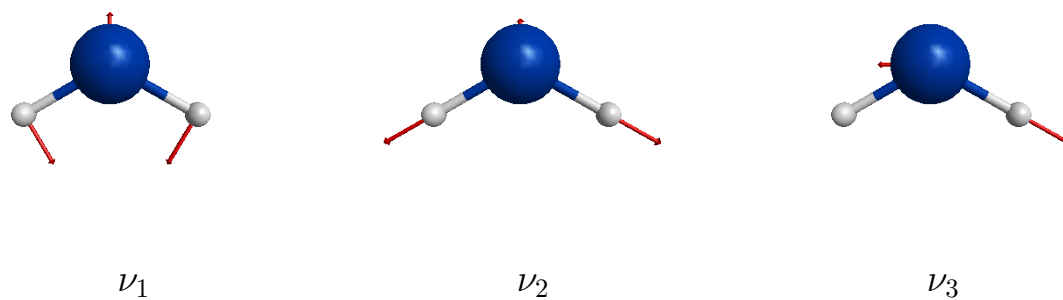


Figure B.2: ${}^2\text{SiH}_2^+$ normal modes.

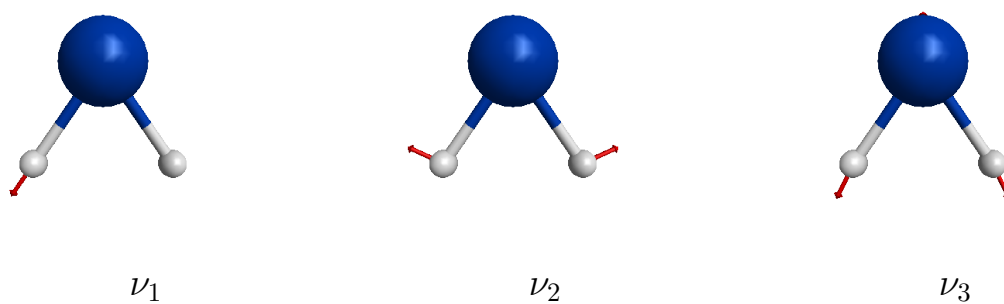
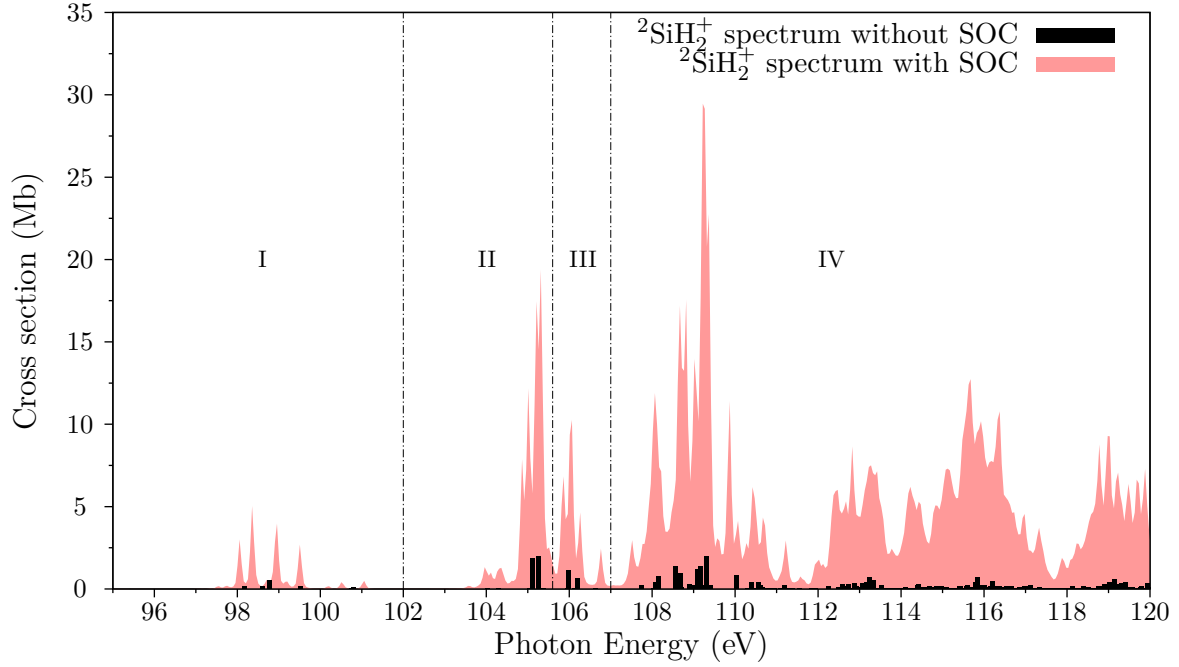
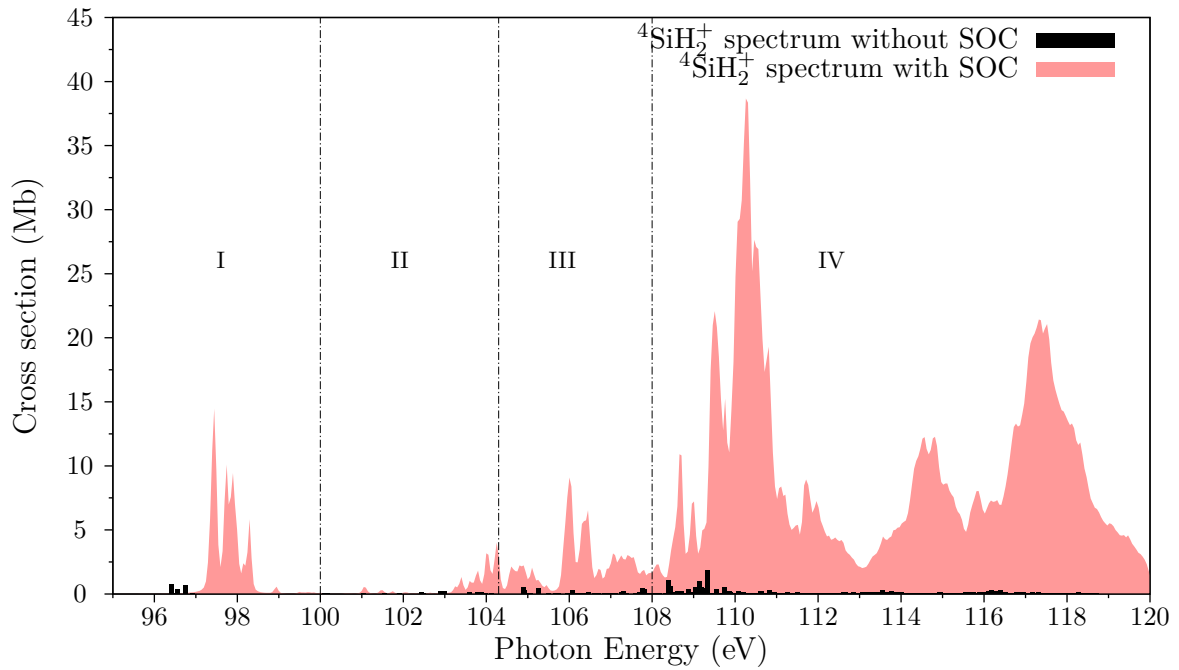


Figure B.3: ${}^4\text{SiH}_2^+$ normal modes.



(a)



(b)

Figure B.4: Vertical X-ray photoabsorption spectra of ${}^2\text{SiH}_2^+$ (top) and ${}^4\text{SiH}_2^+$ (bottom)

SiH₃⁺

The Sylil cation, SiH₃⁺ in its ground state belongs to the D_{3h} point group while it has C_s symmetry in the valence excited state. It has 6 vibrational normal modes which frequencies and reduced masses are reported in Table B.6.

The photoabsorption spectrum for the ground state appears quite simple. It was divided in two regions according to the involved electronic transitions, as shown in Fig. B.7a. Only the first region presents a large FC distribution which is associated to the vibrational mode ν_4 (symmetric stretching), represented in Fig. B.5.

As can be seen from Fig. B.7b, the vertical spectrum of the metastable state is more complicated and presents a high number of transitions. It was divided in four regions but the vibrational study was carried out only for the first three regions. In Region I, the vibrational modes ν_1 and ν_2 in Fig. B.6 are activated, they can be attributed to the wagging and twisting of atoms 2 and 4, respectively. In addition to these, a second wagging ν_3 in Fig. B.6 is activated in the second region. In Region III, the modes ν_1 and ν_2 the asymmetric stretching (ν_5 in Fig. B.6) leads to a broad FC profile.

The FC distribution for the ground and valence excited state are reported in Table B.11 and B.12, respectively.

Molecular ion	Frequency (cm ⁻¹)		Normal mode				
	Reduced mass (a.m.u.)	ν_1	ν_2	ν_3	ν_4	ν_5	ν_6
¹ SiH ₃ ⁺	ω	906.	1000.7	1000.7	2377.	2441.	2441
	μ	1.1124	1.05526	1.05526	1.0078	1.05983	1.05983
³ SiH ₃ ⁺	ω	642.	677	829	1361	2335	3575
	μ	1.0151	1.0931	1.0419	1.0109	1.04353	1.00836

Table B.6: Normal modes ${}^x\text{SiH}_3^+$ ($x = 1, 3$)

In Fig. B.5 and B.6 are reported the vibrational normal modes for the ground and metastable state, respectively.

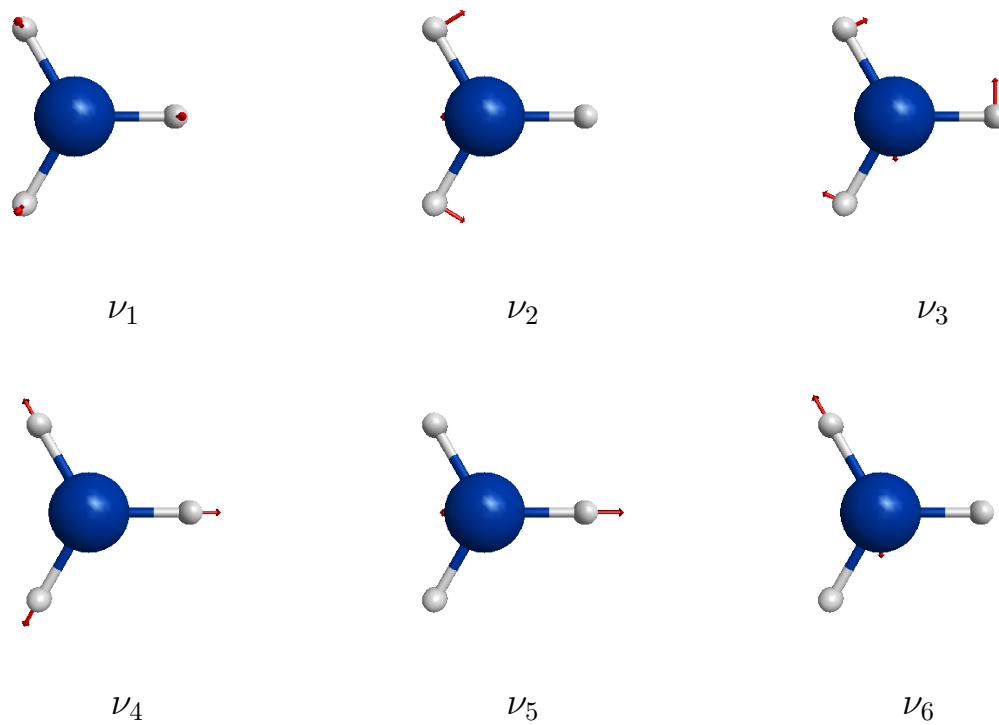


Figure B.5: ${}^1\text{SiH}_3^+$ normal modes.

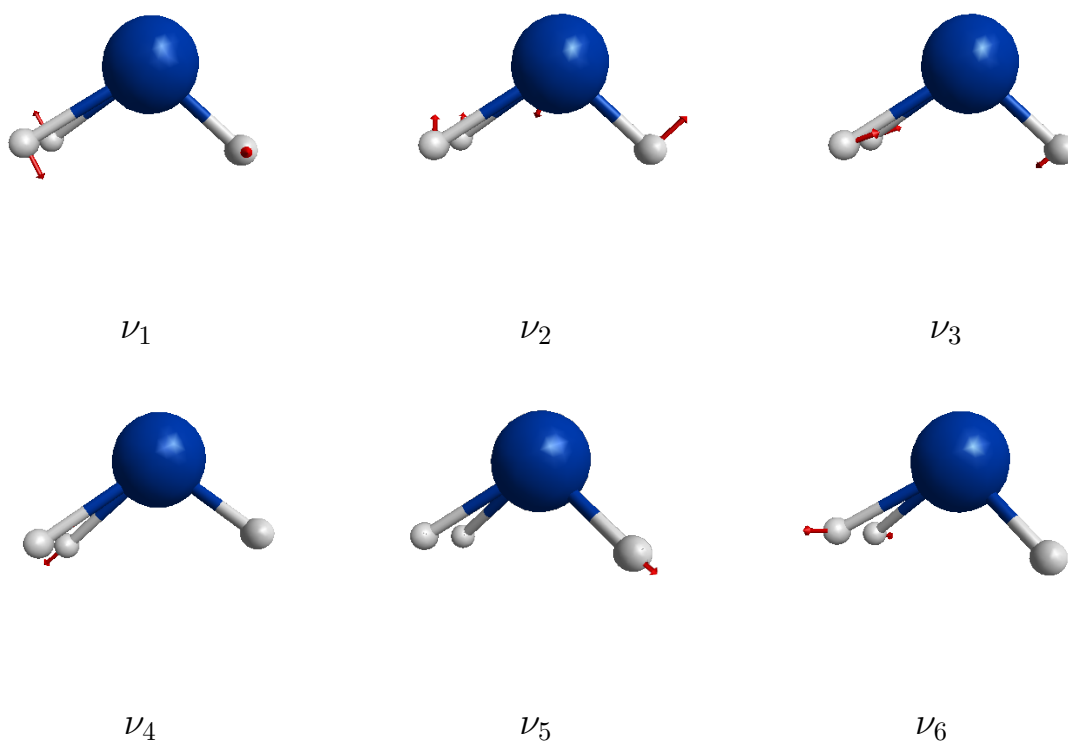
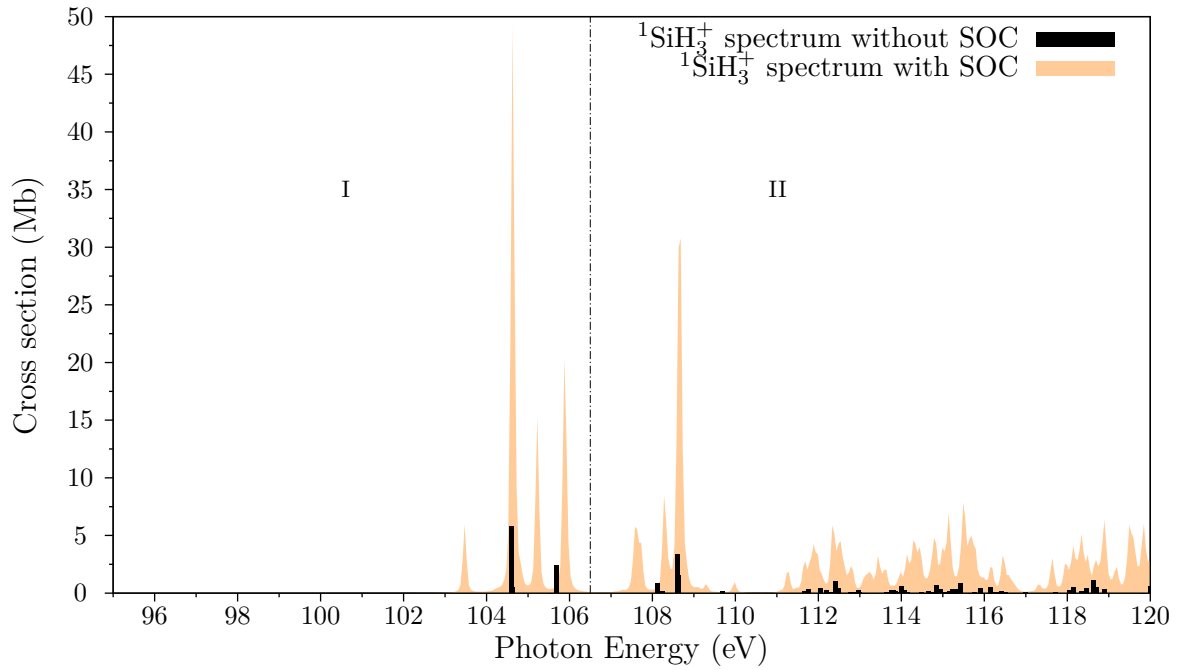
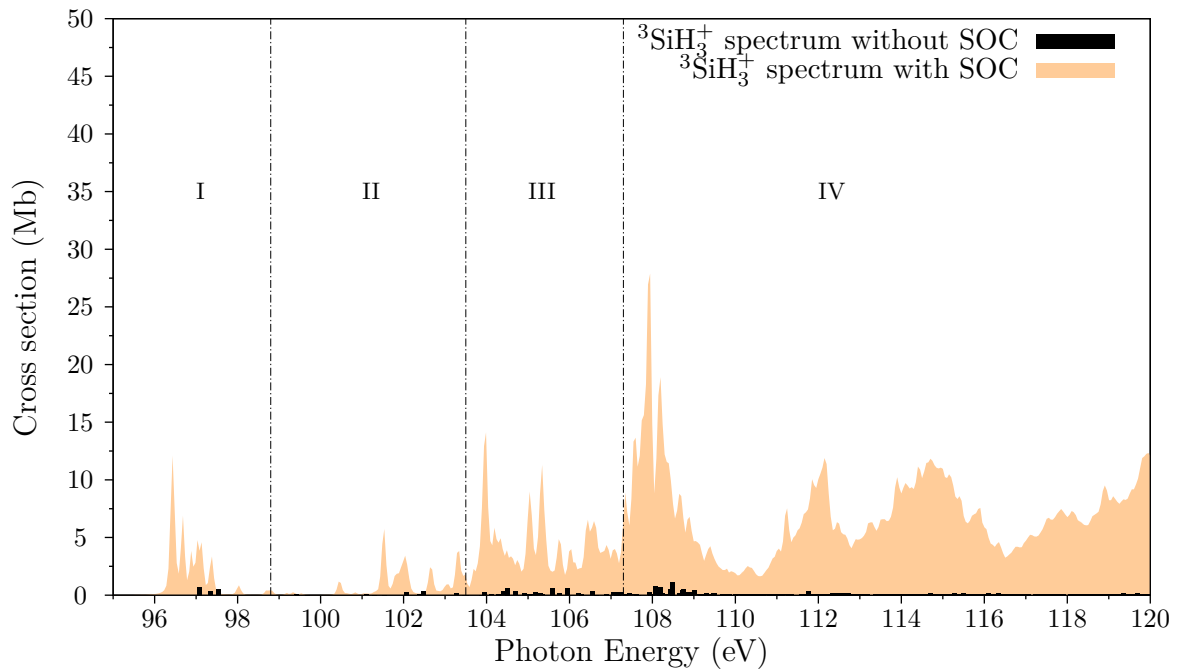


Figure B.6: ${}^3\text{SiH}_3^+$ normal modes



(a)



(b)

Figure B.7: Vertical X-ray photoabsorption spectra of ${}^1\text{SiH}_3^+$ (top) and ${}^3\text{SiH}_3^+$ (bottom)

Region	Gradient	FWHM	S	0-0	0-1	0-2	0-3	0-4	0-5	0-6	0-7	0-8	0-9	FC
Region I	0.052	0.530	0.6604	5.17E-01	3.41E-01	1.13E-01	2.48E-02	4.10E-03	5.41E-04	5.95E-05	5.62E-06	4.64E-07	3.40E-08	1.00000
Region II	0.117	1.200	3.3263	3.59E-02	1.20E-01	1.99E-01	2.20E-01	1.83E-01	1.22E-01	6.76E-02	3.21E-02	1.34E-02	4.93E-03	0.99768

Table B.7: SiH⁺ ground state

Region	Gradient	FWHM	S	0-0	0-1	0-2	0-3	0-4	0-5	0-6	0-7	0-8	0-9	FC
Region I	0.050	0.51	0.6598	0.516943	3.4E-01	1.1E-01	2.5E-02	4.1E-03	5.4E-04	5.9E-05	5.6E-06	4.6E-07	3.4E-08	1.00000
Region II	0.028	0.29	0.2036	0.815749	1.7E-01	1.7E-02	1.1E-03	5.8E-05	2.4E-06	8.1E-08	2.4E-09	6.0E-11	1.4E-12	1.00000
Region III	0.188	2.03	9.5177	0.000074	7.0E-04	3.3E-03	1.1E-02	2.5E-02	4.8E-02	7.6E-02	1.0E-01	1.2E-01	1.3E-01	0.51953

Table B.8: SiH⁺ metastable state

Region	XX	Gradient	FWHM	S	0-0	0-1	0-2	0-3	0-4	0-5	0-6	0-7	0-8	0-9	FC
Region I	$\nu 1$	0.05	0.78	7.51E+00	5.48E-04	4.11E-03	1.54E-02	3.87E-02	7.26E-02	1.09E-01	1.36E-01	1.46E-01	1.37E-01	1.15E-01	0.24038
	$\nu 2$	0.047	0.48	5.01E-01	6.06E-01	3.04E-01	7.61E-02	1.27E-02	1.60E-03	1.60E-04	1.34E-05	9.58E-07	6.01E-08	3.35E-09	1.00000
	$\nu 3$	2.76E-06	0.00	1.53E-09	1.00E+00	1.53E-09	1.18E-18	6.01E-28	2.31E-37	7.07E-47	1.81E-56	3.96E-66	7.59E-76	1.29E-85	1.00000
Region II	$\nu 1$	0.0035	0.05	3.68E-02	9.64E-01	3.55E-02	6.53E-04	8.00E-06	7.36E-08	5.42E-10	3.32E-12	1.75E-14	8.04E-17	3.29E-19	1.00000
	$\nu 2$	0.108	1.10	2.65E+00	7.08E-02	1.87E-01	2.48E-01	2.19E-01	1.45E-01	7.68E-02	3.39E-02	1.28E-02	4.24E-03	1.25E-03	0.99957
	$\nu 3$	1.80E-06	0.00	6.52E-10	1.00E+00	6.52E-10	2.13E-19	4.63E-29	7.54E-39	9.84E-49	1.07E-58	9.97E-69	8.13E-79	5.89E-89	1.00000
Region III	$\nu 1$	0.05	0.78	7.51E+00	5.48E-04	4.11E-03	1.54E-02	3.87E-02	7.26E-02	1.09E-01	1.36E-01	1.46E-01	1.37E-01	1.15E-01	0.77530
	$\nu 2$	0.057	0.59	7.38E-01	4.78E-01	3.53E-01	1.30E-01	3.20E-02	5.90E-03	8.70E-04	1.07E-04	1.13E-05	1.04E-06	8.51E-08	1.00000
	$\nu 3$	2.40E-06	0.00	1.16E-09	1.00E+00	1.16E-09	6.72E-19	2.60E-28	7.54E-38	1.75E-47	3.38E-57	5.60E-67	8.11E-77	1.05E-86	1.00000

Table B.9: SiH_2^+ ground state

Region	XX	Gradient	FWHM	S	0-0	0-1	0-2	0-3	0-4	0-5	0-6	0-7	0-8	0-9	FC
Region I	$\nu 1$	0.012	0.22	1.16E+00	3.15E-01	3.64E-01	2.10E-01	8.09E-02	2.34E-02	5.40E-03	1.04E-03	1.72E-04	2.48E-05	3.18E-06	1.00000
	$\nu 2$	0.034	0.61	7.92E+00	3.62E-04	2.87E-03	1.14E-02	3.00E-02	5.94E-02	9.42E-02	1.24E-01	1.41E-01	1.40E-01	1.23E-01	0.72590
	$\nu 3$	0.0745	0.86	3.00E+00	4.97E-02	1.49E-01	2.24E-01	2.24E-01	1.68E-01	1.01E-01	5.05E-02	2.17E-02	8.14E-03	2.71E-03	0.99889
Region II	$\nu 1$	0.044	0.82	1.55E+01	1.80E-07	2.79E-06	2.17E-05	1.12E-04	4.36E-04	1.35E-03	3.50E-03	7.78E-03	1.51E-02	2.61E-02	0.05435
	$\nu 2$	0.013	0.23	1.16E+00	3.14E-01	3.64E-01	2.11E-01	8.14E-02	2.36E-02	5.46E-03	1.05E-03	1.75E-04	2.53E-05	3.25E-06	1.00000
	$\nu 3$	0.029	0.33	4.55E-01	6.34E-01	2.89E-01	6.57E-02	9.96E-03	1.13E-03	1.03E-04	7.82E-06	5.08E-07	2.89E-08	1.46E-09	1.00000
Region III	$\nu 1$	0.066	1.22	3.49E+01	6.65E-16	2.32E-14	4.06E-13	4.73E-12	4.13E-11	2.89E-10	1.68E-09	8.40E-09	3.67E-08	1.42E-07	0.00000
	$\nu 2$	0.037	0.68	9.39E+00	8.40E-05	7.88E-04	3.70E-03	1.16E-02	2.71E-02	5.09E-02	7.97E-02	1.07E-01	1.25E-01	1.31E-01	0.53681
	$\nu 3$	0.082	0.95	3.64E+00	2.63E-02	9.57E-02	1.74E-01	2.11E-01	1.92E-01	1.40E-01	8.47E-02	4.40E-02	2.00E-02	8.09E-03	0.99568

Table B.10: SiH_2^+ metastable state

Region	XX	Gradient	FWHM	S	0-0	0-1	0-2	0-3	0-4	0-5	0-6	0-7	0-8	0-9	FC	
Region I	$\nu 1$	-3.00E-09	4.97E-08	3.13E-14	1.00E+00	3.1E-14	4.9E-28	5.1E-42	4.0E-56	2.5E-70	1.3E-84	5.9E-99	2.3E-113	8.0E-128	1.00000	
	$\nu 2$	2.90E-03	0.04	2.29E-02	9.77E-01	2.2E-02	2.6E-04	2.0E-06	1.1E-08	5.1E-11	2.0E-13	6.4E-16	1.8E-18	4.7E-21	1.00000	
	$\nu 3$	2.56E-05	0.00	1.78E-06	1.00E+00	1.8E-06	1.6E-12	9.5E-19	4.2E-25	1.5E-31	4.5E-38	1.1E-44	2.5E-51	5.1E-58	1.00000	
	$\nu 4$	9.00E-02	0.93	1.72E+00	1.79E-01	3.1E-01	2.6E-01	1.5E-01	6.6E-02	2.3E-02	6.5E-03	1.6E-03	1.6E-03	3.4E-04	6.6E-05	0.99998
	$\nu 5$	3.00E-03	0.03	1.68E-03	9.98E-01	1.7E-03	1.4E-06	7.9E-10	3.3E-13	1.1E-16	3.1E-20	7.5E-24	1.6E-27	1.6E-27	2.9E-31	1.00000
	$\nu 6$	2.09E-05	0.00	8.16E-08	1.00E+00	8.2E-08	3.3E-15	9.1E-23	1.8E-30	3.0E-38	4.1E-46	4.8E-54	4.9E-62	4.9E-62	4.4E-70	1.00000
Region II	$\nu 1$	3.00E-09	0.00	3.13E-14	1.00E+00	3.1E-14	4.9E-28	5.1E-42	4.0E-56	2.5E-70	1.3E-84	5.9E-99	2.3E-113	8.0E-128	1.00000	
	$\nu 2$	5.00E-03	0.01	6.81E-02	9.34E-01	6.4E-02	2.2E-03	4.9E-05	8.4E-07	1.1E-08	1.3E-10	1.3E-12	1.1E-14	8.1E-17	1.00000	
	$\nu 3$	4.70E-05	0.00	6.01E-06	1.00E+00	6.0E-06	1.8E-11	3.6E-17	5.5E-23	6.6E-29	6.6E-35	5.7E-41	4.2E-47	2.8E-53	1.00000	
	$\nu 4$	2.37E-02	0.24	1.19E-01	8.87E-01	1.1E-01	6.3E-03	2.5E-04	7.5E-06	1.8E-07	3.6E-09	6.1E-11	9.1E-13	1.2E-14	1.00000	
	$\nu 5$	7.00E-03	0.07	9.15E-03	9.91E-01	9.1E-03	4.1E-05	1.3E-07	2.9E-10	5.3E-13	8.1E-16	1.1E-18	1.2E-21	1.2E-21	1.00000	
	$\nu 6$	5.00E-05	0.00	4.67E-07	1.00E+00	4.7E-07	1.1E-13	1.7E-20	2.0E-27	1.8E-34	1.4E-41	9.6E-49	5.6E-56	5.6E-56	2.9E-63	1.00000

Table B.11: SiH_3^+ ground state

Region	XX	Gradient	FWHM	S	0-0	0-1	0-2	0-3	0-4	0-5	0-6	0-7	0-8	0-9	FC
Region I	ν_1	0.026	0.48	7.2E+00	7.13E-04	5.2E-03	1.9E-02	4.5E-02	8.2E-02	1.2E-01	1.4E-01	1.5E-01	1.3E-01	1.1E-01	0.80473
	ν_2	0.038	0.67	1.23E+01	4.75E-06	5.8E-05	3.6E-04	1.5E-03	4.5E-03	1.1E-02	2.2E-02	3.9E-02	6.0E-02	8.2E-02	0.22066
	ν_3	7.70E-05	0.42	2.88E-05	1.00E+00	2.9E-05	4.1E-10	4.0E-15	2.8E-20	1.6E-25	7.9E-31	3.2E-36	1.2E-41	3.7E-47	1.00000
	ν_4	0.0002	0.34	4.52E-05	1.00E+00	4.5E-05	1.0E-09	1.5E-14	1.7E-19	1.6E-24	1.2E-29	7.6E-35	4.3E-40	2.2E-45	1.00000
	ν_5	0.0032	0.01	2.22E-03	9.98E-01	2.2E-03	2.5E-06	1.8E-09	1.0E-12	4.5E-16	1.7E-19	5.2E-23	1.5E-26	3.6E-30	1.00000
	ν_6	0.043	0.11	1.16E-01	8.91E-01	1.0E-01	5.9E-03	2.3E-04	6.6E-06	1.5E-07	2.9E-09	4.9E-11	7.0E-13	9.0E-15	1.00000
Region II	ν_1	0.031	0.60	1.03E+01	3.36E-05	3.5E-04	1.8E-03	6.1E-03	1.6E-02	3.2E-02	5.6E-02	8.2E-02	1.1E-01	1.2E-01	0.42094
	ν_2	0.1	1.88	8.49E+01	1.37E-37	1.2E-35	4.9E-34	1.4E-32	3.0E-31	5.0E-30	7.1E-29	8.6E-28	9.1E-27	8.6E-26	0.00000
	ν_3	0.2	2.40	1.94E+02	5.54E-85	1.1E-82	1.0E-80	6.7E-79	3.3E-77	1.3E-75	4.1E-74	1.1E-72	2.8E-71	5.9E-70	0.00000
	ν_4	0.0037	0.05	1.55E-02	9.85E-01	1.5E-02	1.2E-04	6.1E-07	2.3E-09	7.3E-12	1.9E-14	4.1E-17	8.0E-20	1.4E-22	1.00000
	ν_5	0.018	0.18	7.02E-02	9.32E-01	6.5E-02	2.3E-03	5.4E-05	9.4E-07	1.3E-08	1.6E-10	1.6E-12	1.4E-14	1.1E-16	1.00000
	ν_6	0.14	1.16	1.22E+00	2.94E-01	3.6E-01	2.2E-01	9.0E-02	2.8E-02	6.7E-03	1.4E-03	2.4E-04	3.7E-05	5.0E-06	1.00000
Region III	ν_1	0.016	0.31	2.7E+00	6.43E-02	1.8E-01	2.4E-01	2.2E-01	1.5E-01	8.3E-02	3.8E-02	1.5E-02	5.1E-03	1.6E-03	0.99943
	ν_2	0.024	0.44	4.9E+00	7.53E-03	3.7E-02	9.0E-02	1.5E-01	1.8E-01	1.8E-01	1.4E-01	1.0E-01	6.1E-02	3.3E-02	0.97201
	ν_3	0.016	0.27	1.2E+00	2.89E-01	3.6E-01	2.2E-01	9.2E-02	2.9E-02	7.1E-03	1.5E-03	2.6E-04	4.0E-05	5.6E-06	1.00000
	ν_4	0.015	0.20	2.5E-01	7.76E-01	2.0E-01	2.5E-02	2.1E-03	1.3E-04	6.9E-06	2.9E-07	1.1E-08	3.4E-10	9.5E-12	1.00000
	ν_5	0.15	1.55	4.9E+00	7.63E-03	3.7E-02	9.1E-02	1.5E-01	1.8E-01	1.8E-01	1.4E-01	9.9E-02	6.0E-02	3.3E-02	0.97245
	ν_6	0.011	0.09	7.56E-03	9.92E-01	7.5E-03	2.8E-05	7.2E-08	1.4E-10	2.0E-13	2.6E-16	2.6E-19	2.8E-22	2.2E-25	1.00000

Table B.12: SiH_3^+ metastable state

Bibliography

- [1] A. N. Witt. “The chemical composition of interstellar medium”. In: *Philosophical transactions of the Royal Society A* 359 (2001), pp. 1949–1959.
- [2] E. Herbst. “The chemistry of interstellar space”. In: *Chemical Society Review* 30 (3 2001), pp. 168–176.
- [3] K. M. T. Yamada and G. Winnewisser. *Interstellar Molecules - Their laboratory and interstellar habitat*. Springer-Verlag Berlin Heidelberg, 2011.
- [4] D. W. Savin et al. “The impact of recent advances in laboratory astrophysics on our understanding of the cosmos”. In: *Reports on Progress in Physics* 75.3 (2012), p. 036901.
- [5] T. Dunham. “Interstellar Neutral Potassium and Neutral Calcium”. In: *Publications of the Astronomical Society of the Pacific* 49.287 (), p. 26.
- [6] P. Swings and L. Rosenfeld. In: *Astrophysical Journal* 86 (1937), p. 483.
- [7] A.E. Douglas and G. Herzberg. In: *Astrophysical Journal* 94 (1941), p. 483.
- [8] F. Wyrowski et al. “First interstellar detection of OH⁺”. In: *Astronomy & Astrophysics* 518 (2010), A26.
- [9] M. Gerin et al. “Interstellar OH⁺, H₂O⁺ and H₃O⁺ along the sight-line to G10.6-0.4”. In: *Astronomy & Astrophysics* 518 (2010), p. L110.
- [10] V. Ossenkopf et al. “Detection of interstellar oxidaniumyl: Abundant H₂O⁺ towards the star-forming regions DR21, Sgr B2, and NGC6334”. In: *Astronomy & Astrophysics* 518 (2010), p. L111.
- [11] K. M. Menten et al. “Submillimeter absorption from SH⁺, a new widespread interstellar radical, ¹³CH⁺ and HCl*”. In: *Astronomy & Astrophysical* 525 (2011), A77.
- [12] A. O. Benz, A. O. et al. “Hydrides in young stellar objects: Radiation tracers in a protostar-disk-outflow system”. In: *Astronomy & Astrphysical* 521 (2010), p. L35.

- [13] M. De Luca et al. “Herschel/HIFI Discovery of HCl^+ in the Interstellar Medium”. In: *The Astrophysical Journal Letters* 751.2 (2012), p. L37.
- [14] N. Grevesse and A. J. Sauval. “Identification of SiH^+ in the solar photospheric spectrum”. In: *Astronomy and astrophysics* 9 (1970), p. 1970.
- [15] A.A. de Almeida and P. D. Singh. “Predictions on finding the SiH^+ and SiH in interstellar space”. In: *Astrophysics and Space Science* 56.2 (1978), pp. 415–419.
- [16] R. K. Janev and D. Reiter. “Collision processes of CH_y and CH_y^+ hydrocarbons with plasma electrons and protons”. In: *Physics of Plasmas* 9.9 (2002), pp. 4071–4081.
- [17] S. Mehrabian et al. “Ion impact distribution over plasma exposed nanocone arrays”. In: *Physics of Plasmas* 20.3 (2013), p. 033501.
- [18] M. Meyyappan et al. “Carbon nanotube growth by PECVD: a review”. In: *Plasma Sources Science and Technology* 12.2 (2003), p. 205.
- [19] L. Mangolini and U. Kortshagen. “Nonthermal Plasma Synthesis of Silicon Nanocrystals”. In: *Silicon Nanocrystals*. Wiley-VCH Verlag GmbH & Co. KGaA, 2010, pp. 309–348.
- [20] L. Sainiemi et al. “Non-Reflecting Silicon and Polymer Surfaces by Plasma Etching and Replication”. In: *Advanced Materials* 23.1 (2011), pp. 122–126.
- [21] S. E. Babayan et al. “Deposition of silicon dioxide films with a non-equilibrium atmospheric-pressure plasma jet”. In: *Plasma Sources Science and Technology* 10.4 (2001), p. 573.
- [22] I. Martìn et al. “Surface passivation of p-type crystalline Si by plasma enhanced chemical vapor deposited amorphous SiC_xH films”. In: *Applied Physics Letters* 79.14 (2001), pp. 2199–2201.
- [23] T. Roschek et al. “Comprehensive study of microcrystalline silicon solar cells deposited at high rate using 13.56 MHz plasma-enhanced chemical vapor deposition”. In: *Journal of Vacuum Science & Technology A: Vacuum, Surfaces, and Films* 20.2 (2002), pp. 492–498.
- [24] U. Fantz. “Spectroscopic diagnostics and modelling of silane microwave plasmas”. In: *Plasma Physics and Controlled Fusion* 40.6 (1998), p. 1035.
- [25] M. S. Gordon. “Structure and stability of SiH_4^+ ”. In: *Chemical Physics Letters* 59.3 (1978), pp. 410–413.

- [26] H. Sun and K. F. Freed. “Ab-initio effective valence shell Hamiltonian calculation of valence state potential curves of CH and CH⁺”. In: *Chemical Physics Letters* 78.3 (1981), pp. 531–537.
- [27] T. Graber et al. “CH₂⁺ is bent”. In: *The Journal of Chemical Physics* 98.10 (1993), pp. 7725–7729.
- [28] S. P. Mort et al. “Photodissociation pathways and conical intersections in the lowlying electronic states of SiH₂⁺”. In: *The Journal of Chemical Physics* 101 (1994), p. 10576.
- [29] P. C. Stancil et al. “The photodissociation of SiH⁺ in interstellar clouds and stellar atmospheres”. In: *The Astrophysical Journal* 486 (1997), pp. 574–579.
- [30] J.M. Bizau et al. “A merged-beam setup at SOLEIL dedicated to photoelectron-photoion coincidence studies on ionic species”. In: *Journal of Electron Spectroscopy and Related Phenomena* 210 (2016), pp. 5–12.
- [31] *SOLEIL synchrotron facility - Pléiades beam line*. URL: <https://www.synchrotron-soleil.fr/fr/lignes-de-lumiere/pleiades>.
- [32] J.-P. Mosnier et al. “Inner-shell photoexcitations as probes of the molecular ions CH⁺, OH⁺, and SiH⁺: Measurements and theory”. In: *Physical Review A* 93 (6 2016), p. 061401.
- [33] W. L. Borst and E. C. Zipf. “Lifetimes of Metastable CO and N₂ Molecules”. In: *Physical Review A* 3 (3 1971), pp. 979–989.
- [34] A. V. Phelps and J. P. Molnar. “Lifetimes of Metastable States of Noble Gases”. In: *Physical Review* 89 (6 1953), pp. 1202–1208.
- [35] P. Bolognesi et al. “Pyrimidine and halogenated pyrimidine near edge x-ray absorption fine structure spectra at C and N K-edges: experiment and theory”. In: *The Journal of Chemical Physics* 133 (2010), p. 034302.
- [36] V. Feyer et al. “Core level study of alanine and threonine”. In: *The Journal of Chemical Physics* 112 (2008), pp. 7806–7815.
- [37] H. Ade and A.P. Hitchcock. “NEXAFS microscopy and resonant scattering: Composition and orientation probed in real and reciprocal space”. In: *Polymer* 49.3 (2008), pp. 643–675.
- [38] M.D. Crapper et al. “Determination of the adsorption structure for formate on Cu(110) using SEXAFS and NEXAFS”. In: *Surface Science* 171.1 (1986), pp. 1–12.

- [39] E. Breynaert, C. Bruggeman, and A. Maes. “XANES-EXAFS Analysis of Se Solid-Phase Reaction Products Formed upon Contacting Se(IV) with FeS₂ and FeS”. In: *Environmental Science & Technology* 42.10 (2008), pp. 3595–3601.
- [40] A. Thompson et al. *X-Ray Data Booklet*. 2009.
- [41] D. D. Vvedensky. “Theory of X-ray absorption fine structure”. In: *Unoccupied Electronic States: Fundamentals for XANES, EELS, IPS and BIS*. Ed. by John C. Fuggle and John E. Inglesfield. Berlin, Heidelberg: Springer Berlin Heidelberg, 1992, pp. 139–176. ISBN: 978-3-540-47473-9.
- [42] B. H. Bransden and C. J. Joachain. *Physics of Atoms and Molecules*. 2nd edition. Pearson Education, 1983.
- [43] J. Stöhr. *NEXAFS Spectroscopy*. Ed. by G. Ertl, R. Gomer, and D. L. Mills. Springer Series in Surface Sciences 25. ”Springer Berlin Heidelberg”, 1992.
- [44] G. B. Armen et al. “The resonant Auger effect”. In: *Journal of Physics B: Atomic, Molecular and Optical Physics* 33.2 (2000).
- [45] M. O. Krause. “Atomic radiative and radiationless yields for K and L shells”. In: *Journal of Physical and Chemical Reference Data* 8.2 (1979).
- [46] W. Eberharft et al. “Recent advances in studies of the electronic decay of core excited states in small molecules”. In: *Physica Scripta* T41 (1992), pp. 143–148.
- [47] E. Condon. “A Theory of Intensity Distribution in Band Systems”. In: *Phys. Rev.* 28 (6 1926), pp. 1182–1201.
- [48] J. Franck and E. G. Dymond. “Elementary processes of photochemical reactions”. In: *Trans. Faraday Soc.* 21 (February 1926), pp. 536–542.
- [49] Edward U. Condon. “Nuclear Motions Associated with Electron Transitions in Diatomic Molecules”. In: *Phys. Rev.* 32 (6 1928), pp. 858–872.
- [50] T. E. Sharp and H. M. Resenstock. “Franck-Condon factors for polyatomic molecules”. In: *The Journal of Chemical Physics* 41 (1964), p. 3453.
- [51] E. V. Doktorov, A. Malkin, and V. I. Manko. “Dynamical symmetry of vibronic transitions in polyatomic molecules and the Franck-Condon principle”. In: *Journal of Molecular Spectroscopy* 56 (1975), pp. 1–20.
- [52] D. J. Tannor. *Introduction to quantum mechanics: a time-dependent perspective*. Ed. by Univ Science Books. 2007.

- [53] T. Helgaker, P. Jørgensen, and J. Olsen. *Molecular electronic structure theory*. 2000.
- [54] A. Szabo and N. S. Ostlund. *Modern quantum chemistry - Introduction to advanced electronic structure theory*. Dover Publications, Inc., New York - First Edition Revised, 1996.
- [55] C. C. J. Roothaan. "Self-Consistent Field Theory for Open Shells of Electronic Systems". In: *Review of Modern Physics* (2 1960).
- [56] J. A. Pople and R. K. Nesbet. "Self - Consistent Orbitals for Radicals". In: *The Journal of Chemical Physics* 22.3 (1954), pp. 571–572.
- [57] M. F. Guest and V. R. Saunders. "On methods for converging open-shell Hartree-Fock wavefunctions". In: *Molecular Physics* 28.3 (1973), pp. 819–828.
- [58] Takashi Tsuchimochi and Gustavo E. Scuseria. "Communication: ROHF theory made simple". In: *The Journal of Chemical Physics* 133.14 (2010), p. 141102.
- [59] R.J. Harrison; N.C. Handy. "Full CI calculations on BH, H₂O, NH₃, and HF". In: *Chemical Physics Letters* 95 (4-5 1983).
- [60] H. Lischka et al. "New implementation of the graphical unitary group approach for multireference direct configuration interaction calculations". In: *International Journal of Quantum Chemistry* 20.S15 (1981), pp. 91–100.
- [61] R. P. Hosteny et al. "Ab initio study of the π -electron states of trans-butadiene". In: *The Journal of Chemical Physics* 62.12 (1975), pp. 4764–4779.
- [62] J. Paldus et al. *The Unitary Group for the Evaluation of Electronic Energy Matrix Elements*. Lecture Notes in Chemistry 22. Springer, 1981.
- [63] J. B. Foresman et al. "Toward a systematic molecular orbital theory for excited states". In: *The Journal of Physical Chemistry* 96.1 (1992), pp. 135–149.
- [64] R. C. Ladner and W. A. Goddard III. "Improved Quantum Theory of Many-Electron Systems. V. The Spin-Coupling Optimized GI Method". In: *The Journal of Chemical Physics* 51.3 (1969), pp. 1073–1087.
- [65] W. A. Goddard et al. "Generalized valence bond description of bonding in low-lying states of molecules". In: *Accounts of Chemical Research* 6.11 (1973), pp. 368–376.
- [66] J.M. Langlois et al. "Rule-Based Trial Wave Functions for Generalized Valence Bond Theory". In: *The Journal of Physical Chemistry* 98 (1994), pp. 13498–13505.
- [67] P. Hohenberg and W. Kohn. "Inhomogeneous Electron Gas". In: *Phys. Rev.* 136 (3B 1964), B864–B871.

- [68] A.P. Hitchcock and C.E. Brion. “K-shell excitation spectra of CO, N₂ and O₂”. In: *Journal of Electron Spectroscopy and Related Phenomena* 18.1 (1980), pp. 1–21. ISSN: 0368-2048.
- [69] A.P. Hitchcock and I. Ishii. “Carbon K-shell excitation spectra of linear and branched alkanes”. In: *Journal of Electron Spectroscopy and Related Phenomena* 42.1 (1987), pp. 11–26.
- [70] Y. Ma et al. “High-resolution K-shell photoabsorption measurements of simple molecules”. In: *Physical Review A* 44 (3 1991), pp. 1848–1858.
- [71] J. Stöhr et al. “Identification of C—H resonances in the K-shell excitation spectra of gas-phase, chemisorbed, and polymeric hydrocarbons”. In: *Physical Review B* 36 (5 1987), pp. 2976–2979.
- [72] J. Åhlunda et al. “The electronic structure of iron phthalocyanine probed by photoelectron and x-ray absorption spectroscopies and density functional theory calculations”. In: *The Journal of Chemical Physics* 125 (2006), p. 034709.
- [73] Y. Tamenori et al. “Hydrogen bonding in methanol clusters probed by inner-shell photoabsorption spectroscopy in the carbon and oxygen K-edge regions”. In: *The Journal of Chemical Physics* 128 (2008), p. 124321.
- [74] S. Coriani et al. “Coupled-cluster response theory for near-edge x-ray-absorption fine structure of atoms and molecules”. In: *Physical Review* 1 85 (2012), p. 022507.
- [75] T. Fransson et al. “Carbon X-ray absorption spectra of fluoroethenes and acetone: A study at the coupled cluster, density functional, and static-exchange levels of theory”. In: *The Journal of Chemical Physics* 138 (2013), p. 124311.
- [76] K. Ueda et al. “Symmetry-Resolved Vibrational Spectra of Carbon K-Shell Photoelectron Satellites in Carbon Monoxides: Experiment and Theory”. In: *Physical Review Letters* 94 (2005), p. 243004.
- [77] E. Kawerk et al. “Resonant inelastic x-ray scattering on iso-C₂H₂Cl₂ around the chlorine K-edge: Structural and dynamical aspects”. In: *The Journal of Chemical Physics* 141.14 (2014), p. 144301.
- [78] A. A. El-Azhary and H. U. Suter. “Comparison between Optimized Geometries and Vibrational Frequencies Calculated by the DFT Methods”. In: *The Journal of Physical Chemistry* 100.37 (1996), pp. 15056–15063.

- [79] J. A. Montgomery Jr. et al. "A complete basis set model chemistry. VI. Use of density functional geometries and frequencies". In: *The Journal of Chemical Physics* 110.6 (1999), pp. 2822–2827.
- [80] Rahul V. Pinjari et al. "Restricted active space calculations of L-edge X-ray absorption spectra: From molecular orbitals to multiplet states". In: *The Journal of Chemical Physics* 141.12 (2014), p. 124116.
- [81] Michael Roemelt et al. "A combined DFT and restricted open-shell configuration interaction method including spin-orbit coupling: Application to transition metal L-edge X-ray absorption spectroscopy". In: *The Journal of Chemical Physics* 138.20 (2013), p. 204101.
- [82] R. F. Fink, M. Kivilompolo, and H. Aksela. "Theory and ab initio calculations of 2p photoabsorption spectra: The lowest Rydberg resonances in HCl". In: *The Journal of Chemical Physics* 111.22 (1999), pp. 10034–10045.
- [83] M. Kivilompolo et al. "The Cl(2p) photoelectron spectra of the HCl and DCl molecules: the effects of the molecular field". In: *Journal of Physics B: Atomic, Molecular and Optical Physics* 33.5 (2000), p. L157.
- [84] D. G. Fedorov and M. S. Gordon. "A study of relative importance of one and two-electron contributions to spin-orbit coupling". In: *The Journal of Chemical Physics* 112 (13 2000), p. 5611.
- [85] M.W. Schmidt et al. "General Atomic and Molecular Electronic Structure System". In: *J. Comput. Chem.* 14 (1993), pp. 1347–1363.
- [86] Thom H. Dunning Jr. "Gaussian basis sets for use in correlated molecular calculations. I. The atoms boron through neon and hydrogen". In: *The Journal of Chemical Physics* 90.2 (1989), pp. 1007–1023.
- [87] A. D. Becke. "Density-functional thermochemistry. III. The role of exact exchange". In: *Journal of Chemical Physics* (98 1993), pp. 5648–5652.
- [88] C. Lee, W. Yang, and R. G. Parr. "Development of the Colic-Salvetti correlation-energy formula into a functional of the electron density". In: *Physical Review B* (37 1988), pp. 785–789.
- [89] P. J. Stephens et al. "Ab Initio Calculation of Vibrational Absorption and Circular Dichroism Spectra Using Density Functional Force Fields". In: *The Journal of Physical Chemistry* 98.45 (1994), pp. 11623–11627.

- [90] J. Ivanic. “Direct configuration interaction and multiconfigurational self-consistent-field method for multiple spaces with variable occupations. I. Method”. In: *The Journal of Chemical Physics* 119 (18 2003), p. 9364.
- [91] J. D. Bozek et al. “Vibrationally resolved core-level photoelectron spectroscopy: Si $2p$ levels of SiH₄ and SiF₄ molecules”. In: *Physical Review Letters* 65 (22 1990), pp. 2757–2760.
- [92] C. Nicolas and C. Miron. “Lifetime broadening of core-excited and -ionized states”. In: *Journal of Electron Spectroscopy and Related Phenomena* 185 (2012), pp. 267–272.
- [93] S. Green et al. “Calculated Potential-Energy Curves for CH⁺”. In: *Physical Review A* 5 (4 1972), pp. 1614–1618.
- [94] Karl K. Irikura. “Experimental Vibrational Zero-Point Energies: Diatomic Molecules”. In: *Journal of Physical and Chemical Reference Data* 36.2 (2007), pp. 389–397.
- [95] P.J. Linstrom and W.G. Mallard. *NIST Chemistry WebBook*. Version NIST Standard Reference Database Number 69. National Institute of Standards and Technology, Gaithersburg MD, 20899. URL: <http://cccbdb.nist.gov/>.
- [96] H. Ågren et al. “Direct SCF direct static-exchange calculations of electronic spectra”. In: *Theoretical Chemistry Accounts* 97.1 (1997), pp. 14–40.
- [97] Franck Jensen. *Introduction to computational chemistry*. Ed. by Chichester John Wiley & Sons. 1999.
- [98] S. Katsumata and D.R. Lloyd. “The photoelectron spectra of the OH and OD radicals”. In: *Chemical Physics Letters* 45.3 (1977), pp. 519–522.
- [99] L. V. Gurvich, I. V. Veyts, and C. B. Alcock. *Thermodynamic Properties of Individual Substances, Fourth Edition*. Hemisphere Pub. Co., New York, 1989.
- [100] T.J. Sear et al. “Diode Laser absorption spectroscopy of D₃O⁺: Determination of the equilibrium structure and potential function of the oxonium ion”. In: *The Journal of Chemical Physics* 83.6 (1985), p. 2676.
- [101] E. Hirota and H. Ishikawa. “The vibrational spectrum and molecular constants of silicon dihydride SiH₂ in the ground electronic state”. In: *The Journal of Chemical Physics* 110.9 (1999), pp. 4254–4257.
- [102] Chikashi Yamada and Eizi Hirota. “Detection of the Silyl Radical SiH₃ by Infrared Diode-Laser Spectroscopy”. In: *Physical Review Letters* 56 (9 1986), pp. 923–925.

-
- [103] K. P. Huber and G. Herzberg. *Molecular spectra and molecular structure*. Vol. IV. Constant of diatomic molecules. Van Nostrand Reinhold Co., 1979.
- [104] H. Aksela et al. “Partial Auger decay rates of core-ionized molecular states in HCl and DCI”. In: *Journal of Physics B: Atomic, Molecular and Optical Physics* 28.19 (1995), p. 4259.
- [105] T. Miteva, S. Kazandjian, and N. Sisourat. “On the computations of decay widths of Fano resonances”. In: *Chemical Physics* 482 (2017), pp. 208–215.
- [106] M. R. et al. “SHARC: ab initio Molecular Dynamics with Surface Hopping in the Adiabatic Representation Including Arbitrary Couplings”. In: *Journal of Chemical Theory and Computation* 7.5 (2011), pp. 1253–1258.
- [107] S. Mai, P. Marquetand, and L. González. “A General Method to Describe Intersystem Crossing Dynamics in Trajectory Surface Hopping”. In: *International Journal of Quantum Chemistry* 115 (2015), pp. 1215–1231.